Craneless Buoyancy-Assisted Monopile Upending

Functional Concept Design of a Friction-Based Gripper

ME54035: Msc Thesis

M.T. van der Slot

Delft University of Technology

TU Delft

TWD

Craneless Buoyancy-Assisted Monopile Upending

Functional Concept Design of a Friction-Based Gripper

by

M.T. van der Slot

In partial fulfillment of the requirements for the degree of

Master of Science
in Mechanical Engineering

at Delft University of Technology

Student number: 5166683
MSc Track: Multi-Machine Engineering
Report Number: 2026.MME.9197

Project duration: December, 2025 – June, 2026
Supervisors: J. Jovanova, TU Delft
J. Termorshuizen TWD

TU Delft TWD

Preface

This thesis was conducted as part of the Master's programme in Mechanical Engineering at TU Delft and focuses on the development of a craneless installation method for offshore monopiles.

Large-scale mechanical design is the subtopic of my master's programme that interests me the most, and developing a giant machine to handle monopiles is a textbook example that satisfies this interest. Combined with the challenges that offshore installation brings, this thesis has been a challenging but exciting assignment.

With the completion of my thesis, there are several people I would like to thank. First of all, I would like to thank my TU Delft supervisor, Jovana Jovanova, for providing guidance and valuable feedback throughout the process. Your support in allowing me to push myself has made this thesis period incredibly insightful, with a steep learning curve.

In addition, I would like to express my gratitude to my graduation company TWD. A special thanks goes to Jelmar Termorshuizen, my supervisor at TWD, who always made time to help me get started and provided relevant insights from an operational perspective. Spending 40 hours a week at the company, I also really appreciated the support from the Innovation Team. Their motivation to make the most of my time, combined with the enjoyable moments during lunch breaks, made this thesis project surprisingly bearable.

On a personal note, I would like to thank my family and friends for their continuous support in pursuing my academic interests. A special appreciation goes to Rens Heemskerk, who always provided support and critical insight throughout both this thesis and my entire studies.

Finishing this thesis marks the end of my studies and the start of my professional career. I am excited to begin working in the offshore field and to see where this next chapter will lead.

M.T. van der Slot
Rotterdam, June 2026

Abstract

The increasing size of offshore wind monopiles has intensified reliance on heavy lift vessels (HLVs), leading to cost and availability constraints. To mitigate this reliance, this research investigates the technical feasibility of a craneless buoyancy-assisted upending method. The proposed concept allows a highly available Jack-Up Vessel (JUV) to upend floating monopiles using controlled seawater ballasting and a custom friction-based gripper.

The method combines controlled ballasting and vertical displacement to rotate the monopile from a horizontal to a vertical position without the use of a crane. The concept was validated through a coupled systems engineering framework. Global time-domain dynamic simulations evaluated the kinematic trajectory and wave-induced environmental disturbances. Subsequently, local analytical sizing models, supported by empirical laboratory friction data, verified the structural integrity of the monopile during engagement of the proposed gripper.

The global analysis demonstrated that active ballasting and a 10 m vertical jacking stroke successfully reduce the perceived weight of a 2,170-tonne reference monopile to an effective load of just 950 tonnes, yielding a baseline longitudinal shear force of 9,500 kN. The optimal trajectory guarantees a 3 m seabed clearance safety buffer.

To safely transfer the 9,500 kN shear load without inducing localized shell yielding, empirical data established a required normal clamping force of 40,000 kN. The proposed "Radial Hydraulic Gripper" concept distributes this massive load across sixteen 2 m by 1 m polymer pads. This 8×2 architecture restricts local steel bending stresses to a safe 180 MPa (well below the 355 MPa yield limit) while preventing polymer crushing. To translate these requirements into a physical machine, a full, functional concept design was developed. This includes the mechanical layout of the gripper system and a detailed, step-by-step operational sequence for the gripper-monopile engagement and the actual upending maneuver. Logistically, shifting from an HLV to a JUV yields an estimated operational expenditure (OPEX) saving of €21.8 million per wind farm. Ultimately, this thesis proves that friction-based, craneless upending is mathematically defensible, structurally safe, and economically advantageous.

Contents

List of Figures

List of Tables

Nomenclature

Abbreviations

Abbreviation	Definition
3XL	Triple Extra Large (Monopile size class)
BAI	Buoyancy Assisted Installation
BL	Boundary Lubrication
CAPEX	Capital Expenditure
CoB	Center of Buoyancy
CoG	Center of Gravity
COF	Coefficient of Friction
DNV	Det Norske Veritas
DoF	Degrees of Freedom
DP	Dynamic Positioning
FBD	Free Body Diagram
FEM	Finite Element Method
FSE	Free Surface Effect
HL	Hydrodynamic Lubrication
HLV	Heavy Lift Vessel
JONSWAP	Joint North Sea Wave Project
JUV	Jack-Up Vessel
LCoE	Levelized Cost of Energy
MCA	Multi-Criteria Analysis
ML	Mixed Lubrication
MP	Monopile
MW	Megawatt
ODE	Ordinary Differential Equation
OPEX	Operational Expenditure
RES	Renewable Energy Source
SF	Safety Factor
SQ	Subquestion
SWL	Still Water Level
T&I	Transport and Installation
WTG	Wind Turbine Generator
XXL	Extra Extra Large (Monopile size class)

Symbols

Latin Symbols

Symbol	Definition	Unit
a	Empirical friction exponential pressure scale parameter	[-]
A	General cross-sectional area	[m^2]
A_i	Internal cross-sectional area of the monopile	[m^2]
A_{mp}	Cross-sectional area of the structural steel wall	[m^2]
A_o	Outer gross cross-sectional area of the monopile	[m^2]
A_{req}	Idealized total physical pad contact area required	[m^2]
$A_{sub,i}$	Submerged cross-sectional area of structural strip i	[m^2]
b	Empirical friction exponential baseline intercept / Unit height	[-] / [m]
B_{total}	Total integrated hydrostatic buoyancy force	[N]
c	Empirical friction asymptotic offset parameter	[-]
C_a	Dimensionless 3D hydrodynamic added mass coefficient	[-]
C_{DS}	3D-corrected member hydrodynamic drag coefficient	[-]
C_M	Hydrodynamic inertia coefficient $(1 + C_a)$	[-]
d	Total water depth measured from still water level	[m]
$dF_{b,i}$	Elemental buoyant force acting on structural strip i	[N]
D_b	Bottom outer diameter of the monopile	[m]
D_o	Reference outer diameter for hydrodynamics	[m]
D_t	Top outer diameter of the monopile	[m]
dz	Infinitesimal longitudinal thickness of a strip element	[m]
E	Modulus of Elasticity (Young's Modulus) for steel	[MPa]
F	General force vector	[N]
F_{cyl}	Required continuous radial push force per hydraulic cylinder	[kN]
F_f	Maximum achievable friction force	[N]
F_{fric_req}	Total required vertical frictional holding capacity	[kN]
F_{pad}	Radial clamping force exerted by a single individual pad	[kN]
$F_{req\_per\_pad}$	Share of the global holding demand per individual pad	[kN]
F_{tang}	Applied tangential shear load on the interface	[N]
f_{Eh}	Characteristic elastic shell buckling strength	[MPa]
g	Gravitational acceleration	[m/s^2]
h_i	Local submerged depth of structural strip i	[m]
H_s	Significant wave height	[m]
I	General mass moment of inertia	[kg·m^2]
I_P	Total system mass moment of inertia about the pivot	[kg·m^2]
$\dot{I}_P$	Time rate of change of total system inertia about pivot	[kg·m^2/s]
$I_{a,P}$	Hydrodynamic added mass inertia about the pivot	[kg·m^2]
$I_{bal,P}$	Mass moment of inertia of internal ballast about pivot	[kg·m^2]
$I_{mp,P}$	Mass moment of inertia of dry steel pile about pivot	[kg·m^2]
k	Wave number $(2\pi/\lambda)$	[rad/m]
k_2	Roark hoop stress deformation ring constant $(1 - \alpha_h)$	[-]
K	Instantaneous rotational system stiffness	[Nm/rad]
KC	Keulegan-Carpenter number	[-]
l	Longitudinal length of evaluated unstiffened cylinder	[m]
L	Total structural length of the monopile	[m]
L_a	Length of the cylindrical section after the cone	[m]
L_b	Length of the cylindrical section before the cone	[m]
L_c	Longitudinal length of the tapered conical section	[m]
l_{eo}	DNV-defined equivalent length of cooperating shell plating	[m]
L_{eff_total}	Total effective shell length resisting radial crushing	[m]
L_{pad}	Physical longitudinal length of a gripper pad	[m]
m_{bal}	Total mass of the internal water ballast	[T]
m_{mp}	Total dry structural mass of the steel monopile	[T]

Symbol	Definition	Unit
M_B	Hydrostatic buoyancy moment about the pivot	[Nm]
M_{bal}	Gravitational driving moment of the internal ballast	[Nm]
M_{max}	Peak localized circumferential ring bending moment	[Nm]
M_{mp}	Gravitational driving moment of the dry steel structure	[Nm]
M_{drag}	Hydrodynamic relative velocity drag moment	[Nm]
$M_{wave,I}$	Hydrodynamic wave inertia moment	[Nm]
N	Normal clamping force applied perpendicular to a surface	[N]
n	Minimum required pad count per circumferential ring	[-]
n_{cyl}	Total number of independent radial hydraulic actuators	[-]
N_{rings}	Total number of vertically stacked gripper pad rings	[-]
p_{eq}	Smeared equivalent uniform external radial pressure	[MPa]
Q	Volumetric ballast water pump flow rate	[m^3/h]
r	Perpendicular distance from rotation axis to mass element	[m]
R	Outer radius of the cylindrical monopile structure	[m]
R_i	Inner radius of the hollow cylinder wall	[m]
R_o	Outer radius of the hollow cylinder wall	[m]
R_x	Transverse local reaction force at the gripper pivot	[N]
R_z	Axial local structural shear force at the gripper pivot	[N]
$R_{Z,G}$	Global vertical reaction force acting on the gripper frame	[N]
R_a	Arithmetic mean surface roughness of structural steel	[μm]
SF_μ	Material/uncertainty safety factor for friction coefficient	[-]
t	Time stepping variable	[s]
t_{mp}	Average wall thickness of the steel monopile shell	[mm]
T	Ambient atmospheric operational temperature	[°C]
T_n	Shifting natural period of the physical system	[s]
T_p	Peak wave period of the design sea state	[s]
u	Undisturbed horizontal water particle velocity	[m/s]
$\dot{u}$	Undisturbed horizontal water particle acceleration	[m/s^2]
u_{max}	Maximum horizontal water particle surface velocity	[m/s]
u_n	Normal water particle velocity projected onto pile axis	[m/s]
$\dot{u}_n$	Normal water particle acceleration projected onto pile axis	[m/s^2]
U_R	Dimensionless Ursell number	[-]
v_c	Steady depth-averaged current velocity	[m/s]
v_j	Continuous vertical jacking translation velocity	[m/min]
v_{mp}	Local normal structural velocity of a pile segment	[m/s]
v_{rel}	Relative normal fluid-structure velocity step	[m/s]
w	Undisturbed vertical water particle velocity	[m/s]
$\dot{w}$	Undisturbed vertical water particle acceleration	[m/s^2]
W	Radial line load mapped onto a unit 2D ring slice	[kN/m]
W_{pad}	Physical circumferential width of a gripper pad	[m]
W_{slice}	Elastic section modulus of a unit horizontal ring slice	[m^3]
x	Body-fixed local transverse coordinate axis	[m]
X_G	Earth-fixed global horizontal coordinate axis	[m]
$x_{C,i}$	Local transverse shift of internal fluid segment centroid	[m]
X_{G,C_i}	Global horizontal coordinate of strip ballast centroid	[m]
z	Body-fixed local longitudinal coordinate axis	[m]
z_B	Local longitudinal coordinate of buoyancy center	[m]
z_C	Local longitudinal coordinate of ballast center of gravity	[m]
z_{fill}	Internal ballast water vertical fill height	[m]
$z_{fill,0}$	Initial internal ballast water vertical fill level	[m]
Z_G	Earth-fixed global vertical coordinate axis	[m]
$Z_{G,i}$	Global vertical position of discrete strip center i	[m]
$Z_{G,P,0}$	Initial global height of the physical pivot point	[m]
z_i	Local longitudinal coordinate of discrete strip center i	[m]

Symbol	Definition	Unit
z_{off}	Mechanical pivot offset from dry Center of Gravity	[m]
z_p	Local longitudinal coordinate of the gripper pivot	[m]
z_{surf}	Longitudinal coordinate of internal fluid free surface	[m]
z_{swl}	Longitudinal coordinate of outer waterline intersection	[m]
$\dot{z}_{swl}$	Longitudinal velocity of outer waterline intersection	[m/s]
$Z_{G,P}$	Continuous global vertical pivot height coordinate	[m]
$Z_{G,P,max}$	Upper bounding limit of global vertical pivot height	[m]
$Z_{G,P,min}$	Lower bounding limit of global vertical pivot height	[m]
$z_{off,max}$	Upper bounding limit of physical pivot offset location	[m]
$z_{off,min}$	Lower bounding limit of physical pivot offset location	[m]
$Z_{G,tip}$	Instantaneous global vertical position of the lower tip	[m]

Greek Symbols

Symbol	Definition	Unit
α	Structural cone geometric inclination angle	[°]
α_h	Dimensionless hoop-stress ring deformation factor	[-]
α_i	Submerged cross-sectional central angle of strip i	[rad]
$\Delta\theta$	Angular perturbation step for finite difference derivative	[rad]
ΔM_{net}	Infinitesimal variation in net static restoring moment	[Nm]
θ	Rotational pitch angle / upending equilibrium angle	[°] or [rad]
θ_0	Initial starting pitch trim orientation angle	[°]
$\dot{\theta}$	Angular pitch velocity of the rotating structure	[rad/s]
$\ddot{\theta}$	Angular pitch acceleration of the rotating structure	[rad/s^2]
λ	Calculated airy wave length of the sea state	[m]
μ	Coefficient of friction	[-]
$\mu(\sigma)$	Pressure-dependent operational friction coefficient function	[-]
μ_k	Kinetic sliding coefficient of friction	[-]
μ_{nom}	Idealized constant nominal coefficient of friction	[-]
μ_s	Static sticking coefficient of friction	[-]
ρ_s	Mass density of structural steel S355	[kg/m^3]
ρ_w	Mass density of North Sea salt water	[kg/m^3]
σ	Actual normal contact pressure applied to a pad face	[MPa]
σ_b	Peak localized elastic circumferential bending stress	[MPa]
$\sigma_{h,Sd}$	Design circumferential membrane (hoop) stress value	[MPa]
σ_{nom}	Target nominal polymer design contact pressure	[MPa]
ω	Angular wave frequency ($2\pi/T_p$)	[rad/s]
ω_n	Angular natural eigenfrequency of the floating assembly	[rad/s]

1

Introduction

As the offshore wind industry rapidly scales to meet global energy demands, the installation of next-generation XXL monopiles has emerged as a critical logistical bottleneck. While a limited number of high-capacity offshore vessels are technically capable of handling these increasingly massive structures, their availability remains limited. As monopile size and mass continue to grow, the required lifting capacity is approaching the upper limits of the existing installation fleet. To contextualize this challenge, this chapter formulates the core problem statement, introduces a novel craneless upending concept, and outlines the design methodology that forms the engineering framework of this thesis.

1.1. Background

Global climate targets are driving a rapid expansion in renewable energy, where offshore wind is seen as the main renewable energy source (RES) [1]. This results in a rapid expansion of offshore wind farms. The economic viability of these projects relies on the structural foundations that support the wind turbine generators (WTGs) in harsh marine environments.

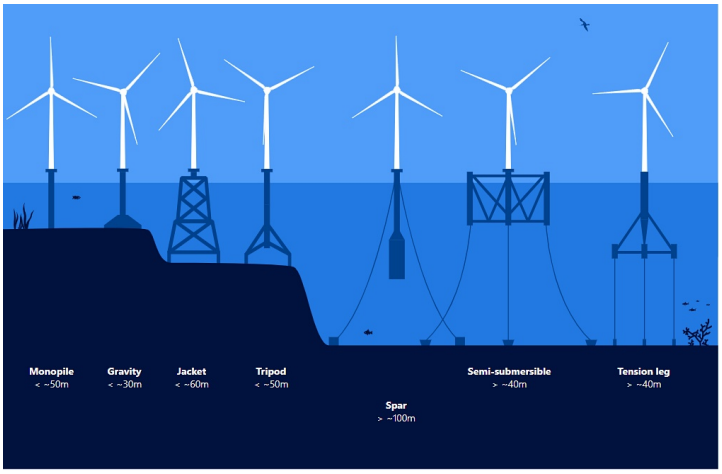

Figure 1.1: Typical foundations of wind turbines [2].

Various foundation types exist, ranging from gravity-based structures to floating platforms, as illustrated in Figure 1.1. From these foundations, the monopile (Figure 1.2) is the most used foundation, as indicated by Figure 1.3. Driven by their simplicity, adaptability to various soil conditions, and cost-effectiveness, monopiles currently account for approximately 80 % of all offshore wind turbine foundations worldwide [3] [1].

Figure 1.2: An image of a monopile made at SIF.

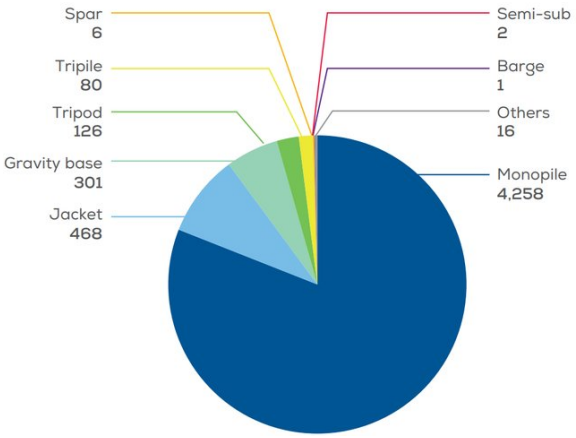

Figure 1.3: Share of foundations that are monopiles [4].

The drive to reduce the Levelized Cost of Energy (LCoE) [5] has led to an exponential increase in turbine size. Modern offshore turbines are already in the 15 MW class [3]. To support these massive wind turbines, while also moving into slightly deeper water, the monopile foundations must scale accordingly in both diameter and length.

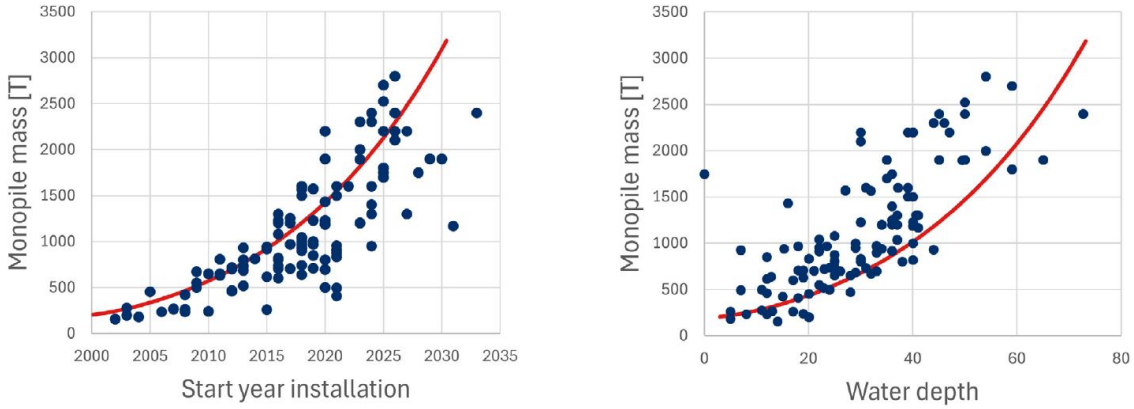

Figure 1.4: Evolution of monopile mass (in tonnes) relative to the start year of installation (left) and water depth (right). The red curves indicate the general growth trend in both metrics [6].

This scaling results in a rapid increase of the structural mass of the monopiles. As shown in Figure 1.4, the historical trend of monopile mass demonstrates a substantial upward trajectory. While monopiles installed in the early 2000s weighed less than 500 tonnes, current installations concern monopiles weighing between 1,500 and 2,500 tonnes. Furthermore, the projected trend indicates [6] that the industry is rapidly moving towards XXL and 3XL monopiles, with masses expected to exceed 3,000 to 4,000 tonnes.

The massive dimensions and weights of these next-generation monopiles have pushed traditional handling and installation methodologies to their limits, creating a severe bottleneck for the industry's future.

1.2. Installation Vessel Bottlenecks

The drive to continually lower the Levelized Cost of Energy (LCoE) is forcing the industry to critically re-evaluate transport and installation (T&I) logistics. Currently, the manufacturing of the support structure and its associated installation operations account for approximately 25% [7] of the total capital expenditure (CAPEX) of an offshore wind farm.

Traditionally, monopiles are transported to the offshore site horizontally and upended into a vertical position using the main crane of a Heavy Lift Vessel (HLV) or a specialized, purpose-built Jack-Up Vessel (JUV). This conventional upending sequence requires the crane to lift the entire structural weight of the monopile.

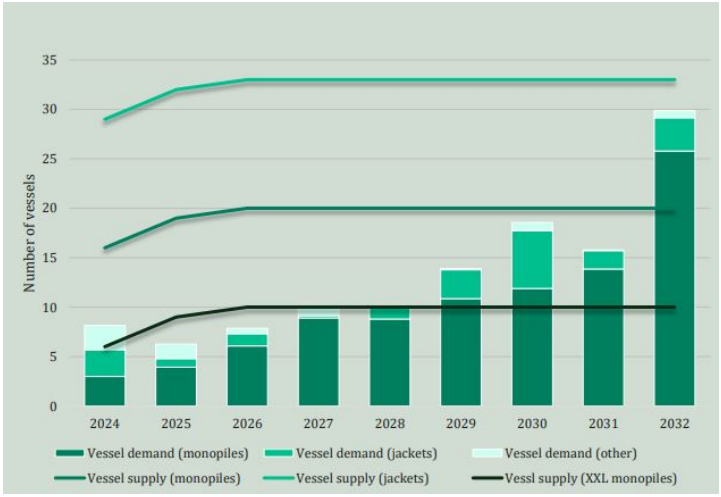

Figure 1.5: Foundation installation vessel supply and demand projections [8].

As monopiles approach the 3,000 to 4,000-tonne threshold, this traditional lifting method is reaching its physical limits. Only a fraction of the global offshore installation fleet is equipped with the crane capacity and hook height required to handle these massive structures. As illustrated in Figure 1.5, the offshore wind industry is rapidly approaching a critical vessel shortage, where the demand for top-tier installation vessels (Figure 1.5 black line) will outpace supply (Figure 1.5 dark green bars) [8]. This supply chain bottleneck threatens to inflate vessel day rates exponentially.

Currently, traditional upending methods force developers to rely on the most expensive tier of the installation fleet. According to recent 2025 market estimates by TNO [9], Heavy Lift Vessels capable of handling next-generation monopiles ask day rates of €400,000 or more.

To maintain the economic viability of future offshore wind projects and circumvent this lurking vessel shortage, the industry must develop novel installation methodologies. This thesis presents a buoyancy-assisted craneless upending solution where a floating monopile is presented to a friction-based gripper mounted on a standard, highly available Jack-Up Vessel (JUV). By shifting the operation away from a €400,000/day HLV to a standard €250,000/day JUV [9], this concept provides a massive reduction in daily operational expenditure (OPEX) while actively bypassing the heavy-lift supply chain bottleneck.

1.3. The Proposed Concept

To address the scaling limitations of traditional heavy-lift operations, this research proposes a novel craneless upending concept. The method integrates a vertically translating frame with the passive lifting power of ballast-assisted rotation. To handle the massive loads of an XXL monopile without inflicting structural damage, the concept uses a friction-based gripper.

The general sequence of the proposed concept is illustrated in the storyboard below (Figure 1.6):

- **Phase 1: Approach and Connection.** The temporarily sealed, buoyant monopile is towed to the Jack-Up Vessel (JUV). The vertical frame lowers to the waterline, and the friction-based gripper firmly clamps the floating pile.
- **Phase 2: Initiation.** Seawater is pumped into the base of the monopile. Simultaneously, the JUV's vertical frame begins to lift the gripper upwards. The shifting internal weight and the upward motion at the pivot actively initiate rotation.
- **Phase 3: Controlled Rotation.** As ballast intake and vertical lifting continue, the monopile passively rotates towards a vertical orientation. The upward vertical translation guarantees the descending base clears the seabed. Throughout this rotation, the friction gripper securely holds the pile, transferring all structural and environmental loads without allowing the pile to slip.
- **Phase 4: Vertical Handover and Embedment.** Once the pile reaches a stable, fully vertical orientation ($90°$), ballasting is halted and the bottom plug is removed. The vertical frame then reverses direction, lowering the gripped monopile directly into the seabed. Once self-stable embedment is achieved, the gripper releases, and standard piling operations start.

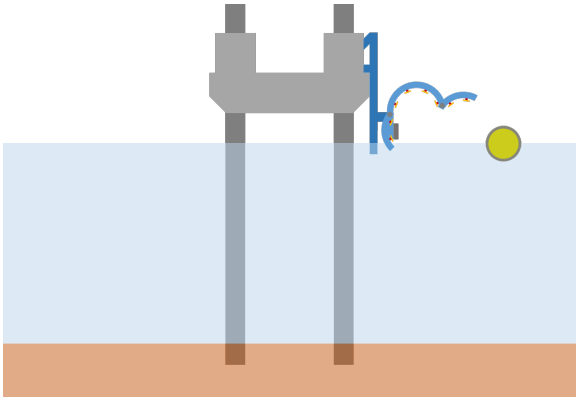

(a) Phase 1: Buoyant monopile is transported and presented to the gripper with tugboats.

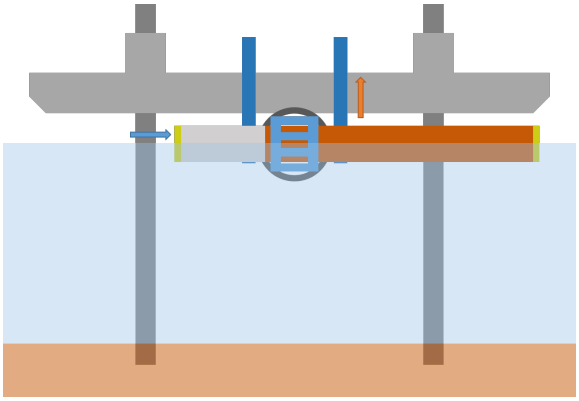

(b) Phase 2: The gripper engages the monopile, and ballasting is initiated.

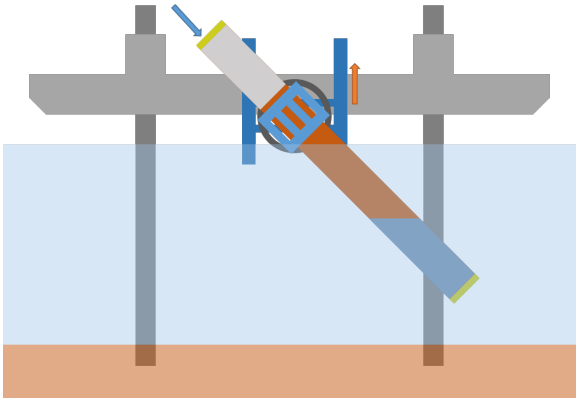

(c) Phase 3: Controlled rotation. Gripper assembly elevates while ballast fills.

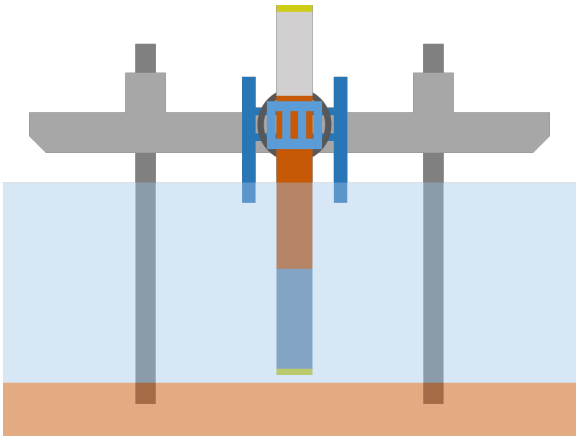

(d) Phase 4: gripper assembly is at 90°after which the monopile is moved downwards to self stable embedment depth.

Figure 1.6: Schematic overview of the proposed craneless upending sequence.

1.4. Design Objective and Methodology

The main objective of this thesis is:

> *To develop and verify a functional concept design for a friction-based, craneless upending system that can safely upend a monopile without compromising its structural integrity*

To achieve this main design objective, this thesis adopts a systems engineering approach. The upending process is divided into a global dynamic problem and a local structural problem. By developing analytical models for both, the resulting safe operational boundaries can be used to synthesize and evaluate a mechanical concept design. This design framework is illustrated in Figure 1.7

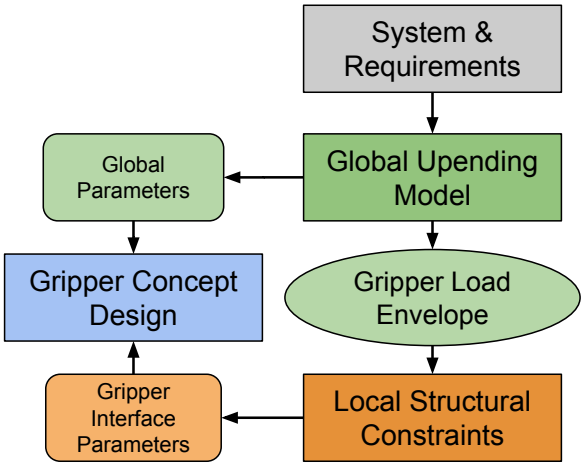

Figure 1.7: Design framework.

- **SQ1: System & Requirements.** What operational, environmental, and structural requirements govern the gripping and upending of a monopile alongside a JUV?
- **SQ2: Global Upending Model (Upending Dynamics)**. How can the monopile's rotation and movement during upending be modeled?
- **SQ3: Local Structural Model (Local Interface Mechanics).** How can the interaction between clamp force, friction, and local shell buckling of the monopile be modeled to determine safe clamping conditions?
- **SQ4: Gripper Concept Design.** How can the models be used to design and evaluate a feasible gripper concept?

1.5. Thesis Outline

To answer the research questions, this thesis is structured into seven chapters. The progression flows from theoretical background and physical boundary conditions to dynamic modeling, structural interface verification, and final concept synthesis.

- **Chapter 2: State of the Art** reviews the mechanical limitations of traditional heavy-lift operations and evaluates current alternative buoyancy-based upending concepts. It systematically assesses offshore gripping technologies, identifying friction as the most viable mechanism, and establishes the fundamental tribological physics that govern wet polymer-steel interfaces.
- **Chapter 3: System Definition** answers **SQ1**. It defines the physical properties of the target 2,170-tonne XXL monopile and establishes the environmental design parameters and wave kinematics in accordance with DNV standards as well as the requirement and assumptions made.
- **Chapter 4: Global Upending Dynamics** answers **SQ2** by developing a quasi-static model to identify the optimal values for the global parameters. After which a time-domain analytical model of the upending sequence is developed. It evaluates the hydrostatic, hydrodynamic, and ballasting forces during the vertical translation of the pivot point, ultimately defining the monopile's kinematic trajectory and the peak global reaction loads exerted on the gripper.
- **Chapter 5: Local Interface Mechanics** answers **SQ3** by translating the massive global shear loads from Chapter 4 into localized structural demands. Utilizing laboratory data for wet friction, this chapter filters the clamping requirements through local steel yielding limits and global elastic buckling limits to establish a safe operational window and provide a baseline for the gripper pad geometry, resulting in the local variables.
- **Chapter 6: Functional Concept Design** answers **SQ4** by the global and local variables into a tangible 3D functional concept design. The resulting design is evaluated against the operational performance criteria and boundary conditions. A full operation sequence of the concept is explained as well as the economic viability of the proposed concept.
- **Chapter 7: Conclusion and Recommendations** summarizes the key analytical findings of the research, evaluates the overarching feasibility of the craneless upending concept, and provides recommendations for future detailed engineering phases and numerical verifications.

2

State of the Art

This chapter establishes the technical foundation for the craneless, ballast-assisted upending methodology by reviewing three key engineering domains. First, current commercial monopile installation practices are evaluated to define the operational baseline. Second, historical and conceptual developments in buoyancy-assisted installation (BAI) are reviewed to illustrate the progress already made within the research field. Finally, since the proposed concept relies on gripping the monopile, friction is demonstrated to be the most suitable gripping principle for this application, after which the resulting design implications of adopting friction-based gripping are discussed.

2.1. Traditional Monopile Installation

Monopiles are typically transported from the fabrication yard to a quay close to the installation site with a heavy cargo vessel (Figure 2.1). From the nearby quay the monopiles are transported to the installation site in a horizontal orientation, sea-fastened on a feeder barge (Figure 2.2) or on the deck of the installation vessel (Figure 2.5).

Figure 2.1: Heavy cargo vessel [10].

Figure 2.2: Feeder barge towed by a tugboat [11].

At the installation site, in the most commonly used configuration, a single main crane lifts the monopile near its top end, while the lower end is supported on deck by an upending tool such as an upend hinge, as illustrated in Figure 2.3. As the crane hoists, the monopile rotates about the lower support tool, moving the monopile from a horizontal to a vertical orientation. Guiding the monopile with an upend hinge prevents uncontrolled motion of the MP during upending, but requires substantial crane hook height.

After upending, the monopile is lifted over the vessel side and transferred into the water. A gripper (Figure 2.4) will enclose the monopile to support the last action of the installation sequence: penetrating the seabed. This is done with an impact hammer.

Figure 2.3: Monopile upending operation utilizing a deck-mounted upending hinge [12].

Figure 2.4: Monopile positioned within the gripper system alongside the installation vessel [13].

Monopile installations are currently mostly performed with purpose-built Jack-Up Vessels (Figure 2.5) or heavy lift vessels (Figure 2.6) [1]. Each of the two types offers certain advantages and limitations regarding stability, lifting capacity, and costs [14].

Jack-Up Vessels provide a fixed installation platform by extending legs to the seabed and elevating the hull above the water surface [15]. This eliminates vessel motions during lifting and pile handling. As a result, JUVs have been the most used vessel for monopile installation. However, their applicability is constrained by water depth, leg length, and most importantly, crane capacity [14].

Figure 2.5: Purpose built Jack-Up Vessel DEME Innovation [16].

Floating heavy lift vessels operate while floating and rely on dynamic positioning (DP) systems to remain in position [17]. This vessel class enables installation in deeper waters and can accommodate larger crane capacities. However, unlike Jack-Up Vessels, floating HLVs are influenced by wave- and wind-induced motions. During monopile lifting and upending, these motions are transferred to the pile resulting in strict operational limits and narrow weather windows.

The need for a larger crane capacity to install heavier monopile foundations drives a transition from JUVs to the need for HLVs [15]. This transition has significant implications for monopile handling, introducing more dynamics to consider. But more importantly, vessel selection and availability have become critical factors in the feasibility and cost of installing next generation monopile foundations.

Figure 2.6: Heavy lift vessel Seaway Strashnov [18].

2.2. Buoyancy Assisted Installation

Buoyancy Assisted Installation (BAI) uses the buoyancy force of a monopile to relieve the required weight that has to be lifted for monopile installation. This section explores the current state of buoyancy-assisted installation and relevant research on this topic.

2.2.1. Svanen Upending

An established method for buoyancy assisted monopile installation uses the heavy lift vessel Svanen [19]. In this upending procedure, the monopile is first made buoyant by installing caps at both ends, allowing natural buoyancy to support part of its weight. The buoyant monopile is then transported from the quay to the installation site by tugboat, as shown in Figure 6.10.

Figure 2.7: Floating monopile towed by a tugboat [20].

Once at the vessel, the monopile is maneuvered with the help of tugboats to the crane of the Svanen installation vessel, as shown in Figure 2.8. After this, the main crane connects slings to two lifting discs mounted on the monopile. These disc connections are used to initiate the upending operation. A secondary crane is attached to the bottom cap to enable its controlled release once the monopile reaches a vertical orientation. During the upending phase, buoyancy significantly reduces the required crane capacity (Figure 2.9). After the monopile has reached a stable vertical position, the bottom cap is removed [21]. After which, the MP is transferred to the gripper frame, which acts as a guide for the MP seabed penetration.

Figure 2.8: Floating monopile presented to Svanen by a tugboat [22].

Figure 2.9: The heavy lift vessel Svanen performing a monopile upending operation [23].

2.2.2. Craneless Upending via Vertical Translation

To completely eliminate the reliance on heavy-lift cranes during the upending phase, the industry has explored alternative kinematic mechanisms. An early method of this was successfully introduced by the Fugro Seacore barge 'Excalibur' [24]. In this operation, a relatively small foundation pile (approximately 4 meters in diameter) is presented to the vessel in a buoyant, floating state. It is securely engaged by a structural gripper positioned just below the conical section, as illustrated in Figure 2.10.

Figure 2.10: A barge from Fugro Seacore performing craneless monopile upending using a vertically translating frame and gripper [24].

The gripper is mounted to a specialized vertical frame attached to the side of the vessel. A hydraulic system drives the entire assembly upward along guide rails. As the gripper elevates, it lifts the upper section of the monopile out of the water. Acting as a translating pivot point, this upward motion naturally induces the rotation of the monopile from a horizontal buoyant state into a fully vertical orientation. Once vertical, the installation is completed using standard piling equipment.

2.2.3. Buoyancy Assisted Upending Concepts

As a possible solution to the physical limitations of heavy-lift cranes, academic and industry research has investigated buoyancy-assisted craneless installation methods. A concept, explored by Raaijman [25] and further developed by TWD as the 'Craneless Monopile Installation' method [6], proposes upending a floating monopile by solely relying on controlled ballasting and the application of an external mechanical moment.

In this proposed methodology, a fully capped, buoyant monopile is towed to the site and connected to a floating monopile guide. The upending sequence is initiated by passively pumping seawater into the base of the monopile. However, because the length of modern monopiles significantly exceeds typical wind farm water depths, simple continuous ballasting would cause the pile to draft too deeply, resulting in a seabed collision.

To circumvent this, the TWD sequence halts the ballasting process once a safe seabed clearance is reached, as illustrated in Figure 2.11. The pumps are then reversed (deballasting), and a massive external counteracting moment is simultaneously applied at the rotation point to force the monopile into a final vertical orientation. Once vertical, the monopile is locked, pressurized to safely remove the bottom cap, and lowered to the seafloor.

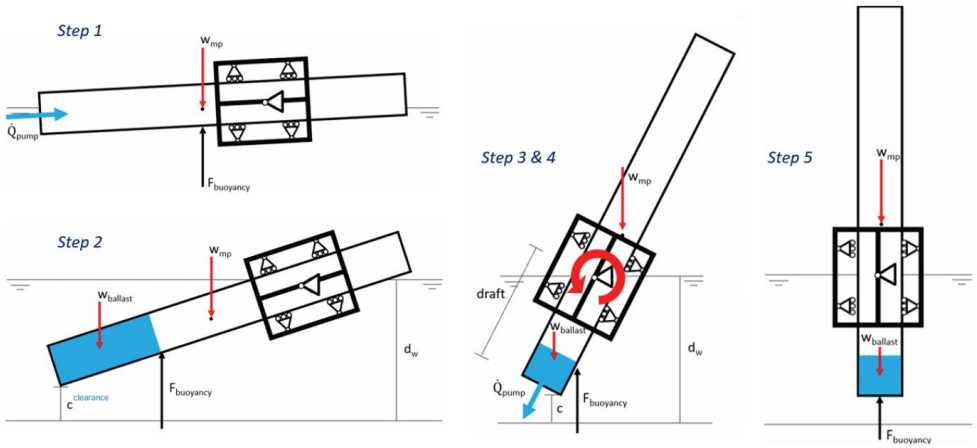

Figure 2.11: Steps in the craneless upending method as defined by Raaijman [25].

The scalability of this concept is substantial. A benchmark study by TWD applied this sequence to a future-generation XXL monopile (Ø15m, 4500 tonnes) in 60-meter water depth. The analysis concluded that the maneuver requires approximately 9,500 tonnes of ballast water and an external applied moment of 450 MNm to successfully upend the pile. If successful, this concept would allow developers to completely eliminate Heavy Lift Vessels (HLVs) from the installation campaign, utilizing highly economical dynamically positioned (DP) semi-submersible barges equipped with motion-compensated upending systems instead.

While this craneless methodology offers immense operational advantages, it introduces a severe mechanical challenge. Generating and transferring a 450 MNm control moment to a floating 4,500-tonne steel monopile, an effort equivalent to lifting 1,500 tonnes with a 30-meter lever arm, introduces a significant engineering challenge.

Therefore, there is a critical need to explore alternative kinematic strategies that do not require such extreme counteracting moments. To address this gap, this thesis investigates an alternative application of the ballast-assisted method. Rather than forcing the monopile to rotate around a vertically fixed pivot point, seabed collision can be prevented by actively translating the entire gripper and monopile assembly vertically during the rotation.

However, to successfully execute this vertical translation and maintain control over the monopile's trajectory, the upending tool must be fundamentally redesigned. It requires a gripping mechanism that acts as a rigid, no-slip interface, instead of a guide that allows for translation.

2.3. Offshore Gripping and Handling

To identify a gripping mechanism capable of performing the no-slip vertical translation required for the craneless upending concept, the physical constraints of the marine environment must first be established. Offshore handling introduces unique loading and environmental conditions that differs from onshore handling. A prior literature study [26] assessed gripping mechanisms across the range of offshore handling operations. The study identified three governing criteria for feasibility in this environment: robustness (structural integrity under dynamic shock loads), wet performance (holding capacity in lubricated conditions), and scalability (potential to handle multi-kiloton loads). The classification and evaluation resulted in the matrix presented in Table 2.1.

Table 2.1: Comparative evaluation matrix of gripping mechanisms for offshore splash zone operations.

Class Name	Mechanism Class	Robustness	Wet Performance	Scalability	Key Offshore Constraint
Impactive	**Frictional**	**+** *Prone to slip* [27]	**+** *Lubrication reduces grip* [28]	**++** *Scales with actuator* [29], [30]	Requires massive normal forces
	Form Closure	**++** *Geometric interlocking* [31]	**++** *Unaffected by fluids* [32]	**++** *Scales with structure* [33]	Requires specific payload geometry
	Soft / Variable Stiffness	**-** *Distributes stress well* [34]	**+** *Conformal slip risk* [34]	**- -** *Material stress overload* [35]	Hyperelastic material limits
Ingressive	**Penetrative**	**++** *Mechanical surface embedding* [36]	**++** *Bypasses surface films* [37]	**++** *Proven offshore capability* [36], [38]	Inflicts permanent payload damage
Astrictive	**Suction (Passive)**	**-** *Seal easily broken* [39]	**-** *Water weakens seal* [39]	**- -** *Low pressure differential* [40]	Inadequate heavy lifting capacity
	Vacuum (Active)	**-** *Vulnerable to leaks* [41]	**-** *Water weakens seal* [42]	**+** *Requires massive area* [43]	Alternating wet dry failures
	Magnetic	**+** *Solid state holding* [44]	**++** *Flux ignores water* [45]	**++** *Scales with area* [46]	Damages protective paint coatings
Contigutive	**Dry Adhesive**	**-** *Delicate micro structures* [47]	**- -** *Water blocks adhesion* [48]	**- -** *Complex scaling limits* [49]	Completely fails in saltwater

While the matrix identifies penetrative, form-closure, and magnetic gripping as high-potential candidates for general offshore use, their applicability to monopile upending is limited by specific operational constraints:

- **Penetrative gripping:** This robust method relies on material penetration. The penetration renders this gripping mechanism unsuitable, as DNV-ST-N001 guidelines [50] prohibit damage to the primary steel or anti-corrosion coating of the monopile.
- **Form-closure:** This mechanism relies on geometric features to support the load. However, monopiles are smooth tapered cylinders. Implementing form-closure would require welding (temporary) connection points to the outside of the monopile.
- **Magnetic gripping:** Magnetic flux generates force only normal to the surface. It provides no direct resistance to shear loads (gravity acting on the vertical pile) other than through friction [51]. That makes this method unsuitable for holding the monopile in both a horizontal and vertical orientation.

This elimination process leaves **friction-based gripping** as the only non-destructive, scalable, and structurally viable option for the proposed upending concept. Even though it scores lower on wet

performance due to the uncertainties of achieving consistent grip underwater, as the coefficient of friction (COF) varies significantly in lubricated marine environments. Consequently, characterizing this wet-friction uncertainty and translating it into safe, predictable clamping forces forms a fundamental challenge for the concept design. The physical mechanics governing this friction interface are detailed in Section 2.4.

2.4. Tribological Mechanics of Steel-Polymer Interfaces

The feasibility of the proposed upending concept relies for a significant part on the ability of the gripper interface to reliably transmit shear loads through friction. This section discusses the fundamental contact mechanics governing the steel-polymer interface and identifies risks associated with exposure to water as a lubricant.

2.4.1. Fundamentals

The gripping interface is a tribological system consisting of two bodies separated by a medium. The first body is the monopile, composed of S355 structural steel, which is partially protected by an anti-corrosion coating (Figure 2.12). The second body is the gripper pad, composed of the high-strength elastomers polyurethane (Figure 2.13), designed to conform to the steel surface and generate a high coefficient of friction (COF). The medium is seawater, which acts as a lubricant.

Figure 2.12: Monopile made of S355 steel, partly covered with a coating (right).

Figure 2.13: A polymer friction pad currently used by TWD for seafastening monopiles.

Friction is defined as the reaction force between two surfaces in contact. The two surfaces are subjected to a normal force [52]. A tangential force, perpendicular to the normal force, representing the monopile (MP) weight, acts to initiate relative motion of the surfaces. This motion is resisted by the friction force [53] (Figure 2.14).

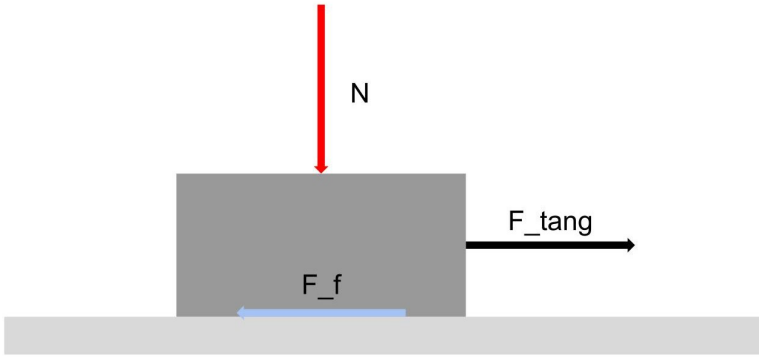

Figure 2.14: Forces acting on a friction interface.

The holding capacity is governed by the classical Coulomb friction model, where the maximum achievable friction force (F_f) is proportional to the normal force [53] [52]. In a static holding scenario, the applied tangential load (F_{tang}) must not exceed this limit [54] [55]:

$$F_f = \mu \cdot N \tag{2.1}$$

Equation 2.1 determines the clamping force required to hold the monopile. The coefficient of friction (μ) is not a constant, but a variable dependent on materials, contact pressure, surface roughness, and lubrication state.

2.4.2. Steel-Polymer Friction

Friction at the steel-polymer interface is derived from two mechanisms: adhesion and deformation [56]. Understanding the contribution of each helps predict performance in wet environments.

Adhesion refers to the intermolecular bonds (Van der Waals forces) formed between the polymer pad and the steel interface [57]. In the context of gripping a monopile in a wet lubricated environment, where contact pressures are in the megapascal (MPa) range, the adhesive component is negligible compared to the deformation component [58].

Consequently, deformation is the dominant mechanism. As the normal load increases, the polymer asperities (Figure 2.15) flatten and the material flows into the valleys of the steel roughness profile, activating viscoelastic hysteresis [57] [59]. As the hard steel asperities penetrate and slide against the polymer surface, the elastomer undergoes a continuous cycle of compression and relaxation. Due to the viscoelastic nature of the material, the energy stored during compression is not fully recovered during relaxation [56] (Figure 2.15). This dissipated energy functions as the tangential resistive force.

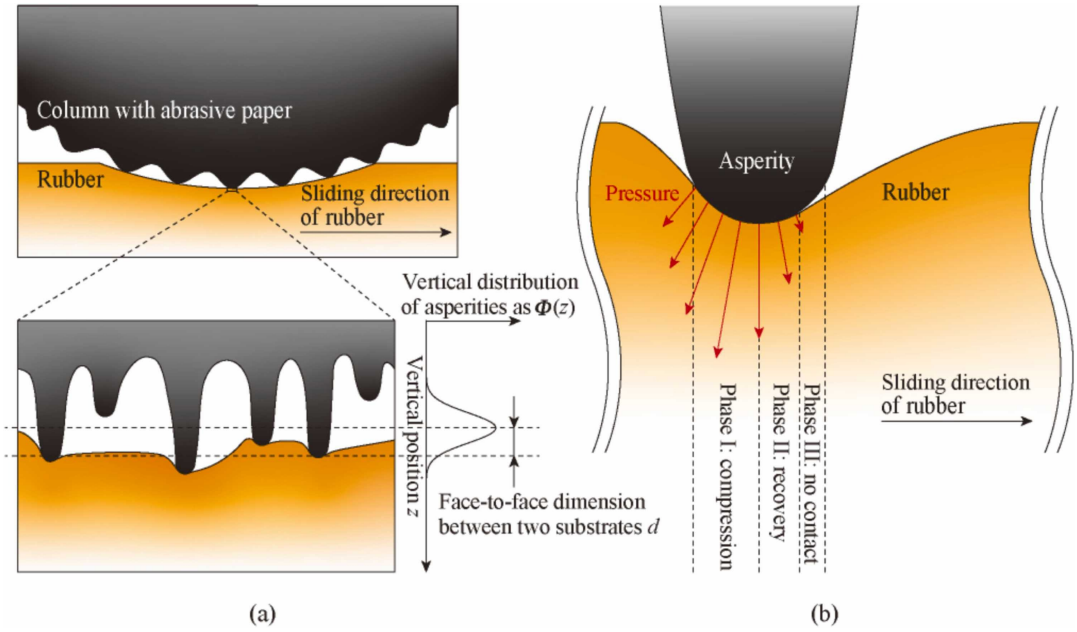

Figure 2.15: Mechanism of viscoelastic friction. (a) Cross-section showing the polymer (orange) conforming to a rough surface. (b) A single asperity showing the mechanism of viscoelastic hysteresis [56].

On a coarser scale, asperity ploughing adds additional mechanical resistance. This occurs when significant surface roughness causes steel peaks to physically shear through the polymer [59]. While ploughing actually contributes to friction and is largely independent of lubrication, it is destructive, leading to increased wear and potential fatigue damage to the gripper pads over repeated cycles [55].

2.4.3. Static vs Kinetic Friction

Friction is categorized into static friction, which acts on a body at rest, and kinetic friction, which opposes motion during slip. A distinction is made between the static COF (μ_s) and the kinetic COF (μ_k) [60].

Static friction is higher than kinetic friction [61]. This is because during static contact, the material allows for slowly increasing the real contact area, allowing junctions (microscopic point of real contact) to strengthen. When sliding begins, thus, kinetic friction, there is no time for these junctions to really form, resulting in a drop of resistance [62].

However, for the specific case of dry steel-polymer interaction, this drop is dampened (Figure 2.16). This is because the resistance is primarily governed by bulk deformation, or creep, rather than surface junction strengthening [61]. As the hard asperities indent the polymer, they create a deformation wave. Because the viscoelastic material requires time to recover, this deformation zone persists during motion [59]. Consequently, the force required to maintain the ploughing action is close to the force required to initiate it [62].

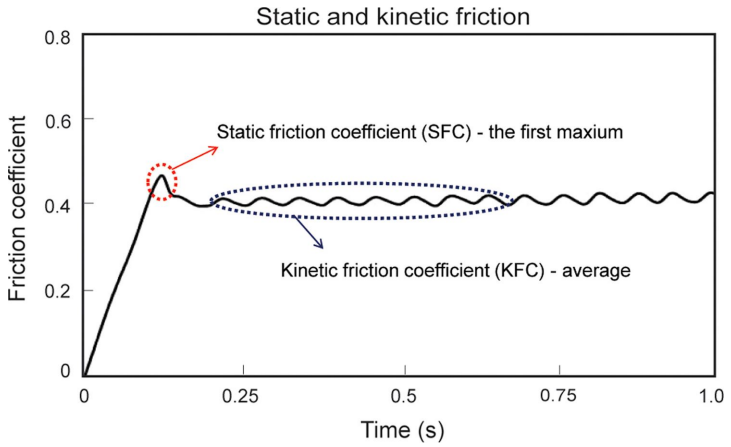

Figure 2.16: A representative polymer friction profile showing minimal difference in the static and kinetic friction coefficient [61].

2.4.4. Wet Conditions

When contact takes place in a wet environment, the presence of water changes the way friction is generated compared to dry surfaces. A thin film of water can enter the valleys between asperities and act as a lubricant, lowering the direct solid to solid contact [63]. As a result, both adhesion and frictional resistance are lowered [28].

The influence of a lubricant is described by the Stribeck curve [64], which relates the friction coefficient to viscosity, velocity, and load. This curve categorizes lubrication into three regimes: Boundary Lubrication (BL), Mixed Lubrication (ML), and Hydrodynamic Lubrication (HL), as shown in Figure 2.17.

The Stribeck curve demonstrates that an increasing presence of lubricant decreases the COF. For the proposed elastomer-steel interaction under high loads, the transition from a static to a kinetic state in wet conditions is critical:

- **Static state**, under high clamping pressure, the elastomer is pressed deep into the steel asperities. Locally displacing the water film from the contact peaks and under the high pressure of the system, the lubricant is slowly pushed out [65], going from an HL to an ML regime and slowly over time even move to a BL regime [53]. Resulting in higher static holding capacity even though a little bit of water is still present.
- **Kinetic state:** As soon as the monopile begins to slip, the movement brings water back into the interface, separating the surface asperities and pushing the contact into the ML regime. The result is a severe loss of friction: the system suffers a 'double drop' in COF driven by the transition from static to kinetic friction, amplified by the increased lubrication of the ML phase.

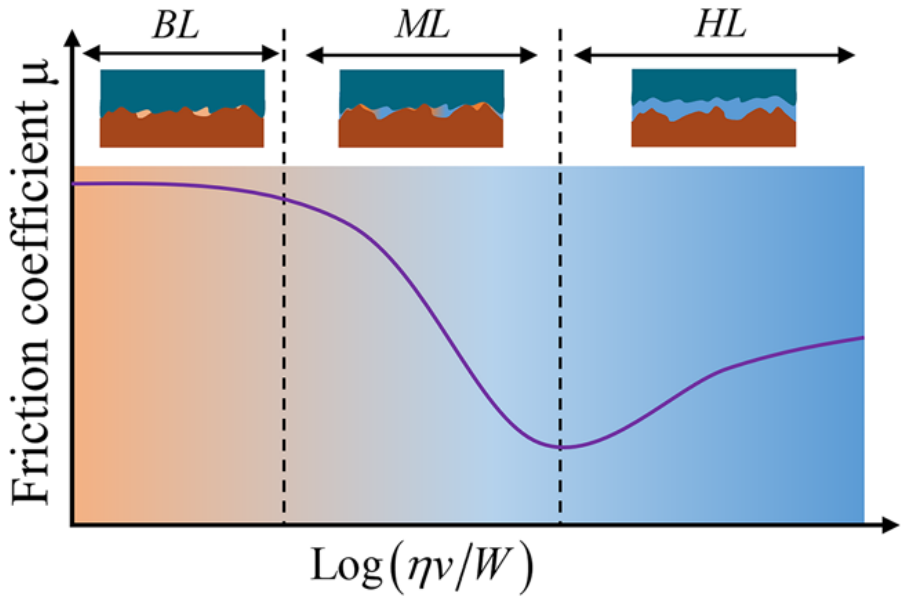

Figure 2.17: Stribeck curve illustrating the relationship between the coefficient of friction and the Hersey number (viscosity × velocity / load) [64].

2.4.5. Pressure Dependency

The classical Coulomb model assumes a constant coefficient of friction independent of normal load. However, this assumption is insufficient for polymeric materials under high stress [57]. In elastomeric pads the COF often exhibits a non-linear, inverse relationship with contact pressure [66] [67].

At low pressures, the elastomer deforms into the surface asperities, and the real area of contact increases linearly with the applied load, maintaining a constant COF. At high pressures, the elastomer fills the surface valleys completely, and the real contact area approaches the geometric area of the pad. Since the contact area cannot increase further, the friction force does not scale linearly with additional normal load, leading to a reduction in the effective μ [67].

2.4.6. Creep

In addition to pressure sensitivity, elastomers exhibit time-dependent behavior known as viscoelastic creep. Under a constant load, the polymer material continues to deform over time [68]. During the upending sequence, which may last several hours, this behavior has critical implications depending on the stiffness of the clamping system.

If the clamping mechanism is rigid (e.g., a screw jack or a hydraulically locked cylinder), the stress relaxation that results from this creep [55], causes a decrease in the effective normal force (N). To prevent slip, the hydraulic system must be active or compliant to compensate for this relaxation and maintain constant clamping pressure.

2.4.7. Surface Roughness and Coatings

As the preceding paragraphs explain is that the friction performance is largely influenced by the surface topography of the monopile [69].

Monopiles are typically partly protected by anti-corrosion coatings, see Figure 2.12. These coatings often result in a smoother finish compared to the partially corroded untreated surface of the monopile.

In dry conditions, for light structures a smoother surface could enhance friction by maximizing the contact area for adhesion [59]. However, in wet heavy lifting conditions, a smooth surface is actually decreasing the friction performance. A degree of surface roughness is essential to penetrate the fluid film. A surface that is too smooth may fail to pierce the water film, leading to a state of hydrodynamic lubrication and thus a significantly reduced COF.

2.4.8. Temperature

Sub-zero temperatures introduce a severe risk of icing. If the air temperature drops below $0°$C during the upending sequence, residual water trapped within the interface can rapidly freeze. This ice layer acts as a solid lubricant, causing a substantial reduction in the coefficient of friction [70] and risking immediate slip. Consequently, to ensure a secure frictional hold, the upending operation must be strictly restricted to ambient weather windows above freezing ($T > 0°$C).

2.4.9. Implications for Designing

This friction review leads to the conclusion that steel-polymer friction is not a constant value. Consequently, the Local Structural Model from Chapter 5 will not treat friction as a single scalar input. Instead, it will be modeled as a variable parameter driven by the following considerations and limitations:

- **Wet Limitation:** Due to the risk of water lubrication, a conservative lower bound for μ will be selected representing the wet/submerged condition.
- **Pressure Saturation:** The non-linear inverse relation between COF and applied force implies that increasing clamping force is only effective up to a specific saturation point. Beyond this threshold, higher pressure yields minimal friction gains while significantly increasing structural loads on the monopile.
- **Coating:** The gripper interface may be positioned on a coated section, a transition zone, or an uncoated section depending on the MP design and gripping location. Therefore, the friction coefficient is not uniform along the length of the monopile. The interface combination that yields the lowest friction coefficient will be chosen.
- **Wear and Tear:** The forces that act on the friction pads are considered to be very high. The pads will damage a lot. Therefore, the pads will probably have to be replaced after each project (e.g. installing the monopiles for a specific windpark).
- **Temperature:** The operations cannot be performed when the atmospheric temperature is below zero degrees, since the COF could drastically drop when a layer of ice is formed on the surface.

3

System Definition

Before diving into the dynamic modeling of the craneless upending operation, it is essential to establish a robust framework governing the physical system and its environment. This chapter defines the fundamental building blocks required for the analytical model, including the used coordinate systems, the monopile dimensions, the hydrodynamic environment definition, the system requirements, and the assumptions made.

3.1. Global and Local Coordinate Frames

To model the kinematics of the monopile and the hydrodynamic loads exerted upon it, two coordinate systems are defined: a stationary global frame and a rotating local frame, as illustrated in Figure 3.1. These coordinate frames will be used for modeling and describing the system.

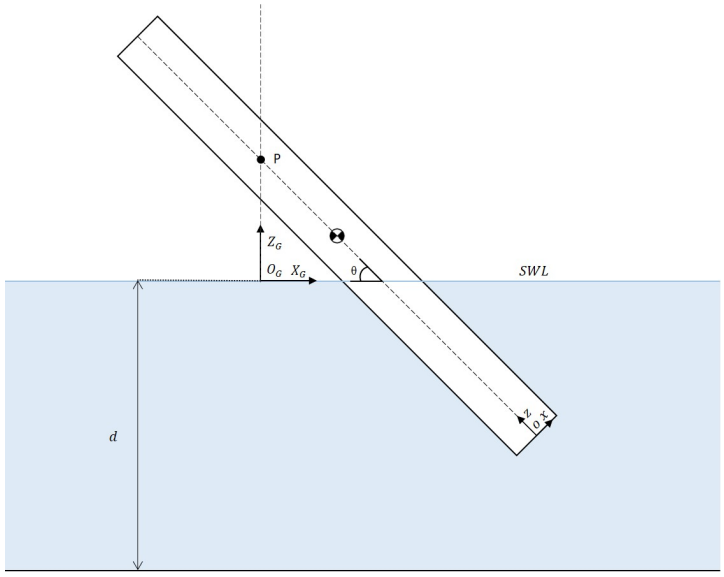

Figure 3.1: Definition of the global (X_G, Z_G) and local (x, z) coordinate systems, illustrating the rotational pitch angle (θ) and the water depth (d).

The Global Coordinate System (X_G, Z_G)

The global reference frame is an earth-fixed, two-dimensional system.

- **Origin (O):** The origin is located exactly at the Still Water Level (SWL), directly vertically aligned with the mechanical pivot point (P) of the gripper.

- **Z-Axis (Z_G):** Defines the vertical elevation. Positive values denote positions above the SWL (in the air), while negative values denote submerged positions. The seabed acts as a hard boundary condition at $Z_G = -d$ (where $d = 50$ m). The dashed vertical line indicates the movement the pivot point can make.
- **X-Axis (X_G):** Defines the horizontal distance parallel to the SWL.

The Local Coordinate System (x, z)
The local reference frame is a body-fixed system that rotates with the monopile during the upending sequence.

- **Origin (o):** The local origin is fixed at the bottom of the monopile.
- **z-Axis (z):** Runs parallel to the longitudinal centerline of the monopile.
- **x-Axis (x):** Runs perpendicular to the monopile centerline (transverse direction).

Orientation and Geometric Boundaries
The relationship between the local and global frames is defined by the pitch angle (θ). A horizontal, floating monopile corresponds to $\theta \approx 0°$, while a fully upended, vertical monopile corresponds to $\theta = 90°$.

By establishing these two frames, all movements can be defined. Lastly, the lower tip of the monopile must not clash with the seabed boundary limit ($Z_{G,tip} > -d$) at any point during the θ progression.

3.2. System Kinematics and Degrees of Freedom

To establish a clear mathematical framework for the upending operation, the standard six degrees of freedom (6-DoF) are defined, as illustrated in Figure 3.2. These definitions govern the translational motions (surge, sway, heave) and rotational motions (roll, pitch, yaw).

Because this operation relies on a bottom-fixed Jack-Up Vessel (JUV) planted firmly on the seabed, the vessel hull is considered entirely stationary during the installation phase. Consequently, the wave-induced translational and rotational motions of the vessel itself are assumed to be zero. This stationary platform provides a rigid base for the installation equipment.

These same standardized 6 DoF definitions are utilized to define the kinematics of the proposed gripper concept and the payload. By locking the inactive degrees of freedom, the complex upending maneuver is simplified into a controlled, two-dimensional operational plane:

- **Gripper Translation (Heave):** The gripper assembly can only move vertically along the global Z_G-axis.
- **Monopile Rotation (Pitch):** The mechanical hinge at the gripper's pivot point allows the monopile to rotate exclusively around the Y-axis. This rotation defines the pitch angle (θ) of the monopile as it transitions from a horizontal floating state to a fully vertical orientation.

All other relative degrees of freedom are assumed to be rigidly constrained by the clamping mechanics of the gripper structure. These kinematic boundary conditions ease the modeling process in Chapter 4.

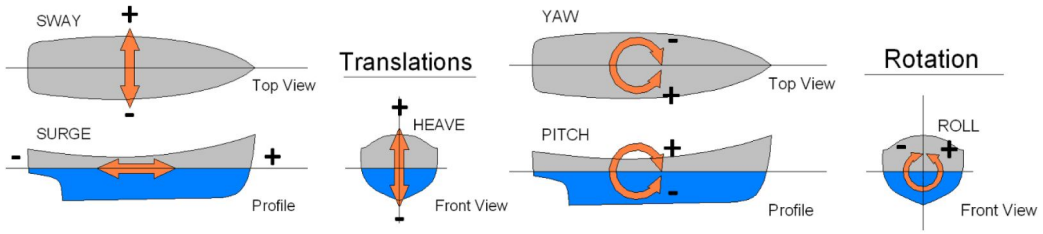

Figure 3.2: Vessel motions as defined by TWD [71].

3.3. Monopile Specifications

The reference monopile is based on dimensions from a 2025 project by TWD [71]. The resulting properties are representative of a next-generation XXL monopile featuring a conical upper section. Within a given wind farm project, monopiles typically share a common upper diameter. While the bottom diameter varies within a wind farm project, this thesis considers the fixed dimensions defined below. The diameter is increased toward the lower section of the monopile to withstand the higher bending moments and axial forces acting at the base. The resulting reference geometry is used as a fixed input for the modeling performed in the next chapters.

The geometry and specifications of the monopile are shown in Figure 3.3 and elaborated in Table 3.1. Despite its tapered geometry, the center of gravity is assumed to be located at the midpoint of the monopile. The structure consists of multiple steel sections (cans) with varying wall thicknesses; however, for the purposes of this study, an average wall thickness t of 110 mm is assumed.

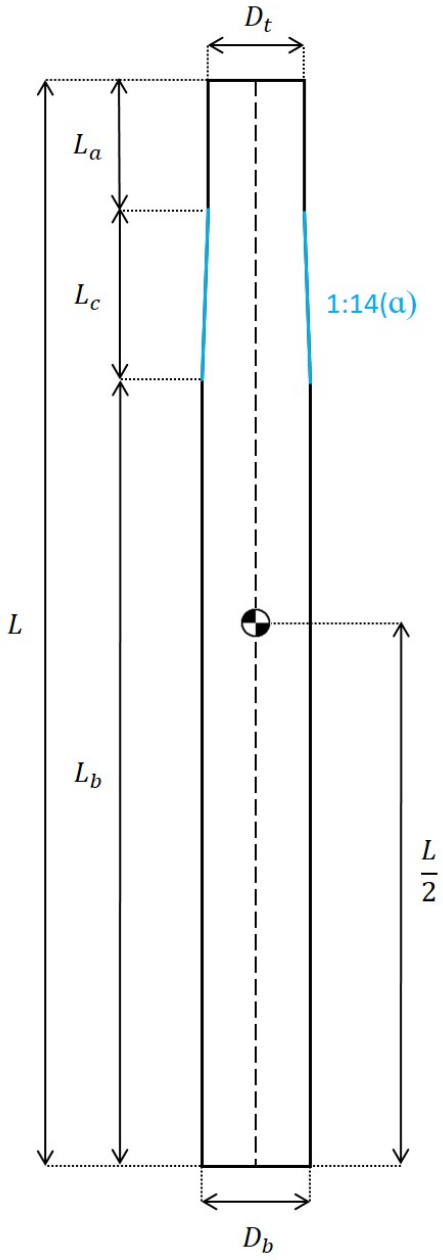

Figure 3.3: Dimensions of the monopile.

Parameter	Symbol	Value	Unit
Diameter Bottom	D_b	9	m
Diameter Top	D_t	8	m
Length Total	L	90	m
Length Before Conical Section	L_b	65	m
Length Conical Section	L_c	14	m
Length After Conical Section	L_a	11	m
Thickness	t_{mp}	110	mm
Cone Inclination	α	4.1	$^\circ$
Center of Gravity	CoG	45	m
Monopile Mass	m_{mp}	2170	t
Density Steel	ρ_s	7850	kg/m^3

Table 3.1: Specifications of the monopile considered in this study.

3.4. Hydrodynamic Environment & Wave Kinematics

The upending operation is a process occurring within the offshore splash zone, making it highly sensitive to environmental loads. Unlike standard lifting operations where a payload is hoisted quickly away from wave action, ballast-assisted upending is a slower process where the structure remains exposed to hydrodynamic excitation for a longer duration. Consequently, the system is designed for a restricted weather window in accordance with DNV-ST-N001 [50].

The design sea state, summarized in Table 3.2, considers a typical North Sea offshore environment during the summer installation season. The operation is restricted to mild sea states with a significant wave height of $H_s \leq 2.0$ m to minimize dynamic structural demands. A steady current velocity (v_c) is incorporated via linear superposition to account for steady drag moments [72]. The fundamental terminology and geometric definitions for the wave environment are illustrated in Figure 3.4.

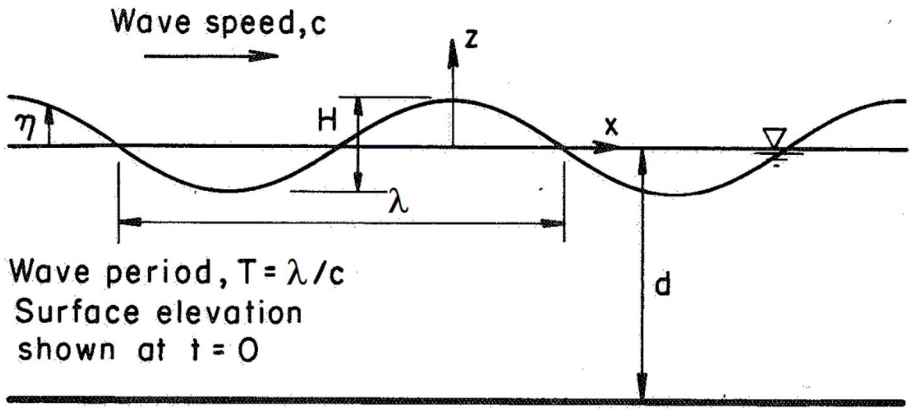

Figure 3.4: Definition sketch and terminology for regular wave theory, illustrating the water depth d [73].

Table 3.2: Environmental design parameters for the upending sequence.

Parameter	Symbol	Value	Unit
Significant wave height	H_s	2.0	m
Peak wave period	T_p	10.0	s
Current velocity	v_c	1.0	m/s
Water depth	d	50	m
Seawater density	ρ_w	1025	kg/m^3
Monopile outer diameter	D_o	9.0	m

Load Model Selection & Theory Verification

To ensure the mathematical load model represents the environmental interaction, the hydrodynamic regime is verified using three distinct industry-standard criteria. The process begins with the dispersion relation [74] to solve for the wavelength ($\lambda \approx 151$ m):

$$\lambda = \frac{gT_p^2}{2\pi} \tanh\left(\frac{2\pi d}{\lambda}\right) \tag{3.1}$$

The applicability of the chosen modeling framework is confirmed as follows:

- **Wave Kinematics (DNV Theory Validity):** Using the dimensionless parameters derived from Table 3.2, the design sea state is mapped onto Figure 3.5a, retrieved from DNV-RP-C205 Section

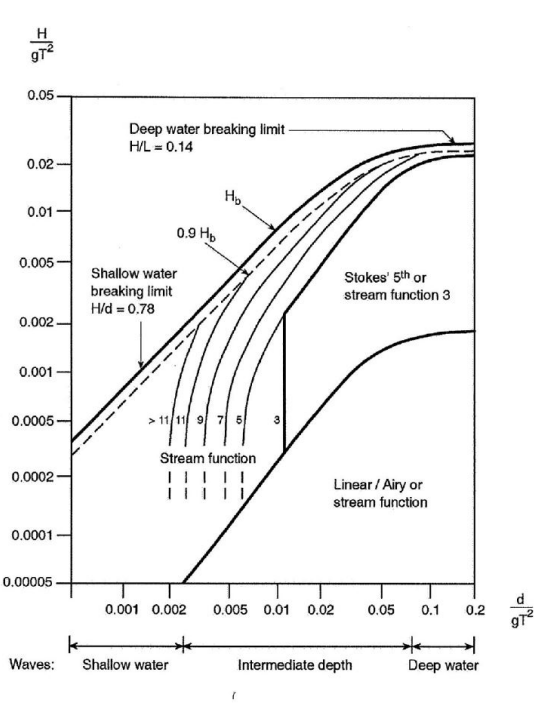

(a) Theory validity range. The design point $(H/gT^2 \approx 0.002, d/gT^2 \approx 0.05)$ justifies Linear Airy theory [73].

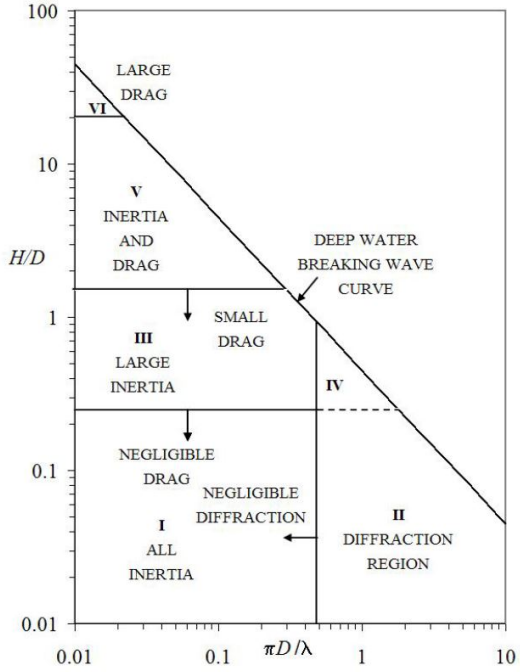

(b) Wave force regimes. The design point $(\pi D_o/\lambda \approx 0.18, H/D_o \approx 0.22)$ confirms a regime of negligible diffraction [75].

Figure 3.5: Hydrodynamic verification charts according to DNV-RP-C205 [73]. The combination of these criteria validates the use of Linear Airy wave kinematics and the Morison load formulation.

3.3 "Wave Kinematics" [73]. The dimensionless coordinates ($H_s/gT_p^2 \approx 0.002, d/gT_p^2 \approx 0.05$) fall deep within the Linear/Airy region. This justifies the exclusion of higher-order wave theories, as non-linear steepness effects ($U_R \approx 0.36 \ll 10$) are negligible.

- **Load Formulation (Diffraction Regime):** The scattering parameter ($\pi D_o/\lambda \approx 0.18$) is evaluated against the diffraction threshold in Figure 3.5b, as retrieved from DNV-RP-N103 Section 2.3 "Wave loads on large volume structures" [75]. Since the diffraction parameter is well below the threshold ($D_o/\lambda \approx 0.06 < 0.2$), the monopile operates in the *Slender Body Regime*. This indicates that the diffraction method is not required, making the relative-velocity **Morison Equation** [76] an appropriate formulation for load calculation.
- **Force Regime (Keulegan-Carpenter Number):** The KC number is calculated using the surface horizontal velocity ($u_{max} \approx 0.65$ m/s) [73]:

$$KC = \frac{u_{max} T_p}{D_o} \approx 0.72 \tag{3.2}$$

The result ($KC < 5$) indicates an **inertia-dominated** regime. This is visually confirmed in Figure 3.6, where the inertia force peaks at ~ 1250 kN, while the drag force is significantly smaller. While the mass term provides the primary wave excitation, the drag term is retained to provide the essential hydrodynamic damping required for the relative-velocity formulation.

Based on Linear Airy Wave Theory, retrieved from DNV-RP-C205 'Table 3-1 linear and second-order wave theory' [73] the undisturbed horizontal ($u, \dot{u}$) and vertical ($w, \dot{w}$) water particle kinematics at any global vertical coordinate $Z_G \leq 0$ and horizontal coordinate X_G are defined as:

$$u(X_G, Z_G, t) = \frac{\pi H_s}{T_p} \frac{\cosh(k(Z_G + d))}{\sinh(kd)} \cos(kX_G - \omega t) + v_c \tag{3.3}$$

$$\dot{u}(X_G, Z_G, t) = \frac{2\pi^2 H_s}{T_p^2} \frac{\cosh(k(Z_G + d))}{\sinh(kd)} \sin(kX_G - \omega t) \tag{3.4}$$

$$w(X_G, Z_G, t) = \frac{\pi H_s}{T_p} \frac{\sinh(k(Z_G + d))}{\sinh(kd)} \sin(kX_G - \omega t) \tag{3.5}$$

$$\dot{w}(X_G, Z_G, t) = -\frac{2\pi^2 H_s}{T_p^2} \frac{\sinh(k(Z_G + d))}{\sinh(kd)} \cos(kX_G - \omega t) \tag{3.6}$$

where k is the wave number ($2\pi/\lambda$) and ω is the angular frequency ($2\pi/T_p$). The variable Z_G represents the vertical coordinate measured upwards from the Still Water Level (SWL). Consequently, $Z_G = 0$ at the surface and $Z_G = -d$ at the seabed.

The right plot in Figure 3.6 illustrates how this formulation results in an exponential decay of wave influence with increasing depth (as Z_G becomes more negative).

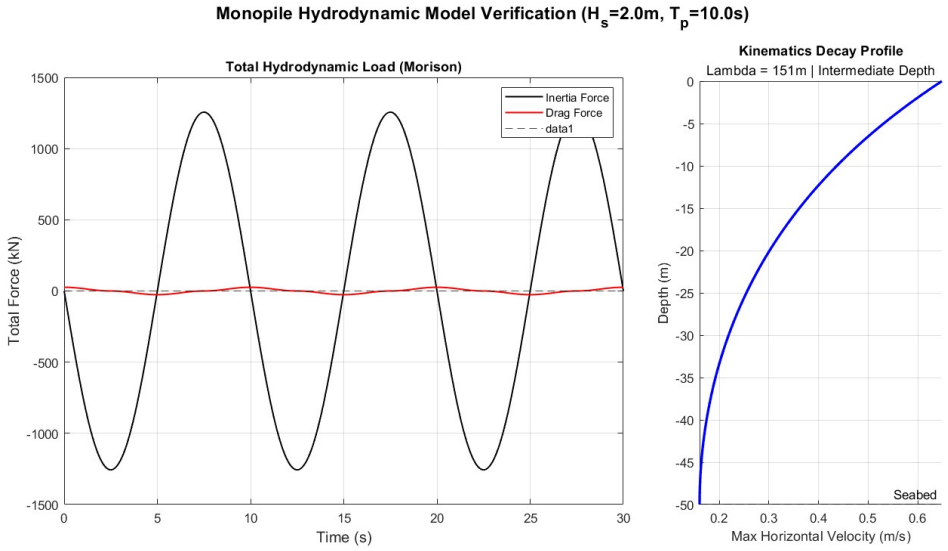

Figure 3.6: Hydrodynamic verification dashboard generated via MATLAB. The simulation confirms inertia dominance and illustrates the exponential decay of horizontal velocity with depth.

Modeling Simplification: Truncated Linear Theory

To compute the total hydrodynamic drag and inertia forces, the wave kinematics are integrated from the seabed ($Z_G = -d$) up to the Still Water Level (SWL, $Z_G = 0$). While methods such as Wheeler Stretching [77] can be used to extrapolate kinematics to the instantaneous free surface, Morison et al. [76] established that neglecting the integration between the trough and crest has a generally small effect for unbroken waves. Given that the significant wave height ($H_s = 2.0$m) in this study is very small relative to the total water depth ($d = 50$ m), omitting the crest kinematics yields negligible differences in the total integrated global loads. This truncated approach is adopted to prioritize the numerical stability of the global upending solution without sacrificing engineering accuracy.

Normal Velocity Projection

As the monopile rotates from near-horizontal ($\theta \approx 0°$) to fully vertical ($\theta \approx 90°$), the loads are governed by the fluid components acting normal to the pile's longitudinal axis. The normal water velocity (u_n) and the normal fluid acceleration ($\dot{u}_n$) at any given time and orientation are derived via trigonometric projection of the global kinematics:

$$u_n(z, t, \theta) = u(X_G, Z_G, t) \sin(\theta) + w(X_G, Z_G, t) \cos(\theta) \tag{3.7}$$

$$\dot{u}_n(z, t, \theta) = \dot{u}(X_G, Z_G, t) \sin(\theta) + \dot{w}(X_G, Z_G, t) \cos(\theta) \tag{3.8}$$

3.5. System Requirements

To systematically evaluate the feasibility of the proposed craneless upending method, design requirements must be established. These criteria dictate the functional, structural, and operational boundaries that the conceptual design must satisfy to be deemed successful.

3.5.1. Functional and Operational Requirements

- **Kinematic Goal:** The system must successfully transition the monopile from a horizontal floating state to a fully vertical 90-degree orientation.
- **Hydrostatic Stability:** Upon reaching verticality, the system must hold the monopile in a stable, controlled manner, to prepare for the subsequent seabed driving phase.
- **Seabed Clearance:** A minimum safety clearance of 3 meters between the monopile bottom and the seabed must be maintained throughout the entire dynamic upending sequence.
- **Environmental Workability:** The system must be able to perform the upending maneuver within the defined operational sea state envelope (defined in section 3.4).
- **Vessel Compatibility:** The operation must be performed from a Jack-Up Vessel (JUV), entirely eliminating the need for a Heavy Lift Vessel (HLV).

3.5.2. Structural and Interface Requirements

- **No Monopile Alterations:** The handling method must rely purely on surface friction. No temporary or permanent structural modifications (such as welded lifting lugs, trunnions, or push-points) may be added to the monopile geometry.
- **Structural Integrity:** The normal forces exerted by the gripper must not induce local yielding, plastic deformation, or global cross-sectional buckling of the thin-walled monopile shell.

3.5.3. Safety and Reliability Requirements

- **Engagement Safety:** The gripper must safely engage the floating monopile without causing structural damage. The mechanism must be capable of accommodating minor presentation misalignments when closing to ensure safe and secure engagement.
- **Fail-Safe Grip:** The actuation system must incorporate a fail-safe mechanism (e.g., mechanical lock-nuts) to ensure the frictional hold is securely maintained even in the event of a total hydraulic pressure loss.

3.6. Assumptions

While the system requirements establish the boundaries for a successful physical operation, modeling the complex interaction of hydrodynamics, structural mechanics, and tribology requires establishing a controlled analytical environment. To facilitate the mathematical and numerical models presented in the subsequent chapters, the following assumptions and simplifications have been applied:

- **Structural Integrity:** The gripper structure is assumed to be rigid and designed with sufficient capacity to transfer all reaction forces.
- **Planar Kinematics:** The upending maneuver is modeled as a two-dimensional planar motion. Out-of-plane movements, such as yaw, roll, and transverse sway of the monopile, are assumed to be perfectly restrained by the structural stiffness of the gripper system.
- **Ballast Dynamics (Quasi-Static):** To facilitate the parametric grid search, the internal ballast water in the quasi-static model is treated as a ”frozen” solid mass. The dynamic time-domain model subsequently lifts this assumption by incorporating the Free Surface Effect (FSE) of the fluid.
- **Monopile Geometry:** The monopile is modeled as a perfect cylinder with a uniform diameter of 9 m and a uniform thickness of 110 mm for the hydrodynamic analysis.
- **Stationary Installation Platform:** The operation is assumed to take place from a bottom-fixed Jack-Up Vessel (JUV). Consequently, wave-induced translational and rotational vessel motions are assumed to be zero, providing a perfectly rigid global reference frame.

- **Wind Loads:** Aerodynamic loads on the upper monopile section are deemed insignificant compared to hydrodynamic and gravitational loads.
- **Wave Kinematics (Truncated Theory):** Wave kinematics are evaluated using Linear Airy Theory and are cut off at the Still Water Level (SWL). Forces generated by wave crests above the SWL (splash zone) are neglected to avoid further complicating the numerical modeling.
- **Regular Waves:** The hydrodynamic environment is modeled using a singular sinusoidal wave defined by the design sea state parameters (H_s and T_p). Real-world offshore sea states consist of a superposition of multiple wave frequencies and varying amplitudes (an irregular wave spectrum). By not considering irregular waves, a simplified time-domain simulation is generated.

4

Global Upending Dynamics

The objective of the global upending model is to simulate the behavior and stability of the monopile as it transitions from a floating horizontal state to a vertical orientation. This analysis is performed through two distinct yet complementary modeling approaches. Initially, a quasi-static model is introduced as a tool for sensitivity analysis, allowing for the evaluation of how the global parameters 'pivot offset (z_{off})' and 'pivot height ($Z_{G,P}$)' influence the load envelope acting on the gripper and the required ballast fill (z_{fill}). Subsequently, a dynamic model is implemented to capture the time-dependent evolution of the process, incorporating pump flow rates, jacking velocities, and environmental disturbances. Together, these models define the boundary conditions, the global parameters, and load envelope required to perform the local structural design checks of the gripper interface and for the development of the final concept.

4.1. Static Equilibrium

The core mechanism of the craneless upending concept is the manipulation of static forces to achieve a controlled rotation. The system's behavior is governed by the interaction between gravitational loads, hydrostatic buoyancy, and the kinematic constraints imposed by the gripper at the pivot point. By adjusting the internal ballast and the vertical position of the gripper, the monopile's rotation is effectively treated as a succession of quasi-static equilibrium states.

4.1.1. Free Body Diagram

To analyze the governing physics, the monopile is modeled as a rigid cylindrical body. For the static equilibrium, environmental loads such as waves and drag are omitted to isolate the fundamental drivers. In this study, the monopile is modeled as a uniform cylinder to simplify the calculation of submerged volume and mass distribution. The influence of the conical section is accounted for as a geometric constraint; the gripper pivot point must be located under the cylindrical sections to ensure a uniform clamping surface and avoid pressurizing the tapered region.

As illustrated in Figure 4.1, three types of forces act on the body during the upending sequence: the dry gravitational force of the monopile steel (W_{mp}), the gravitational force of the ballast mass (W_{bal}) and the buoyancy force (F_B).

Gravitational Forces

The total weight consists of the dry monopile weight (W_{mp}) acting at the center of gravity (G) and the ballast mass weight (W_{bal}) acting at the geometric center of the internal water ballast (C). Assuming a uniform cylindrical geometry, the monopile gravitational force is defined as:

$$W_{mp} = M_{mp} \cdot g = (\rho_s \cdot A_{mp} \cdot L) \cdot g \tag{4.1}$$

Where g is the acceleration due to gravity, A_{mp} is the surface area of a monopile slice and L is the length of the monopile.

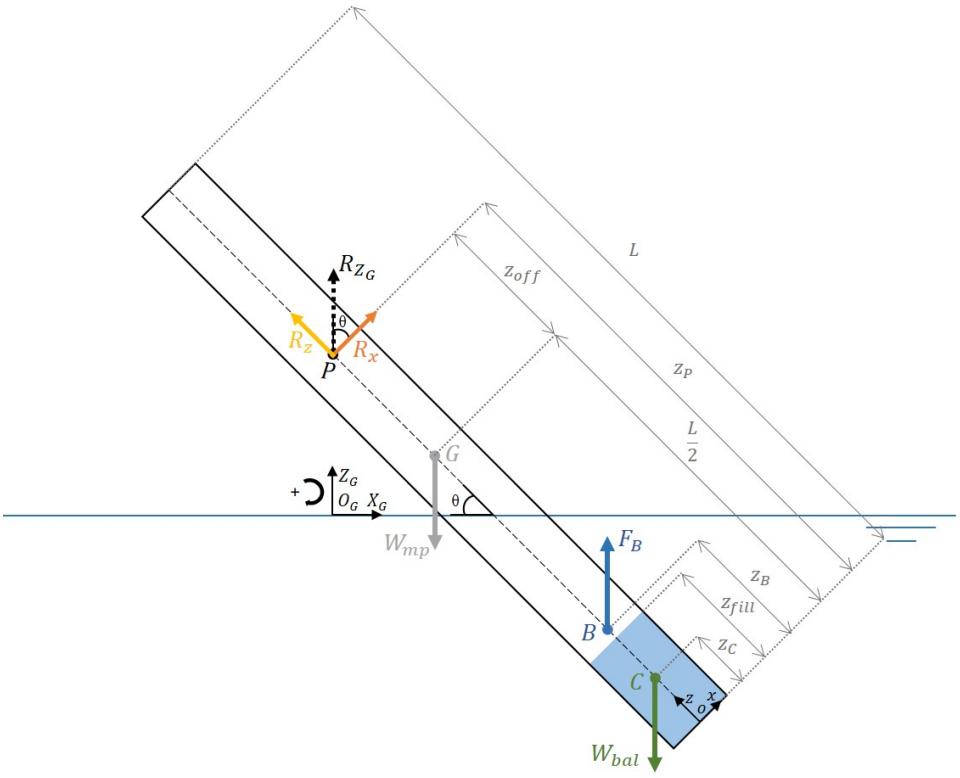

Figure 4.1: Free body diagram of the static system, showing the three main acting forces and the reaction forces at the gripper.

The ballast weight is a function of the internal fill height z_{fill}, the seawater density (ρ_w) and the internal cross-sectional area A_i:

$$W_{bal} = m_{bal} \cdot g = (\rho_w \cdot A_i \cdot z_{fill}) \cdot g \tag{4.2}$$

While z_{fill} is a fixed parameter for any specific static equilibrium state, it becomes a time-dependent variable $z_{fill}(t)$ in the dynamic simulation.

Assumption: The "Frozen" Ballast Mass

For the quasi-static equilibrium analysis and the subsequent parametric design space exploration, the internal water ballast is modeled as a ”frozen” solid mass. This implies that the center of gravity of the ballast (C) is assumed to remain fixed at the geometric center of the fill volume ($z_{fill}/2$) relative to the monopile's local longitudinal axis, regardless of the pitch angle θ.

In reality, liquid ballast experiences a Free Surface Effect (FSE), where the water level remains horizontal and the center of mass shifts towards the lower side of the inclined cylinder. However, modeling this shifting fluid center for thousands of iterations during a multi-variable grid search would introduce huge computational overhead. Because the quasi-static model primarily serves to determine the pivot height and pivot offset, the frozen ballast assumption provides a computationally efficient approximation. The Free Surface Effect of the ballast water is introduced in the dynamic time-domain model (Section 4.5) to capture the most realistic behavior of the system.

Buoyancy Force

The buoyancy force (F_B) acts vertically upwards through the center of buoyancy (B), representing the weight of the displaced water according to Archimedes' principle:

$$F_B = \rho_w \cdot g \cdot V_{sub} \tag{4.3}$$

where V_{sub} is the submerged volume of the cylindrical monopile, which varies based on the rotation angle θ and the vertical position of the pivot point.

Gripper Reaction Forces

The gripper pivot (P) serves as a kinematic constraint that permits only rotational motion. Consequently, reaction forces (R_x and R_z) are generated in response to the combined gravitational and hydrostatic loads. These reactions define the boundary conditions of the local gripper interface:

- **Transverse Force (R_x):** This component represents the load acting perpendicular to the monopile's longitudinal axis. It defines the structural demand on the gripper arms and the local crushing loads on the shell.
- **Axial Force (R_z):** This component represents the load acting along the monopile's longitudinal axis. To maintain a stable equilibrium and prevent the monopile from slipping, R_z must be entirely countered by the friction generated at the contact interface. Therefore, R_z dictates the minimum required frictional holding capacity of the gripper at any given orientation.

These reaction forces comprise the load envelope used in Chapter 5 to evaluate the risk of slip and local shell buckling.

4.1.2. Equilibrium Equations

For the system to maintain a quasi-static equilibrium state at a given angle θ, the sum of all forces and moments acting on the body must be zero.

Translational Equilibrium

The equilibrium of forces is solved in the global coordinate system (O_G, X_G, Z_G). Since the reaction forces R_x and R_z are defined in the local frame of the monopile, they are transformed using the rotation angle θ:

$$\sum F_{X_G} = R_x \sin(\theta) - R_z \cos(\theta) = 0 \tag{4.4}$$

$$\sum F_{Z_G} = F_B - W_{mp} - W_{bal} + R_x \cos(\theta) + R_z \sin(\theta) = 0 \tag{4.5}$$

Moment Equilibrium

The upending motion is governed by the balance of moments about the pivot point P. The equilibrium is defined by the three distinct physical components: the hydrostatic buoyancy moment (M_B), the monopile gravity moment (M_{mp}), and the ballast gravity moment (M_{bal}).

$$\sum M_P = 0 \quad \Rightarrow \quad M_B - M_{mp} - M_{bal} = 0 \tag{4.6}$$

Applying the trigonometric relations defined in Figure 4.1 to project the local longitudinal distances onto the global horizontal lever arm, the individual moment magnitudes are:

$$M_{mp} = W_{mp} \left(z_p - \frac{L}{2} \right) \cos(\theta) \tag{4.7}$$

$$M_{bal} = W_{bal}(z_p - z_C) \cos(\theta) \tag{4.8}$$

$$M_B = F_B(z_p - z_B) \cos(\theta) \tag{4.9}$$

Substituting these definitions back into the general equilibrium equation (Eq. 4.6) yields the expanded static balance:

$$F_B(z_p - z_B) \cos(\theta) - W_{mp} \left(z_p - \frac{L}{2} \right) \cos(\theta) - W_{bal}(z_p - z_C) \cos(\theta) = 0 \tag{4.10}$$

Although the $\cos(\theta)$ term appears in every component and could be mathematically divided out, it is kept in the formulation. This ensures the model correctly represents the true physical magnitude of the moments acting on the system, which is critical for maintaining numerical solver sensitivity and accurately calculating the gripper reaction forces as the monopile approaches verticality.

4.2. Quasi-Static Analysis

The analytical equations derived in Section 4.1 establish the fundamental physics of the upending process. Because the submerged volume and the position of the center of buoyancy change non-linearly with the rotation angle θ, a solely analytical solution is highly impractical. Therefore, a numerical quasi-static model is implemented to evaluate the system. The objective of this quasi-static model is to simulate the sequence of equilibrium states, determine the ballast mass, and extract the resulting reaction forces (R_x, R_z) at the gripper interface.

To extract this information, there are three global parameters that can be influenced, as illustrated in Figure 4.2:

1. **The pivot offset (z_{off}):** The longitudinal distance between the gripper connection point (pivot point) and the monopile's dry Center of Gravity (CoG).
2. **The global pivot height ($Z_{G,P}$):** The vertical position of the hinge point of the gripper relative to the water line, the vertical position is controlled by the jacking system.
3. **The ballast fill (z_{fill}):** The ballast water height that is the result of seawater that is pumped into the monopile and is collected in the lower end of the monopile. This ballast water height is directly linked with the ballast mass (M_{bal}) by geometry calculations.

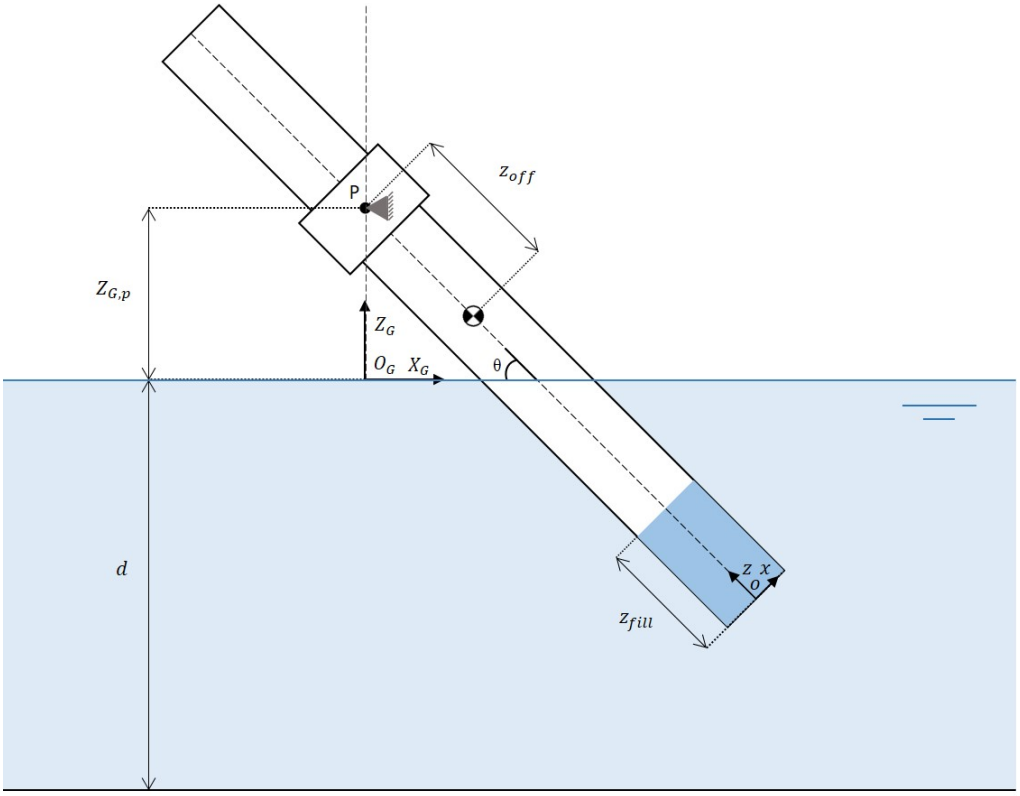

Figure 4.2: Schematic representation of the system variables: z_{off}, z_{fill}, $Z_{G,P}$. It shows the monopile in a certain orientation θ. d is the distance to seabed. The gripper pivot (P) is connected to the jacking structure (not shown in this schematic) for vertical movement.

The pivot offset (z_{off}) is fixed after engagement with the monopile. The other two variables ($Z_{G,P}$ and z_{fill}), will be able to be controlled during upending. The Quasi-static analysis' goal is to find what the final values of these control variables should be. By systematically varying the control parameters, this model facilitates a parametric sensitivity study to identify a feasible design space that minimizes the structural demand on the gripper while avoiding seabed collision.

The Geometrical parameters of Figure 4.2 are laid out in Table 4.1. The maximum pivot offset is driven by where the conical section starts and the minimum pivot offset is at the MP CoG.

Table 4.1: Geometrical parameters.

Parameter	Symbol	Value	Unit
Max Pivot Height	$Z_{G,P,max}$	20	m
Min Pivot Height	$Z_{G,P,min}$	0	m
Max Pivot Offset	$z_{off,max}$	20	m
Min Pivot Offset	$z_{off,min}$	0	m
Water depth	d	50	m

4.2.1. Numerical Implementation and Buoyancy Model

The quasi-static model evaluates the upending sequence by treating the continuous rotation as a series of discrete static equilibrium states. The system is governed by two independent input variables: the physical geometry of the setup ($Z_{G,P}$, z_{off}) and the internal ballast fill height (z_{fill}). For the purpose of this static boundary exploration, the ballast water is modeled as a solid, ”frozen” mass.

To accurately capture the highly non-linear buoyancy moments during rotation, the monopile is modeled using a numerical 1D Strip Theory approach. The total length of the pile is discretized into longitudinal elements. For each iterative time step and pitch angle, the model geometrically evaluates the intersection of the external waterline with each discrete circular cross-section to calculate the exact submerged volume and local buoyant force. The complete mathematical derivation of this numerical strip model, including the formulation of the partially submerged circular segments, is detailed in Appendix B.1.

For any given configuration and ballast fill, the model utilizes an iterative numerical root-finding algorithm to solve the moment equilibrium equation (Equation 4.10). The algorithm calculates the specific angle θ at which the net driving moment from gravity perfectly balances the restoring moment from the numerical buoyancy ($\sum M_P = 0$). Once the corresponding θ is achieved for every system state, the model solves the translational force balance (Equations 4.4 and 4.5) to determine the gripper reaction forces.

4.2.2. Quasi-Static Upending Results

The upending sequence of the quasi-static solution is presented, with an average configuration of the design variables ($z_{off}, Z_{G,P}$) of (10 m, 10 m) in Figure 4.3

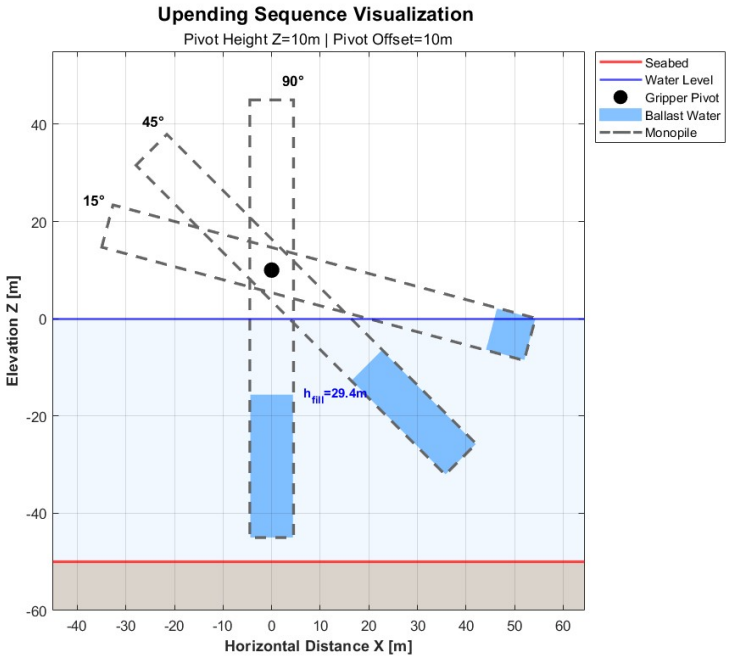

Figure 4.3: Kinematic visualization of the monopile upending sequence where varying pile angles ($15°$, $45°$, and $90°$) are shown.

Figure 4.4 shows the seabed clearance of this configuration and the required ballast mass for every angle. It can be seen from the angle 60 to 90 degrees, that only a very small extra ballast fill is required to rotate the pile a large distance. This implies that the last part of the upending will happen quite quickly.

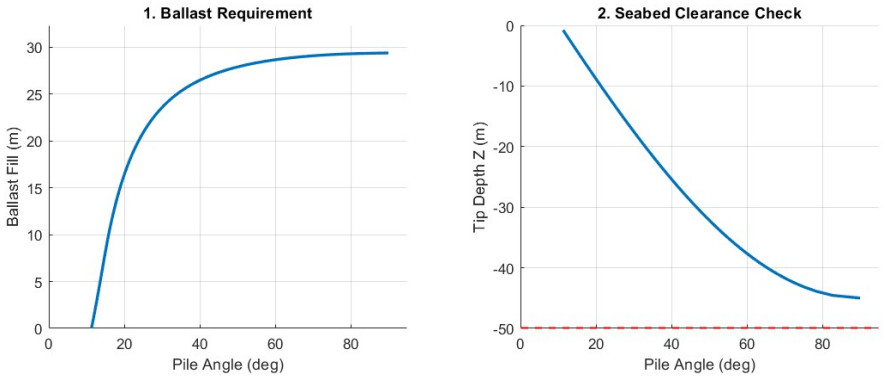

Figure 4.4: Ballast requirement and seabed clearance check evaluated against the pile angle for a pivot offset of 10 m and a pivot height of 10 m.

Figure 4.5 shows how the vertical forces develop with the angle. You can see that quite a substantial magnitude of buoyancy force is generated by adding the ballast weight.

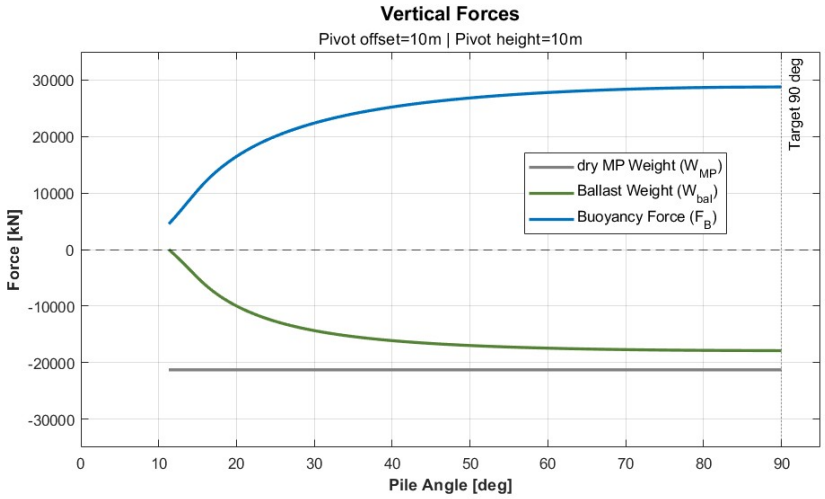

Figure 4.5: Vertical forces (dry monopile weight, ballast weight, and buoyancy) as a function of the pile angle for a pivot offset of 10 m and a pivot height of 10 m.

The resulting moment forces can be seen in Figure 4.6. What is interesting to notice is that the system is unable to apply a turning moment when it approaches 90 degrees. Which means that the system can only reach 90 degrees in a perfect world where no other external forces are acting on the system at 90 degrees.

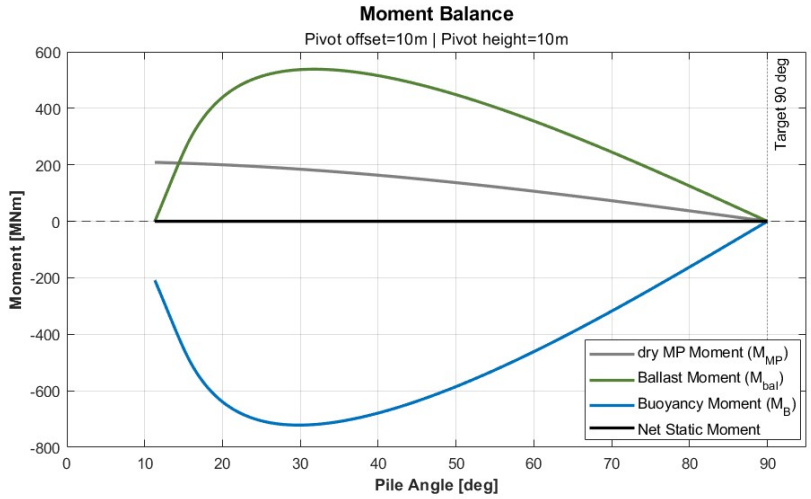

Figure 4.6: Moment balance during the upending sequence, illustrating the individual contributing moments and the net static moment.

The average configuration returns the gripper reaction forces shown in Figure 4.7. It can clearly be seen that over the upending motion, at first, most force is supported with the gripper frame (R_x). As the system approaches 90 degrees, it can be seen that the full system is solely supported by the required frictional force (R_z).

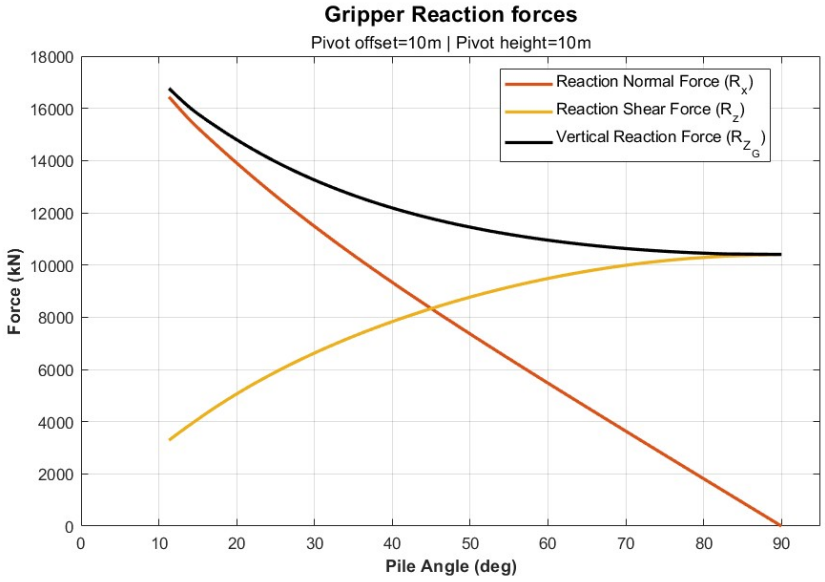

Figure 4.7: Gripper reaction forces (normal, shear, and vertical) evaluated against the pile angle.

4.3. Design Space Exploration

This section investigates how the global geometric parameters, the pivot height ($Z_{G,P}$) and the pivot offset (z_{off}), govern the upending behaviour of the system. A structured sensitivity analysis is first performed to quantify the influence of each parameter on the ballast requirement, seabed clearance, and resulting gripper reaction forces. The pivot height is evaluated while keeping the pivot offset constant, after which the roles are reversed to isolate the effect of the pivot offset. Building on these insights, a combined optimization of both parameters is conducted to identify a feasible configuration that minimizes the structural demand on the gripper while satisfying operational constraints.

4.3.1. Sensitivity to Pivot Height ($Z_{G,P}$)

The pivot height $Z_{G,P}$ can be chosen between 0 m and 20 m, as indicated in Figure 4.8. To isolate the influence of the global pivot height on the upending dynamics, a parametric sweep is performed where the pivot offset is kept constant at $z_{off} = 10$ m, while the global pivot height $Z_{G,P}$ is varied across three discrete levels: 5 m, 10 m, and 15 m. The resulting system responses: ballast requirement, seabed clearance, and local reaction forces are presented in Figure 4.9.

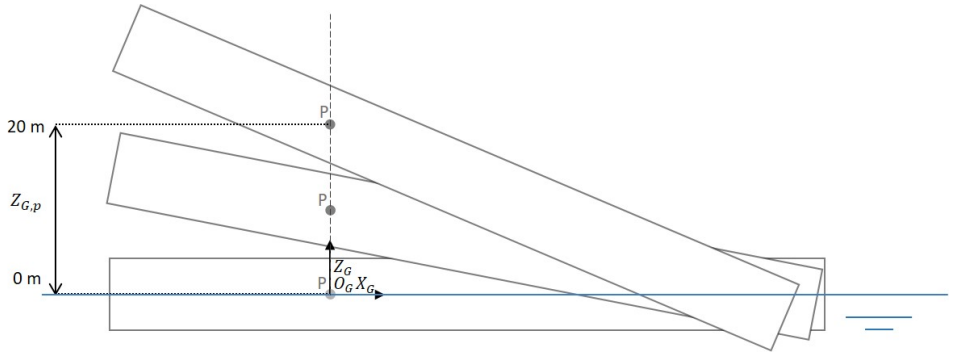

Figure 4.8: The lower and upper bound of the pivot height visualised.

The numerical results reveal a trade-off driven by the pivot height ($Z_{G,P}$), which governs the vertical positioning of the monopile relative to the water surface and the seabed.

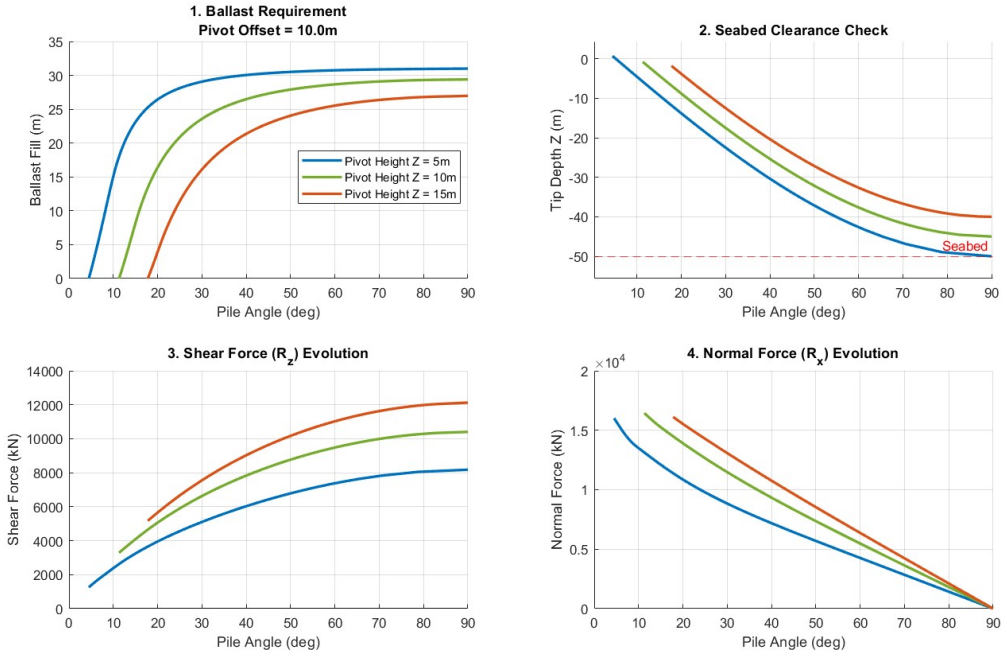

Figure 4.9: Sensitivity analysis of the global pivot height ($Z_{G,P}$) with a fixed offset of $z_{off} = 10$ m, illustrating the trade-off between seabed clearance and structural shear demand.

The Geometric Constraint: Seabed Clearance

The main advantage of increasing the pivot height is geometric safety. Because the gripper acts as a fixed vertical point during quasi-static rotation, a lower pivot height forces the lower half of the monopile deeper into the water column. As observed in the seabed clearance plot (Figure 4.9, top right), for a pivot height of $Z_{G,P} = 5$ m, the monopile tip dangerously approaches the -50 m seabed limit as the angle approaches $90°$. By moving the gripper higher up to $Z_{G,P} = 15$ m, a very comfortable safety buffer of around 10 m above the seabed at verticality is established.

The Structural Penalty: Friction Demand

However, this geometric safety comes at a severe structural cost, as illustrated by the evolution of the local shear force R_z (Figure 4.9, bottom left). The shear force represents the axial load that the gripper must generate purely through friction. At a pivot height of 5 m, the peak shear force at $90°$ is approximately $8,000$ kN. When the pivot is raised to 15 m, this peak load increases to nearly $12,000$ kN.

The physics governing this penalty can be found in the hydrostatic equilibrium. Elevating the pivot height pulls a larger volume of the monopile out of the water, which significantly reduces the total submerged volume V_{sub}. According to the vertical equilibrium equation (Equation 4.5), a reduction in the opposing buoyancy force (F_B) means that a greater percentage of the combined monopile and ballast weight must be mechanically supported by the gripper interface.

Ballast and Normal Force Evolution

The ballast requirement plot (Figure 4.9, top left) further highlights the dual role of the hydrostatic forces. Because the buoyancy force generates the restoring moment that opposes the upending rotation, a higher pivot height, which elevates the monopile and reduces the submerged volume, results in a weaker restoring moment. as a result, significantly less internal ballast is required to drive the system to a given equilibrium angle. Furthermore, the normal force evolution (R_x) demonstrates a convergence: regardless of the chosen pivot height, the transverse structural demand on the gripper arms drops precisely to zero as the monopile reaches $90°$, the gripper must rely entirely on its frictional shear capacity (R_z) to prevent the monopile from slipping.

4.3.2. Sensitivity to Pivot Offset (z_{off})

The pivot offset (z_{off}) can be chosen between 0 m and 20 m, as indicated in Figure 4.10.

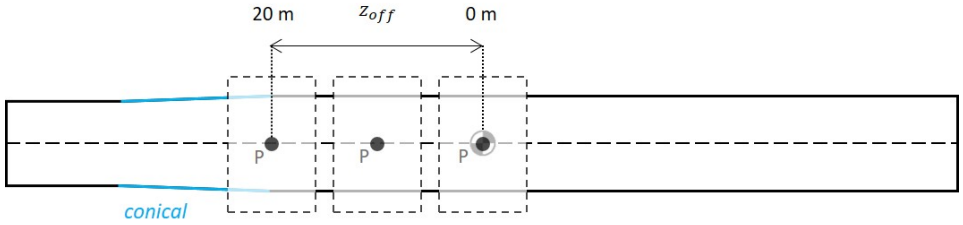

Figure 4.10: The lower and upper bound of the pivot offset visualized. The lower bound is limited by the CoG of the dry MP and the upper bound is limited by the conical section.

To evaluate the influence of the local pivot offset on the upending mechanics, a parametric analysis is performed. The global pivot height is fixed at $Z_{G,P} = 10$ m, while the pivot offset z_{off} is evaluated at 5 m, 10 m, and 15 m. The resulting system responses are presented in Figure 4.11.

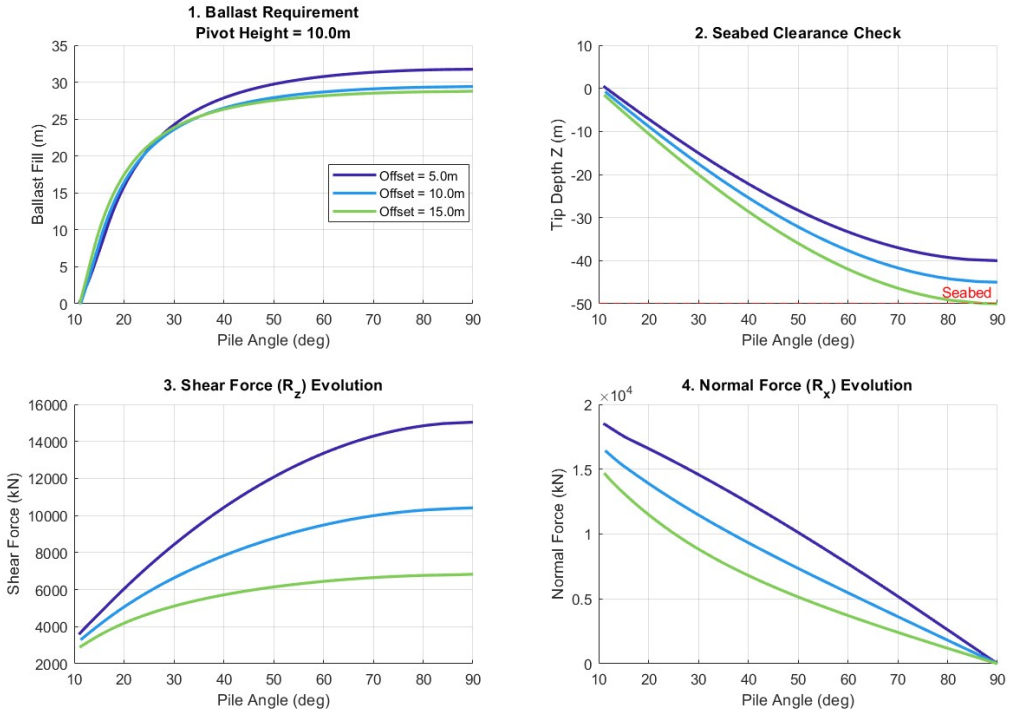

Figure 4.11: Sensitivity analysis of the pivot offset (z_{off}) with a fixed global height of $Z_{G,P} = 10$ m, illustrating an operational trade-off that is the exact inverse of the height sensitivity.

Increasing the pivot offset provides massive structural relief to the gripper. Because a larger offset forces the a larger part of the lower section of the monopile into the water, the submerged volume, and thus the opposing buoyancy force (F_B), increases significantly. As established previously, this increased buoyancy drastically reduces the required friction demand (R_z). As seen in Figure 4.11 (bottom left), moving from an offset of 5 m to 15 m more than halves the peak shear load, dropping it from over $15,000$ kN to approximately $6,800$ kN. However, the reduction in structural forces at the pivot point is linked to a deeper final draft, increasing the risk of seabed collision.

Ultimately, these two isolated sensitivity studies expose the fundamental design conflict of the craneless upending concept: increasing the pivot height saves the system from seabed collision but overloads the gripper, while increasing the pivot offset relieves the loads on the gripper but increases the risk of seabed collision.

4.4. Optimization of Gripper Positioning

To determine the optimal placement of the friction-based gripper, a two-dimensional parametric grid search is conducted across the feasible design space, this grid is visualised in Figure 4.12. The objective is to minimize the peak required shear force (R_z) during the quasi-static upending sequence.

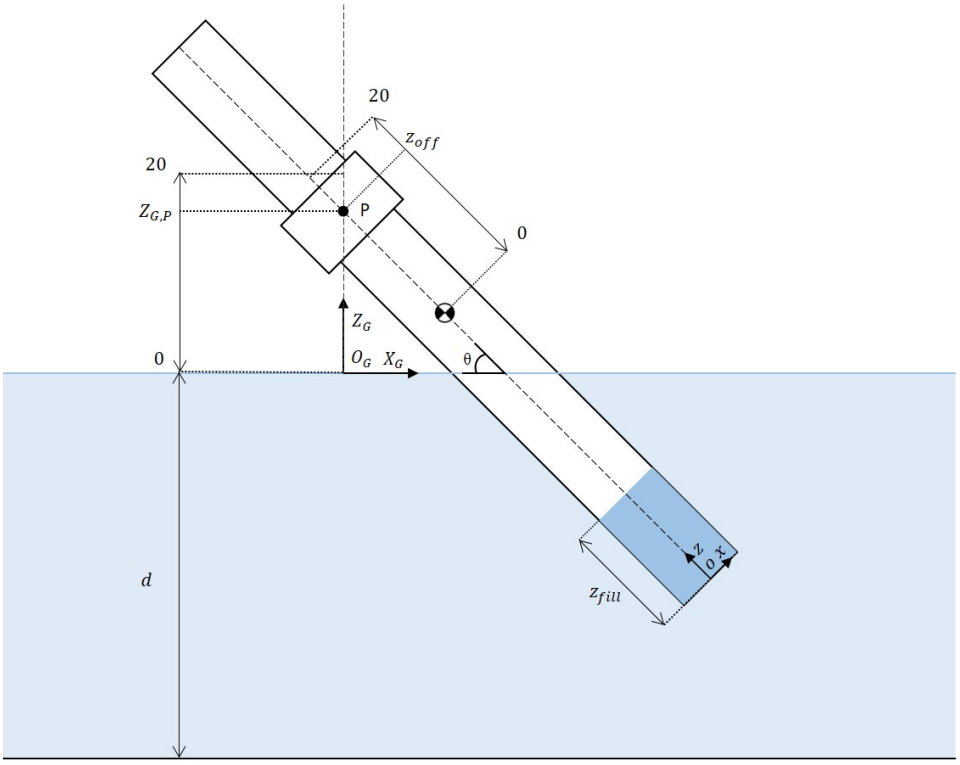

Figure 4.12: The physical representation of the domain over which the optimization takes place.

Objective Function

The objective is to minimize the maximum absolute shear force experienced by the gripper throughout the entire ballast-driven upending rotation. Minimizing this force directly reduces the required frictional holding capacity, thereby lowering the risk of slip and local shell buckling.

$$\min_{z_{G,P}, z_{off}} \left(\max_{\theta \in [0, 90^\circ]} |R_z(\theta)| \right) \tag{4.11}$$

Control Variables (Design Space)

The parametric sweep evaluates the two geometric variables:

- **Pivot Height ($Z_{G,P}$):** The global vertical coordinate of the passive hinge connecting the gripper to the jack-up vessel. Evaluated between 0 m and 20 m.
- **Gripper Offset (z_{off}):** The longitudinal distance from the monopile's dry center of gravity to the gripping pivot point. Evaluated between 0 m and 20 m (representing a physical grip location 45 m to 65 m from the pile tip, ensuring the gripper remains safely below the conical section).

Operational Constraints

To ensure the evaluated configurations are physically viable and safe in an offshore environment, the design space is bounded by three constraints:

1. **Seabed Clearance:** The lowest point of the monopile tip must maintain a minimum safe distance of 3 m from the seabed at all times during the rotation to prevent collision.

$$Z_{tip}(\theta) \geq Z_{seabed} + 3 \text{ m} \tag{4.12}$$

2. **Kinematic Feasibility (Upending Completion):** The chosen configuration must be capable of achieving a fully vertical orientation ($90°$). Configurations that achieve hydrostatic equilibrium at an angle less than $90°$, despite reaching maximum allowable ballast, are deemed infeasible.
3. **Ballast Mass Limitation:** The internal ballast water level is capped at the longitudinal location of the pivot point (z_p). Any ballast added above the pivot creates a negative moment arm relative to the hinge, which actively resists the upending rotation and unnecessarily increases the total system mass and resultant shear loads.

The resulting design space and the maximum absolute shear forces for all evaluated configurations are mapped in Figure 4.13.

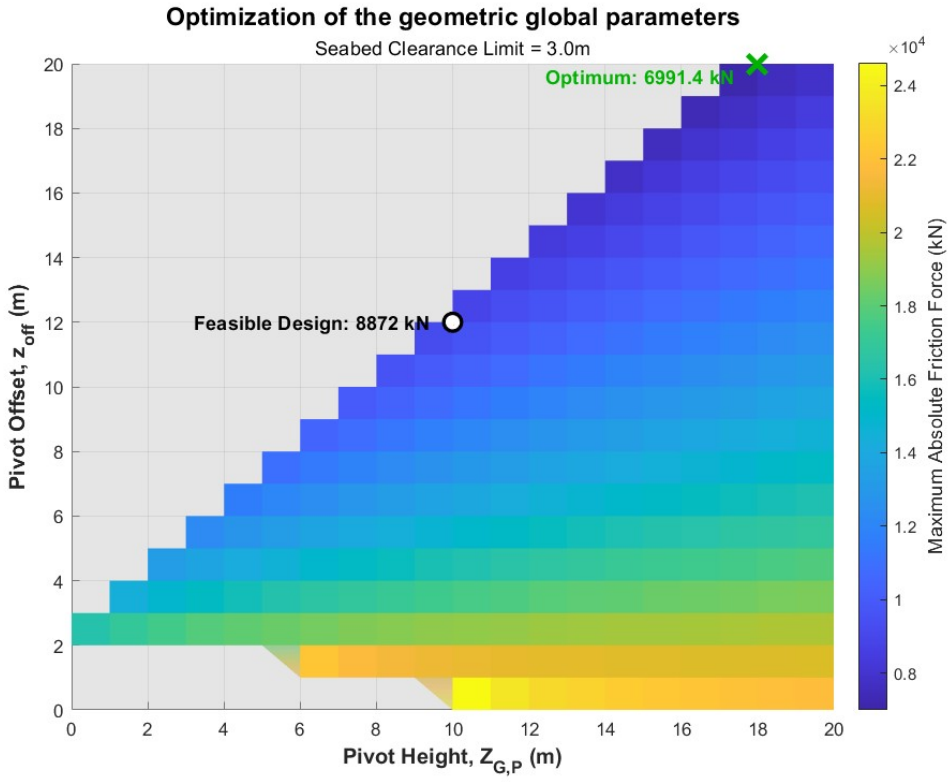

Figure 4.13: Design space exploration mapping the maximum absolute shear force (R_z) as a function of pivot height and offset.

The contour map visually synthesizes the governing physics of the upending operation. The gray region in the upper-left quadrant represents the geometric limit of the system, where high offsets combined with low pivot heights result in seabed collisions. The gray area at the bottom represents configurations that are unable to reach $90°$ while adhering to the ballast mass and geometrical restrictions. Conversely, the color gradient demonstrates that the structural friction demand decreases continuously as the configuration moves toward the upper-right quadrant (higher offsets and higher pivot heights).

The Theoretical Optimum

The optimization algorithm identifies a theoretical minimum shear force of $6,991.4$ kN. Notably, this mathematical optimum sits exactly on the boundary of the geometric constraint line. This placement confirms the underlying hydrostatic logic: to minimize the downward load on the gripper, the system must maximize the opposing buoyancy force. Maximizing buoyancy requires submerging the monopile as deeply as possible. Therefore, the absolute safest point for the gripper structure is achieved by pushing the offset and pivot height to their maximum values.

Feasible Design Point & Practical Compromise

While the global model identifies this theoretical optimum at the edges of the evaluated domain, translating these kinematics into physical components requires engineering compromise. For the physical

gripper to operate effectively, its structural frame must remain largely symmetric, and the physical dimensions of the gripping arms limit how far along the monopile the pivot can realistically be placed. Because moving the symmetrical pivot design closer to the theoretical optimum would result in crossing the conical section.

Consequently, the theoretical optimum is technically infeasible for physical implementation. Considering both the geometric realities of the gripper design, a feasible design point is selected near $Z_{G,P} = 10$ m and $z_{off} = 12$ m. As indicated by the contour map, stepping away from the theoretical optimum into this feasible design space results in a structural penalty, increasing the peak shear demand to approximately $9,000$ kN.

These ultimate values of $Z_{G,P} = 10$ m and $z_{off} = 12$ m establish the definitive geometric configuration for the remainder of the analysis. This configuration will be used in the dynamic simulation, which will verify the system's stability, operational duration, and response to environmental wave forces.

4.5. Dynamic Time-Domain Simulation

While the quasi-static model successfully mapped the geometric limits of the upending operation, it fundamentally assumes a sequence of perfectly balanced equilibrium states. In reality, the upending is a continuous operation governed by active kinematic boundary conditions: a constant jacking velocity (v_j) bringing the pivot point upwards, and a constant pump rate (Q) injecting ballast. Furthermore, the system is subjected to the hydrodynamic loads of the offshore environment.

To evaluate the influence of wave loads, the stability, the true peak structural demands, and the total duration of the operation, a 1-Degree-of-Freedom (DoF) dynamic time-domain model is developed. Because the local translation of the monopile is fixed by the rigid gripper arms and the friction interface, the system exhibits only one degree of freedom: the pitch rotation (θ).

Figure 4.14 provides a clear overview of the system variables and their orientation with respect to the local and global coordinate frames. The control variables of the system are the jacking velocity (v_j), indicated by the vertical black arrow, and the pump rate (Q), indicated by the blue arrow. Because the model now maps a dynamic sequence, the geometric parameters are time (t) and/or angle (θ) dependent.

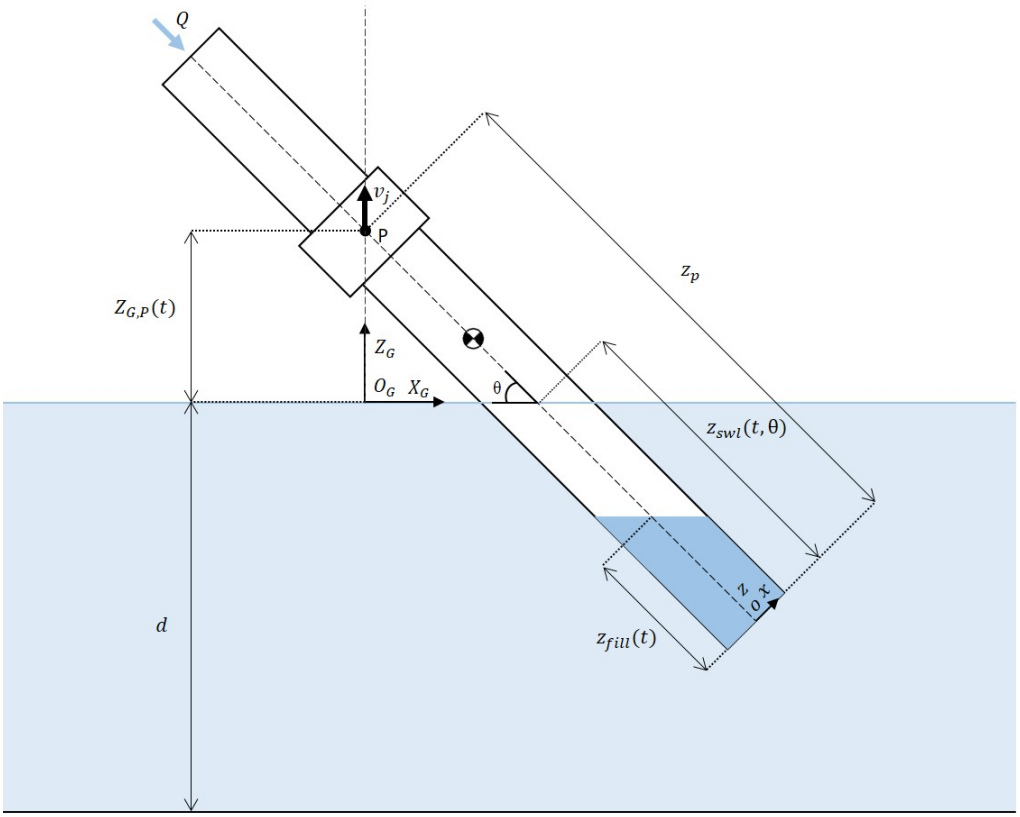

Figure 4.14: Schematic of the dynamic simulation, the active control variables (Q, v_j), and the time/angle-dependent boundaries.

4.5.1. Dynamic System Description & Kinematic Constraints

The dynamic geometric parameters, driven by the control variables, are defined in Table 4.2. The control variables applied to the simulation are listed in Table 4.3.

Table 4.2: Operational inputs and kinematic constraints.

Parameter	Symbol	Equation
Global Pivot Height	$Z_{G,P}(t)$	$v_j \cdot t + Z_{G,P,0}$
Ballast Fill Level	$z_{fill}(t)$	$\frac{Q}{A_i} \cdot t + z_{fill,0}$
Ballast Fill Velocity	$\dot{z}_{fill}$	Q/A_i
Local Waterline Intersection	$z_{swl}(t,\theta)$	$z_p - \frac{Z_{G,P}(t)}{\sin(\theta)}$
Waterline Velocity	$\dot{z}_{swl}(t,\theta)$	$-\frac{v_j}{\sin(\theta)} + \frac{Z_{G,P}(t)\cos(\theta)}{\sin^2(\theta)}\dot{\theta}$

Table 4.3: System parameters for the dynamic simulation.

Parameter	Symbol	Value	Unit
Jacking Speed	v_j	0.25	m/min
Max Pump Rate	Q	3400	m^3/h

The positional state of the system is actively driven by the operational inputs (Table 4.2). The global pivot height ($Z_{G,P}$) moves continuously according to the jacking speed (v_j), initiating from its starting elevation ($Z_{G,P,0}$).

The parameter $z_{fill}(t)$ represents the equivalent volumetric fill level, rising as a direct function of the pump rate (Q) filling the internal cross-sectional area (A_i). It is critical to note that while $z_{fill}(t)$ dictates the total volume of the injected water, the dynamic model treats this fluid as a quasi-static liquid. Because the monopile pitches continuously, the water pools horizontally, creating a Free Surface Effect (FSE) fluid wedge rather than a solid cylindrical plug (as illustrated in Figure 4.14). Consequently, while $z_{fill}(t)$ mathematically governs the volumetric mass input, the true geometric distribution, influencing the moment arm, of this mass is dynamically resolved at every time step (Appendix B.2).

Because the dynamic Equation of Motion relies on the precise rate of change of the system's mass, the boundary velocities of these parameters are critical. The internal fluid rise velocity ($\dot{z}_{fill}$) is a constant derived directly from the pump rate. Conversely, the term $\dot{z}_{swl}$ represents the velocity at which the external waterline travels along the longitudinal axis of the monopile. This velocity is a coupled function of both the continuous vertical jacking translation and the angular rotation. Applying the chain rule yields:

$$\dot{z}_{swl}(t,\theta) = \frac{\partial z_{swl}}{\partial Z_{G,P}}\frac{dZ_{G,P}}{dt} + \frac{\partial z_{swl}}{\partial \theta}\frac{d\theta}{dt} = -\frac{v_j}{\sin(\theta)} + \frac{Z_{G,P}(t)\cos(\theta)}{\sin^2(\theta)}\dot{\theta} \tag{4.13}$$

These kinematic constraints govern the time-varying integration limits required to solve the hydrodynamic loads and the shifting system inertia.

4.6. The Equation of Motion

The dynamic behavior of the system is governed by Newton's Second Law for rotational motion about the fixed pivot point (P). Because the mass of the system changes over time due to the injected water ballast, the rate of change of momentum must account for both angular acceleration and mass variation. By incorporating the hydrostatic buoyancy moment (M_B), the gravitational moments of the steel (M_{mp}) and ballast (M_{bal}) and the hydrodynamic wave loads, the complete, non-linear Equation of Motion for the monopile upending sequence is established as:

$$I_P(t,\theta)\ddot{\theta} + \dot{I}_P(t,\theta)\dot{\theta} + M_B(t,\theta) - M_{mp}(\theta) - M_{bal}(t,\theta) = M_{drag}(t,\theta,\dot{\theta}) + M_{wave,I}(t,\theta) \tag{4.14}$$

This second-order differential equation is decomposed into a system of first-order equations and solved iteratively in the time domain to yield the system's angular trajectory (θ) and velocity ($\dot{\theta}$). A visual representation of the dynamic equilibrium, mapping all driving, restoring, and inertial components of the Equation of Motion, is provided in Figure 4.15. Notably, the internal ballast is described as a pooling horizontal fluid wedge, representing the Free Surface Effect (FSE).

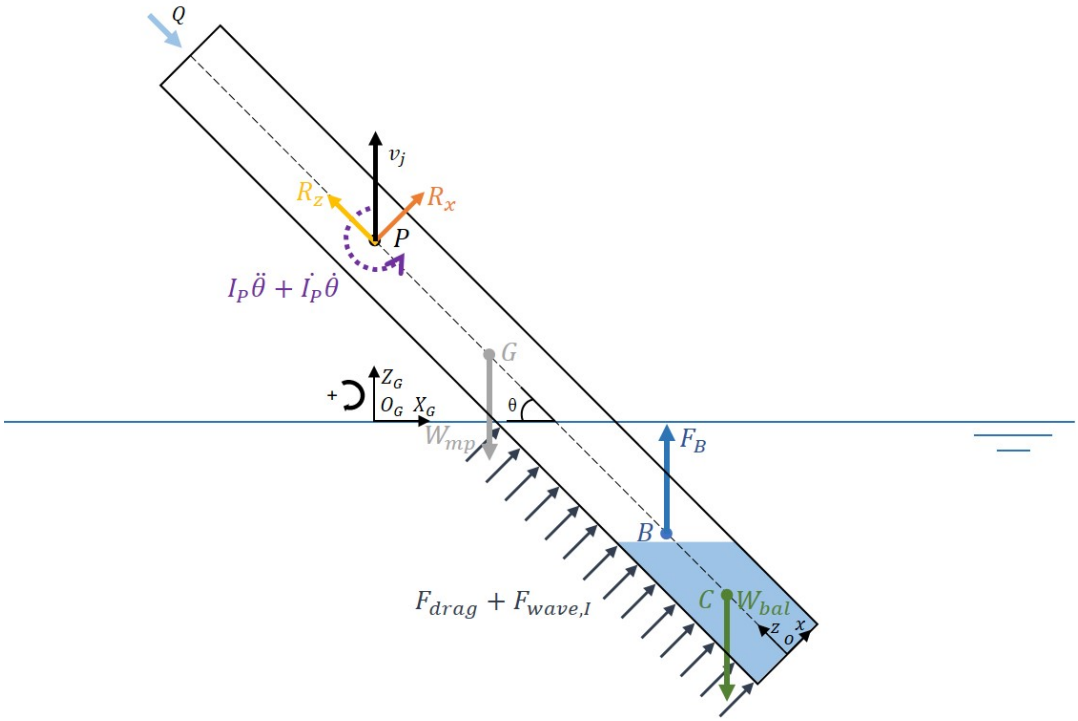

Figure 4.15: Dynamic Free Body Diagram applying, illustrating all forces, moments, and the inertial resistance governing the Equation of Motion.

The individual components driving this equation are defined in the following subsections.

4.6.1. Time-Varying System Inertia (I_P & $\dot{I}_P$)

The total mass moment of inertia (I_P) around the global pivot point (P) represents the system's resistance to angular acceleration. The total inertia consists of three distinct mass components: the dry monopile steel ($I_{mp,P}$), the internal ballast water ($I_{bal,P}$), and the hydrodynamic added mass ($I_{a,P}$):

$$I_P(t,\theta) = I_{mp,P} + I_{bal,P}(t) + I_{a,P}(t,\theta) \tag{4.15}$$

Based on the Parallel Axis Theorem, the total inertia of any discretized strip consists of its local cross-sectional inertia about its own centroid (I_{local}) plus the parallel axis translation ($m \cdot r^2$). For a hollow cylinder, the local inertia is defined as $I_{local} = \frac{1}{4}m(R_o^2 + R_i^2)$.

However, for a monopile with a high aspect ratio ($L/D \approx 10$), the local contribution is negligible compared to the magnitude of the parallel axis term. a scale analysis shows that at a distance of $r = 20$ m from the pivot, the ratio of local to parallel inertia is:

$$\frac{I_{local}}{I_{parallel}} \approx \frac{\frac{1}{4}(4.5^2 + 4.4^2)}{20^2} \approx 2.4\% \tag{4.16}$$

As the distance r increases toward the pile boundaries ($r \approx 45$ m), this contribution drops below 0.5%. Consequently, the local cross-sectional inertia is omitted from the analytical model. The general formula for the system inertia is therefore defined entirely by the integral of the parallel axis translation:

$$I = \int r^2 \, dm \tag{4.17}$$

where dm is an infinitesimal element of mass and r is the perpendicular distance from the axis of rotation (at the pivot point P) to the mass element. For the local coordinate system of the monopile, this distance is universally defined for all distances as $r = (z - z_p)$. The elemental mass dm is defined as $dm = (\rho \cdot A)dz$.

1. Monopile Dry Mass Inertia ($I_{mp,P}$)
The mass element of the steel pile depends on the steel density (ρ_s) and the cross-sectional area of the hollow cylinder wall, $A_{mp} = \pi((D_o/2)^2 - (D_o/2 - t_{mp})^2)$. Integrating over the full, constant length L yields:

$$I_{mp,P} = \int_0^L \rho_s A_{mp}(z - z_p)^2 \, dz \tag{4.18}$$

2. Ballast Water Mass Inertia ($I_{bal,P}$)
Because the internal ballast is modeled as a quasi-static liquid (FSE), it forms a complex fluid wedge rather than a simple cylindrical plug. Consequently, its rotational inertia is evaluated as the discrete summation of the fluid mass acting across N longitudinal strips.

$$I_{bal,P}(t, \theta) = \sum_{i=1}^{N} \left(dm_i \cdot (z_p - z_i)^2 \right) \tag{4.19}$$

Where the elemental fluid mass is defined as $dm_i = \rho_w \cdot A_{bal,i}(t, \theta) \cdot dz$. The local cross-sectional fluid area ($A_{bal,i}$) approaches the wedge area of FSE as the system pitches. The full 1D strip-theory derivation of this fluid area, governed by the equivalent volumetric fill parameter $z_{fill}(t)$, is detailed in Appendix B.2.

3. Added Mass Inertia ($I_{a,P}$)
The virtual added mass element is derived from the seawater density and the total displaced volume of the outer cross-section (A_o), scaled by the dimensionless added mass coefficient (C_a). According to DNV-RP-N103 (Figure 4.16), the added mass coefficient for a cylinder moving perpendicular to its axis depends on the length-to-diameter ratio ($b/2a = 90/9 = 10$). Consequently, the coefficient is taken as $C_a = 1.0$. the added mass inertia formula is as follows:

$$I_{a,P}(t, \theta) = \int_0^{z_{swl}(t,\theta)} C_a \rho_w A_o (z - z_p)^2 \, dz \tag{4.20}$$

The upper integration limit is the local waterline $z_{swl}(t, \theta)$, which dynamically shifts along the monopile based on the current pitch angle and the global jacking height: $z_{swl}(t, \theta) = z_p - Z_{G,P}(t)/\sin(\theta)$.

			b/2a	C_A	
Right circular cylinder	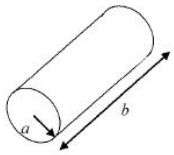	Vertical	1.2 2.5 5.0 9.0 ∞	0.62 0.78 0.90 0.96 1.00	$\pi a^2 b$

Figure 4.16: Added mass coefficient (C_a) for a 3D cylinder as defined in appendix A of DNV-RP-N103 [75].

.

4.6.2. Rate of Change of Inertia ($\dot{I}_P$)

To accurately solve the equation of motion, the dynamic model must account for the rate at which mass crosses the system boundaries during the upending sequence. The total rate of change of inertia is the sum of the changes in the external added mass and the internal ballast:

$$\dot{I}_P(t,\theta) = \dot{I}a, P(t,\theta) + \dot{I}_{bal,boundary}(t,\theta) \tag{4.21}$$

Because the external added mass is modeled as a uniform cylinder with a time-varying boundary (z_{swl}), its derivative is calculated using the 1D application of a deforming control volume, known as the Leibniz Integral Rule. Applying this rule to Equation 4.20 yields the explicit rate of change for the added mass:

$$\dot{I}_{a,P}(t,\theta) = \left[C_a \rho_w A_o (z_{swl}(t,\theta) - z_p)^2 \cdot \dot{z}_{swl}(t,\theta)\right] \tag{4.22}$$

The internal water ballast is injected across a continuously deforming elliptical free surface. To accurately capture the rate of change of the ballast inertia, the Reynolds Transport Theorem (RTT) [78] is applied. The rate at which inertia is injected into the system is the constant mass flow rate ($\rho_w \cdot Q$) multiplied by the square of the distance from the pivot to the exact geometric centroid of this elliptical waterplane (z_{surf}):

$$\dot{I}_{bal,boundary}(t,\theta) = (\rho_w \cdot Q) \cdot (z_p - z_{surf})^2 \tag{4.23}$$

The precise calculation of this area-weighted longitudinal boundary (z_{surf}) is provided in Appendix B.2. By adding this term into the Equation of Motion, the dynamic solver accurately describes the influence of the added mass of the system.

4.6.3. Hydrostatic & Gravitational Moments (M_B, M_{mp}, & M_{bal})

While the fundamental physics of the hydrostatic and gravitational loads are established in the quasi-static analysis (Section 4.1), they are implemented in the dynamic model as time-varying functions of the system state (θ, t).

The total gravitational driving moment and hydrostatic restoring moment are separated into three parts: the steel monopile, the internal ballast, and the external buoyancy.

1. Monopile Gravity Moment (M_{mp})

The driving moment generated by the dry steel weight (W_{mp}) is purely a function of the pitch angle, acting through the pile's geometric center:

$$M_{mp}(\theta) = W_{mp}\left(z_p - \frac{L}{2}\right)\cos(\theta) \tag{4.24}$$

2. Ballast Gravity Moment (M_{bal})
When the internal water is allowed to form a free surface, it naturally pools on the ”downhill” side of the pitched pipe. Consequently, the center of mass of any partially filled cross-section shifts transversely away from the longitudinal centerline by a magnitude of $x_{C,i}$, as defined in Appendix B.2. This transverse shift has a global horizontal projection equal to $x_{C,i}\sin(\theta)$.

To determine the true driving moment, the global horizontal distance (X_{G,C_i}) between the pivot point (P) and the fluid centroid of any strip is updated to include both the axial and transverse contributions:

$$X_{G,C_i} = (z_p - z_i)\cos(\theta) + x_{C,i}\sin(\theta) \tag{4.25}$$

Because the fluid pools ”downward” toward the vertical axis passing through P, this transverse shift physically decreases the total horizontal moment arm. The updated driving moment for the entire free surface ballast volume is the sum of the contributions from all N strips:

$$M_{bal}(t,\theta) = \sum_{i=1}^{N}(dm_i \cdot g \cdot X_{G,C_i}) \tag{4.26}$$

3. Buoyancy Moment (M_B)
The restoring moment (M_B) is provided by the upward buoyancy force. To capture the non-linearities of the circular cross-section during rotation, the model utilizes the numerical summation derived from Strip Theory (Appendix B.1). The moment magnitude is evaluated as the discrete sum of the buoyant forces acting on all N submerged strips:

$$M_B(t,\theta) = \sum_{i=1}^{N}\left(dF_{b,i}(t,\theta)\cdot(z_p - z_i)\cos(\theta)\right) \tag{4.27}$$

Where the elemental buoyant force $dF_{b,i}$ is defined by the fluid density and the dynamically calculated submerged area of the local cross-section:

$$dF_{b,i}(t,\theta) = \rho_w \cdot g \cdot A_{sub,i}(t,\theta)\cdot dz \tag{4.28}$$

In this dynamic formulation, the submerged force of each strip $dF_{b,i}$ is recalculated at every time step. This is necessary because the global vertical position of each strip center, and thus its immersion depth, varies not only with the pitch angle θ but also with the continuous vertical translation of the pivot $Z_{G,P}(t)$.

4.6.4. Relative Velocity Drag (M_{drag})

To accurately capture the non-linear interaction between the moving wave particles and the rotating structure, the relative velocity formulation of the Morison equation is implemented. The local velocity of any given pile segment located at a distance $(z - z_p)$ from the pivot is defined as $v_{mp} = (z - z_p)\dot{\theta}$. Therefore, the relative normal velocity between the fluid and the pile is:

$$v_{rel}(z,t,\theta) = u_n(z,t,\theta) - (z - z_p)\dot{\theta} \tag{4.29}$$

By defining the drag force based on v_{rel}, the mathematical model couples wave excitation and hydrodynamic damping into a single integral. If the water is entirely still ($u_n = 0$), the equation naturally reduces to pure hydrodynamic damping. The total hydrodynamic drag moment, as defined in DNV-RP-C205 [73], is integrated over the submerged length of the pile up to the dynamic intersection with the still water line (z_{swl}):

$$M_{drag}(t,\theta,\dot{\theta}) = \int_0^{z_{swl}(t,\theta)} \frac{1}{2}\rho_w D_o C_{DS}|v_{rel}|v_{rel}\cdot(z - z_p)\,dz \tag{4.30}$$

Where C_{DS} is defined by standard DNV-RP-N103 [75] (Figure 4.17). The aspect ratio of the monopile is defined as $L/D = 90/9 = 10$. According to Figure 4.17 for an aspect ratio of 10 in subcritical flow, the 3D-corrected member drag coefficient is determined to be $C_{DS} = 0.68$.

Geometry	Dimensions	C_{DS}	
Circular cylinder normal to flow. 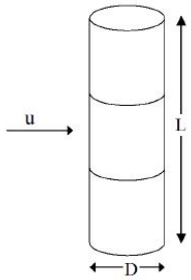	L/D	Sub critical flow $R_e < 10^5$	Supercritical flow $R_e > 5{\cdot}10^5$
		κ	κ
	2	0.58	0.80
	5	0.62	0.80
	10	0.68	0.82
	20	0.74	0.90
	40	0.82	0.98
	50	0.87	0.99
	100	0.98	1.00
	$C_{DS} = \kappa C_{DS}^{\infty}$ κ is the reduction factor due to finite length. C_{DS}^{∞} is the 2D steady drag coefficient.		

Figure 4.17: Drag coefficient (C_{DS}) for a cylinder as defined in appendix B of DNV-RP-N103 [75].

4.6.5. Wave Inertia Moment ($M_{wave,I}$)

In addition to the viscous drag, the accelerating wave particles exert a Froude-Krylov force and a diffraction force on the structure. This is driven by the normal fluid acceleration ($\dot{u}_n$) and is scaled by the inertia coefficient ($C_M = 1 + C_A$) [73]:

$$M_{wave,I}(t,\theta) = \int_0^{z_{swl}(t,\theta)} \rho_w A_o C_M \dot{u}_n \cdot (z - z_p)\, dz \tag{4.31}$$

4.6.6. Model Verification and the Impact of Fluid Dynamics

The dynamic time-domain solver incorporates complex, time-varying boundary conditions and non-linear numerical integration via MATLAB's `ode45` solver. Before utilizing this model to assess environmental wave impacts, the model was verified (Appendix C) with the quasi-static model (Section 4.2).

To isolate the underlying mass and hydrostatic physics, a baseline dynamic simulation was conducted without external wave excitation ($H_s = 0$ m), using a simplified "frozen" ballast mass to match the static assumptions. The dynamic shear force converged to the established static envelope as the pile reached verticality, confirming that the shifting integration boundaries and coordinate transformations in the ODE solver are structurally sound. The full methodology and verification of this baseline model are detailed in Appendix C.

The Structural Penalty of the Free Surface Effect (FSE)

With the ODE solver verified, the Free Surface Effect (FSE) equations derived in Appendix B.2 were used to evaluate the true structural demands of the upending operation. To quantify the impact of the internal fluid dynamics, the waveless FSE model was compared directly against the frozen baseline assumption, as illustrated in Figure 4.18.

The inclusion of the FSE reveals a significant increase in the global reaction forces acting on the gripper system. In the baseline model, the peak local normal force (R_x) reaches approximately $13,300$ kN. However, when the water is allowed to pool horizontally, the peak normal force increases by nearly $1,000$ kN, reaching approximately $14,200$ kN midway through the sequence. Although the gripper structure is assumed to be sufficiently robust for this design phase, and the focus remains on the final shear force, which is identical in both the frozen and FSE simulations, this substantial increase in structural force cannot be ignored.

This load amplification perfectly aligns with the derived FSE kinematics. Because the fluid pools "downward", the effective horizontal moment arm of the liquid counterweight is reduced. With the ballast providing less gravitational driving moment to assist the rotation, The system experiences lower draft and experiences less relief by the buoyancy force.

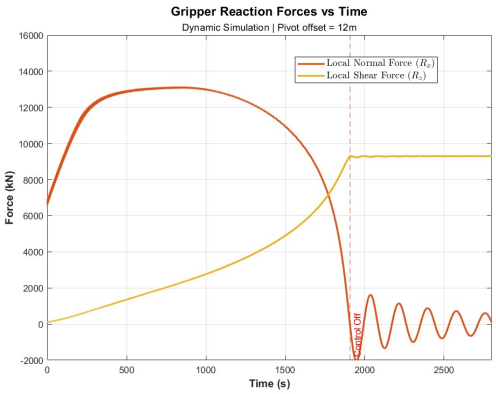

(a) Frozen Ballast model. Peak normal force $R_x \approx 13,300$ kN.

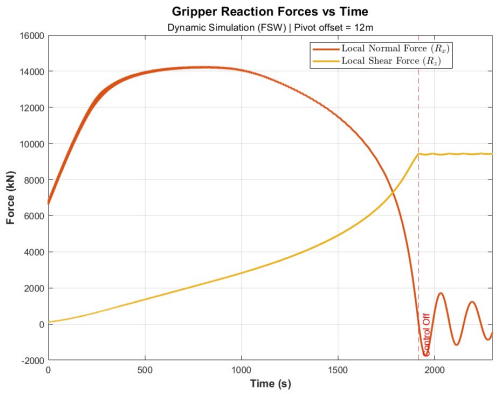

(b) Advanced model (FSE). Peak normal force $R_x \approx 14,200$ kN.

Figure 4.18: Comparison of the gripper reaction forces over time between the baseline and FSE models. The shifting fluid wedge physically increases the required reaction forces on the gripper system.

Consequently, relying on a simplified ”frozen” mass assumption leads to a non-conservative underestimation of the structural loads. The FSE formulation is therefore required to establish a safe, realistic design envelope for the gripper mechanics.

Model Limitations: Fluid Inertia and the Quasi-Static Liquid Assumption

The 1D strip-theory FSE model fundamentally assumes that the internal ballast acts as a quasi-static liquid, meaning the free surface perfectly and instantaneously aligns with the global horizontal plane at every computational time step. In physical reality, the internal fluid possesses inertia and viscosity. As the monopile pitches, these properties cause the fluid to temporarily lag behind the rotation of the structure before settling into its new horizontal equilibrium.

By neglecting this dynamic fluid lag, the model assumes that the water pools transversely to the ”downhill” side of the pipe instantaneously. As established in Equation 4.25, this instantaneous pooling immediately minimizes the effective horizontal moment arm of the ballast, placing the fluid in its lowest-energy state. In reality, the physical lag forces the water to temporarily remain further ”uphill” (closer to the longitudinal centerline). This means the true physical moment arm remains temporarily larger than the model calculates, yielding a marginally higher gravitational driving moment. Consequently, the quasi-static FSE assumption is theoretically pessimistic (conservative), as it slightly overestimates the gripper structural loads.

4.7. Full Dynamic Operational Results

With the physics of the dynamic engine verified and the Free Surface Effect incorporated, the final step is to simulate the true operational environment. The simulation is subjected to the design sea state established in Section 3.4: a significant wave height of $H_s = 2.0$ m, a peak wave period of $T_p = 10$ s, and a steady current velocity of $v_c = 0.5$ m/s. The final global parameters are a pivot height ($Z_{G,P}$) of 10 m, a pivot offset (z_{off}) of 12 m and a ballast fill height (z_{fill}) is 30 m, equivalent to a volume of 1803 m^3. The progression of the control variables ($Z_{G,P}$ and z_{fill}) over the upending sequence can be seen in Figure 4.19

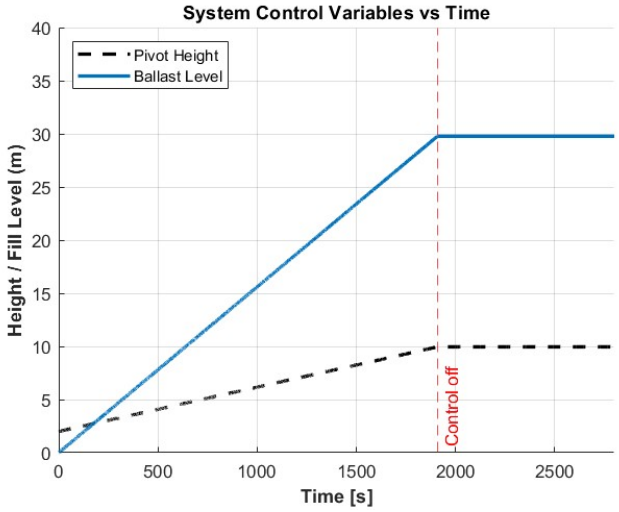

Figure 4.19: Progression of the control variables $Z_{G,P}$ and z_{fill}. At t ≈ 1800, the control is halted, as the final orientation of $90°$ is reached.

4.7.1. Kinematic Response

The kinematic response of the upending procedure is presented in Figure 4.20.

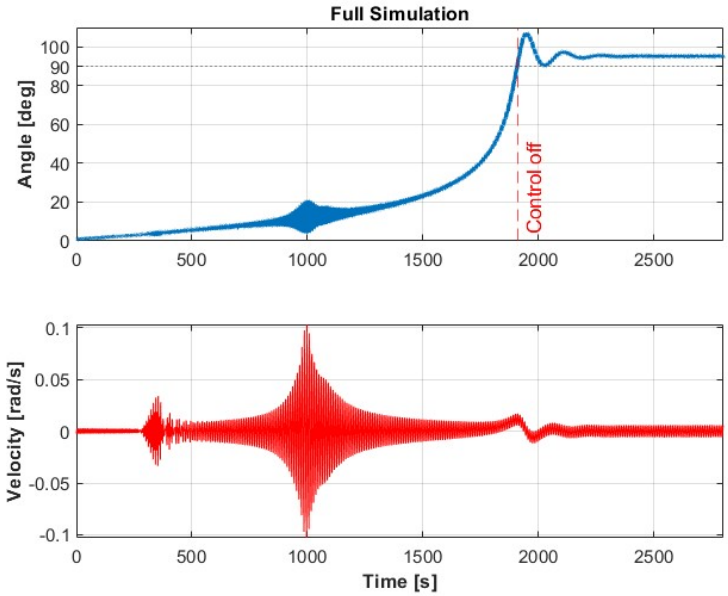

Figure 4.20: Time-domain kinematic response of the fully loaded simulation (FSE, Waves, and Current). Note the dynamic amplification near $t \approx 1{,}000$ s and the final current-induced equilibrium at $95°$.

Two critical dynamic phenomena are observed in the resulting kinematics:

1. **Resonance ($t \approx$ 1,000 s):** As the monopile fills with ballast and changes its pitch angle, its rotational stiffness and inertia continuously shift. At approximately $\theta \approx 10°$, a spike in angular velocity is observed. This indicates a resonance crossing, where the system's shifting natural period temporarily aligns with the 10 s wave excitation.
2. **Current-Induced Equilibrium ($t >$ 2,000 s):** Unlike the waveless baseline which settled perfectly at $90°$, the fully loaded system overshoots and settles into a steady-state equilibrium at approximately $95°$. This is a direct physical consequence of the steady current ($v_c = 0.5$ m/s). At exactly $90°$ (vertical), the centers of gravity and buoyancy align vertically with the pivot, yielding a net hydrostatic restoring moment of zero. Therefore, the system is physically incapable of resisting the overturning drag force of the current at exactly $90°$. The monopile must pitch past vertical to $95°$, shifting its mass transversely to generate the necessary lever arm to counteract the environmental drag.

The kinematic response, shown in Figure 4.20, shows how the angle and angular velocity progress over time. This simulation of the monopile upending is visualised with a storyboard in Figure 4.21.

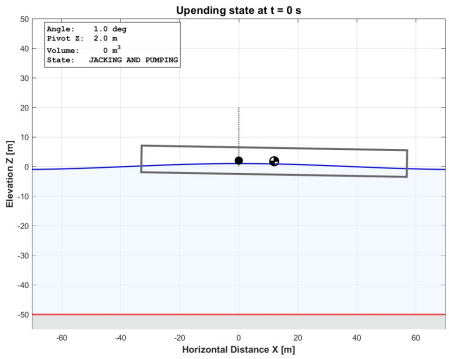

(a) Start of the upending.

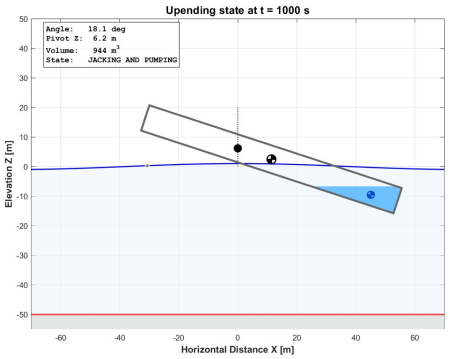

(b) Phase of the upending where wave harmonization takes place.

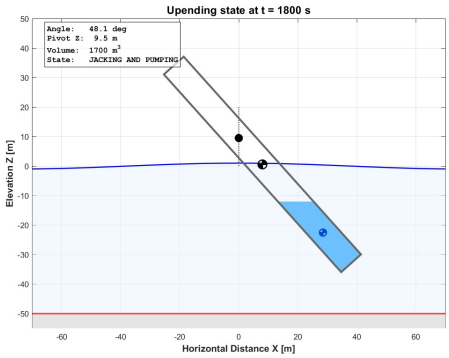

(c) Phase of the upending where the monopile is about to rotate quickly to its final state.

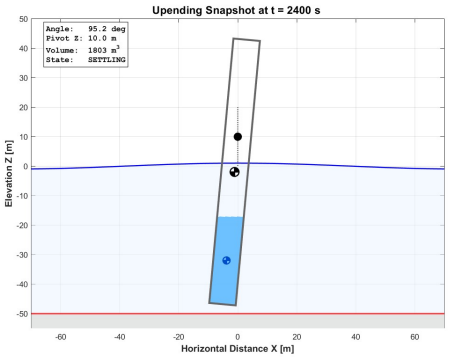

(d) Final state of the monopile at $95.2°$, an equilibrium state a little beyond the $90°$ goal.

Figure 4.21: Storyboard of the upending sequence where four important upending states are visualised.

Dynamic Force Amplification and Buoyancy Loss

The structural consequences of the wave and current excitation are presented in Figure 4.22, which tracks the gripper reaction forces throughout the fully loaded upending sequence.

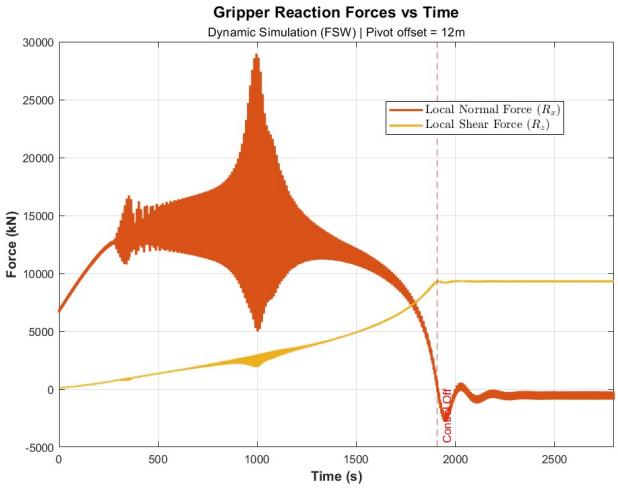

Figure 4.22: Gripper reaction forces over time for the full simulation (FSE, Waves, and Current). A severe load spike occurs during the resonance crossing at $t \approx 1{,}000$ s.

The most critical discovery in the global dynamic analysis occurs during the resonance crossing at $t \approx 1{,}000$ s. At this stage, the local normal force (R_x) experiences severe dynamic amplification, with the load spiking to nearly 30,000 kN (Figure 4.22). This represents an increase of more than 100 % compared to the maximum loads predicted by the waveless baseline model (Figure 4.18).

This massive load amplification is driven by a rapid loss of hydrostatic buoyancy. Because the mechanical pivot is modeled as an ideal hinge with zero rotational friction, it provides no mechanical damping against the wave excitation. Consequently, during the resonance phase, the wave kinematics induce large-amplitude pitch oscillations that repeatedly swing the monopile back toward the free surface.

As the monopile pitches upwards, the total submerged volume of the pile drastically decreases. Hydrostatic buoyancy is the main force relieving the vertical deadweight of the structural steel and ballast water. Therefore, when this submerged volume is lost, the supporting buoyancy vanishes, forcing the gripper to carry the weight of the ballasted system with little buoyancy aid.

Interestingly, while the normal force is highly sensitive to these buoyancy fluctuations, the local shear force (R_z) remains relatively stable. The shear force peaks at approximately 9,500 kN near the end of the sequence. Because this specific reaction force acts parallel to the monopile's longitudinal axis, it must be entirely resisted by the friction grip of the upending tool. Consequently, this 9,500 kN limit establishes the fundamental friction requirement for the gripper clamping system.

Force and Moment Evolution

To fully understand the mechanics driving the gripper reaction forces, it is necessary to examine the individual loads acting on the system. Figures 4.23 and 4.24 illustrate the evolution of the global vertical forces and the system moments, respectively, for the FSE with waves simulation.

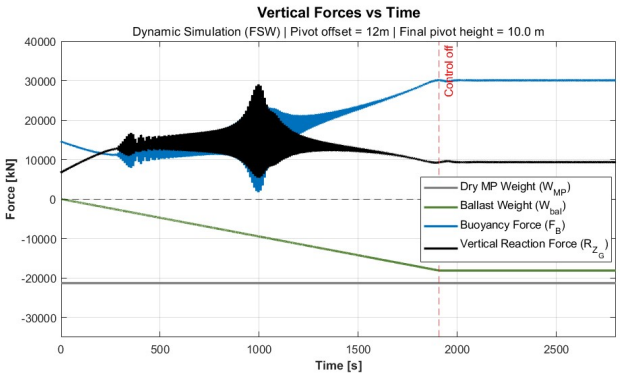

Figure 4.23: Evolution of the vertical forces over time. Buoyancy (F_B) dynamically adapts to counteract the constant dry weight (W_{mp}) and the linearly increasing ballast weight (W_{bal}).

As seen in Figure 4.23, the dry weight of the monopile (W_{mp}) remains a constant negative force, while the ballast weight (W_{bal}) increases linearly as the pumps actively fill the pile. As the system submerges, the hydrostatic buoyancy (F_B) increases. As the pile pitches towards the vertical orientation, a larger volume of the cylinder submerges into the water column, naturally generating the required massive buoyant lift (peaking near 30,000 kN). The global vertical reaction force ($R_{Z,G}$) acts as the final balancing mechanism, compensating for the difference between the total system weight and the available buoyancy.

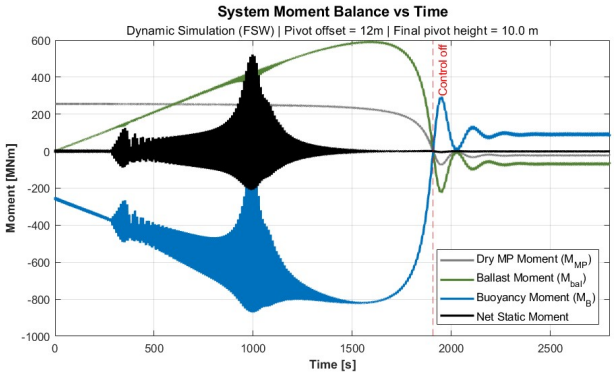

Figure 4.24: Evolution of the system moment balance over time. The hydrostatic restoring moment perfectly counteracts the combined overturning moments of the steel and ballast.

The moment balance (Figure 4.24) further illustrates the transition of the dynamic equilibrium. During the jacking and pumping phase, the overturning moments generated by the dry mass (M_{mp}) and the injected ballast (M_{bal}) are perfectly resisted by the massive restoring moment of the buoyancy (M_B).

As the control variables are halted ($t \approx 1,900$ s) and the monopile approaches the $90°$ vertical target, the horizontal lever arms for the center of gravity and the center of buoyancy rapidly approach zero. And, as indicated before, the steady current results in the fact that the monopile reaches an equilibrium state at approximately $95°$. So the moments stay at a baseline, near zero, to counteract the steady current.

4.7.2. Dynamic Stability and Eigenfrequency Analysis

To mathematically verify the cause of the severe load amplification observed in Section 4.7, an eigenfrequency check is conducted. This analysis tracks the system's shifting natural period over the duration of the upending to determine its vulnerability to wave-induced resonance.

The analytical foundation for the natural frequency relies on the unforced, undamped single-degree-of-freedom rotational equation of motion. The natural angular frequency is defined as:

$$\omega_n = \sqrt{\frac{K}{I_P}} \tag{4.32}$$

Where ω_n is the angular eigenfrequency, K is the rotational stiffness, and I_P is the total system inertia around the pivot point P, including the dynamically varying ballast and hydrodynamic added mass.

Analytically, rotational stiffness represents the rate of change of the net restoring moment with respect to the pitch angle, defined by the exact mathematical derivative:

$$K = \frac{dM_{net}}{d\theta} \tag{4.33}$$

However, the continuous variation of ballast mass, the shifting global pivot height, and the highly nonlinear buoyancy forces throughout the upending sequence prevent a closed-form algebraic derivation. To translate this analytical requirement into a numerical solution, the time domain is discretized. At each time step, the physical state variables (e.g., current ballast volume, pivot location, and draft) are momentarily frozen. A forward finite difference method is then applied to evaluate the local gradient of the restoring moment. The net static moment, consisting of the dry monopile weight, the FSE-adjusted ballast weight, and buoyancy, is evaluated at the current angle θ and at a marginally perturbed angle $\theta + \Delta\theta$:

$$K \approx \frac{\Delta M_{net}}{\Delta\theta} = \frac{M_{net}(\theta + \Delta\theta) - M_{net}(\theta)}{\Delta\theta} \tag{4.34}$$

This numerical slope provides the instantaneous stiffness, linearizing the complex restoring moment curve at that specific operating point. The computed eigenfrequency (ω_n) is then converted to the system's natural period ($T_n = \frac{2\pi}{\omega_n}$).

The evolution of the natural period throughout the FSE time-domain simulation is plotted in Figure 4.25.

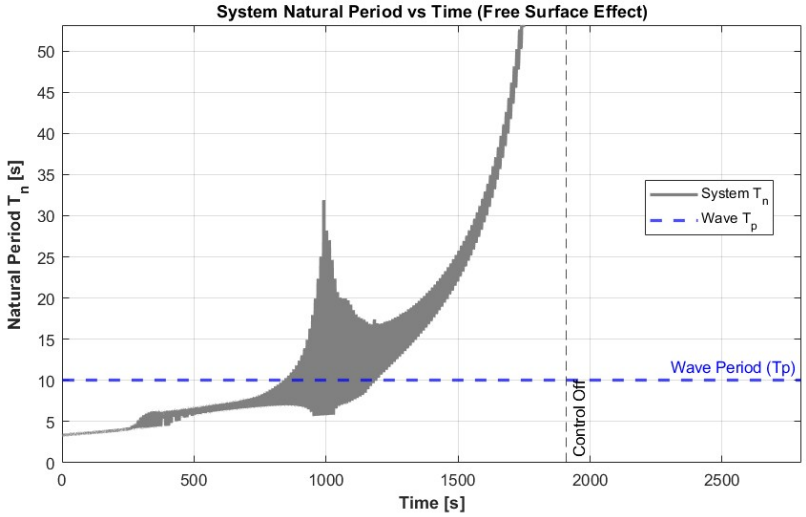

Figure 4.25: System natural period (T_n) vs. time. The resonance spike observed in the global force results is mathematically confirmed as the system's natural period crosses the 10 s wave excitation period at $t \approx$ 1,000 s.

The resulting graph provides mathematical confirmation of the dynamic instability. As the ballast fills and the geometry shifts, the rotational stiffness (K) drops while the total inertia (I_P) increases, causing the natural period to rapidly elongate. At $t \approx$ 1,000 s, the system's natural period perfectly intersects

the environmental wave period ($T_p = 10$ s). This direct harmonic alignment is the exact physical trigger for the 30,000 kN vertical load spike identified in the global force analysis.

Implications for Irregular Sea States

While the time-domain model utilizes a simplified, single sinusoidal regular Airy wave to demonstrate this resonance, real-world offshore operations occur in irregular sea states characterized by a broad spectrum of wave frequencies (e.g., a JONSWAP spectrum).

The eigenfrequency sweep in Figure 4.25 demonstrates that the system's natural period transitions from approximately 4 s to beyond 50 s. Typical North Sea wave spectra contain peak energy bands concentrated anywhere between 3 s and 14 s, which implies that the monopile will mathematically harmonize with the sea state at some point during the continuous upending sequence [79]. This confirms that the resonance observed with a singular wave frequency is a fundamental operational risk that necessitates mechanical mitigation.

Design Implication: Rotational Pitch Damping

To mitigate the extreme 30,000 kN vertical load spikes (Figure 4.22), a rotational pitch damping mechanism must be incorporated into the gripper design. Specifically, a unidirectional hydraulic braking system designed to heavily resist the returning upward motion of the pile will prevent the rapid loss of submerged volume. By actively damping the wave-induced pitch, the system will maintain the hydrostatic draft required to support the monopile's deadweight. Implementing this damping strategy will successfully suppress the resonance peaks, ensuring the global vertical forces acting on the gripper remain within safe, manageable structural limits.

4.8. Chapter Summary

This chapter successfully translated the physical constraints of craneless monopile upending into a definitive structural load envelope. First, the quasi-static grid search identified a practical geometric configuration by balancing seabed clearance requirements with the physical limits of a symmetric gripper design. This analysis established a feasible final global pivot height of $Z_{G,P} = 10$ m and a pivot offset of $z_{off} = 12$ m.

By using this configuration in a full dynamic time-domain simulation, the operational boundaries of the upending concept were mathematically verified. The integration of the Free Surface Effect (FSE) established that reaching full verticality requires an equivalent ballast fill volume of 1,803 m^3. Most notably, this buoyancy-assisted sequence successfully reduces the perceived weight of the monopile from a dry mass of 2,170 tonnes down to an effective load of just 950 tonnes. Consequently, the peak longitudinal shear force exerted on the gripper is 9,500 kN, while the transverse normal force peaks at 14,200 kN, when wave excitation is excluded.

In addition to defining this load envelope, the simulation revealed severe dynamic wave resonance during the upending sequence. This critical vulnerability dictates the mechanical necessity of a rotational pitch damper to maintain hydrostatic draft and suppress the 30,000 kN vertical load spikes.

With the global physics, dynamic boundaries, and required mechanical mitigations fully defined, the analysis now transitions to Chapter 5. This subsequent chapter details the local monopile gripper interface, evaluating the friction limits and pad geometry required to safely transfer the 9,500 kN shear demand without inducing slip or damaging the thin-walled monopile shell.

5

Local Interface Mechanics

Having established the global load envelope and peak upending forces in Chapter 4, the research must now address the structural interaction of the gripper and the monopile. Translating these demands into a secure local holding force presents a critical structural challenge: the friction gripper must exert extreme radial clamping forces, yet the highly optimized, thin-walled shell of modern monopiles is vulnerable to localized yielding and cross-sectional buckling. This chapter resolves this by developing a coupled analytical sizing tool that filters global operational demands through two structural assessments. By evaluating discrete localized yielding limits (the Micro filter) alongside global elastic shell stability criteria (the Macro filter), this framework maps a mathematically justified safe operating window for the gripper. Ultimately, this chapter establishes the local variables: optimized pad geometry, pad count, width, and length, that form the foundation for the functional concept design developed in Chapter 6.

5.1. Physics of the Frictional Interface

To safely capture the monopile, the discrete hydraulic pads must transfer massive radial loads into the steel shell. Before evaluating the complex structural boundaries of this interface, it is necessary to establish the magnitude of the forces involved using idealized mechanics.

5.1.1. Idealized Mechanics and the Baseline Demand

The dynamic analysis established a peak longitudinal shear load of 9,500 kN. To prevent slippage during the upending sequence, a safety factor (SF) of 1.5 is applied. Therefore, the gripper interface must guarantee a total vertical frictional holding capacity (F_{fric_req}) of 14,250 kN.

In a simplified, idealized mechanical model, the total required radial clamping force (F_{total}) and the required physical pad area (A_{req}) can be calculated linearly by assuming a constant coefficient of friction and a target nominal pressure. A target polymer pressure (σ_{nom}) of 2.0 MPa is selected, representing a highly efficient operating point for the friction pads. At this 2.0 MPa pressure, the idealized friction coefficient (μ_{nom}) is approximately 0.30.

Using standard Coulomb friction mechanics, the total required radial clamping force is calculated as:

$$F_{total} = \frac{F_{fric_req}}{\mu_{nom}} = \frac{14,250 \text{ kN}}{0.30} = 47,500 \text{ kN} \tag{5.1}$$

To maintain the target 2.0 MPa pressure under this massive clamping load, the idealized system requires a total physical contact area of:

$$A_{req} = \frac{F_{total}}{\sigma_{nom}} = \frac{47.5 \text{ MN}}{2.0 \text{ MPa}} = 23.75 \text{ m}^2 \tag{5.2}$$

This idealized calculation provides a mental anchor for the scale of the system: the gripper must squeeze the monopile with roughly 47,500 kN of total force, distributed over around 24 m^2 of polymer.

However, translating this baseline requirement into a physical layout reveals the limitations of idealized mechanics. As will be demonstrated, satisfying the complex structural limits of the thin-walled steel monopile and accounting for redundancy, ultimately forces the design to utilize more area (32 m^2) to simultaneously prevent local steel yielding and global elastic buckling.

5.1.2. The Dual Structural Threats: Micro vs. Macro

The application of high-magnitude radial loads onto a thin-walled cylinder introduces two distinct failure mechanisms, which must be evaluated at different structural scales:

- **The Micro Threat (Localized Plastic Yielding):** Because the clamping force is not applied as a continuous 360-degree fluid pressure, but rather through discrete hydraulic pads, the steel shell is forced into a localized bending condition. The unconstrained steel spanning the gaps between the pads bends inward under the discrete radial loads. If the pads are too narrow or spaced too wide, the resulting bending moments will exceed the yield limit of the steel (e.g., 355 MPa), causing localized plastic deformation or ”dimpling” at the pad interfaces.
- **The Macro Threat (Global Elastic Buckling):** Independent of how the discrete pads are arranged, the gross monopile cross-section must survive the sum total of the applied radial clamping force. The total compressive squeeze threatens the global geometric stability of the cylinder, potentially forcing the circular cross-section to ovalize and undergo elastic shell buckling.

These failure mechanisms will be checked in the following sections. First the empirical friction coefficient, used to assess these structural limits, is determined.

5.1.3. Pressure Dependent Friction Behaviour

In contrast to idealized Coulomb friction assumptions, experimental testing of the polymer–steel interface demonstrates that the coefficient of friction is not constant but strongly dependent on the applied normal contact pressure. Friction tests performed in the TWD laboratory show that, for the polymer pad material and coated steel surface under wet conditions, the friction coefficient decreases systematically with increasing contact pressure. The detailed explanation of these friction tests can be found in Appendix D.

This experimentally observed behaviour is represented by a fitted pressure-dependent friction model:

$$\mu(\sigma) = \frac{\exp(a\sigma + b) + c}{SF_\mu} \tag{5.3}$$

where μ is the friction coefficient, σ is the normal contact pressure applied to the pad in MPa, and a, b, and c are empirically derived constants obtained from the friction test programme and SF_μ is a factor coupled to the friction coefficient. The resulting fit for the wet coated steel configuration is shown in Figure 5.1.

The pressure-dependent nature of the friction coefficient introduces a non-linear coupling between gripper pad geometry, applied normal pressure, and required clamping force. Reducing the pad contact area by decreasing pad size or pad count increases the local contact pressure. According to the empirical friction model, this increase in pressure reduces the friction coefficient, which in turn necessitates a higher total clamping force to satisfy the global longitudinal holding demand. The increased clamping force further increases contact pressure, leading to the reduction in friction efficiency.

As a result, the frictional holding capacity of the gripper cannot be assessed using closed-form expressions with a constant friction coefficient. Instead, the interface behaviour must be evaluated through an equilibrium formulation in which the pressure-dependent friction coefficient is accounted for. For a given pad geometry and pad count, the contact pressure adapts until the frictional resistance generated by the pads exactly balances the required longitudinal holding force.

This non-linear friction-pressure interaction forms a central design driver within the local gripper interface model. It directly links geometric design choices to both local structural limits (via pad pressure and shell bending) and global stability limits (via total clamping force). Resolving this interaction therefore requires an iterative equilibrium solver, as developed and applied in the following sections.

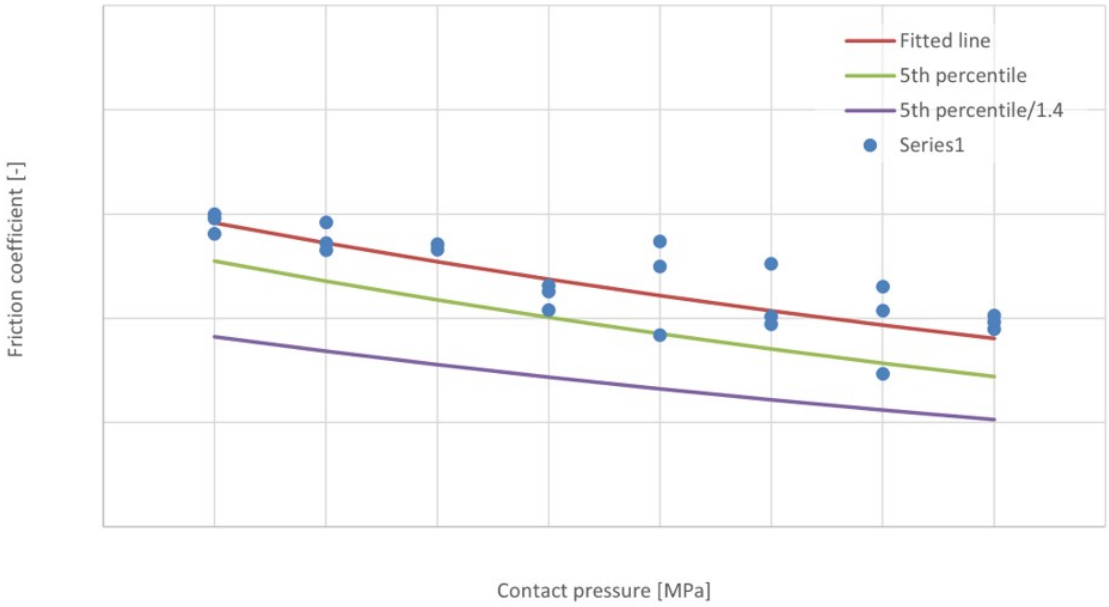

Figure 5.1: Pressure-dependent friction coefficients for the polymer-coated steel interface under wet conditions. Measured data points, fitted trend, and conservative lower-bound friction curve are shown.

5.2. Local Yield Capacity (Micro filter)

The main objective is to determine the minimum required pad count (n) and the discrete pad dimensions ($L_{pad} \times W_{pad}$), as defined in Figure 5.2. These parameters must be sized to simultaneously keep the contact pressure below the polymer crushing limit and prevent the discrete hydraulic loads from plastically yielding the localized steel shell.

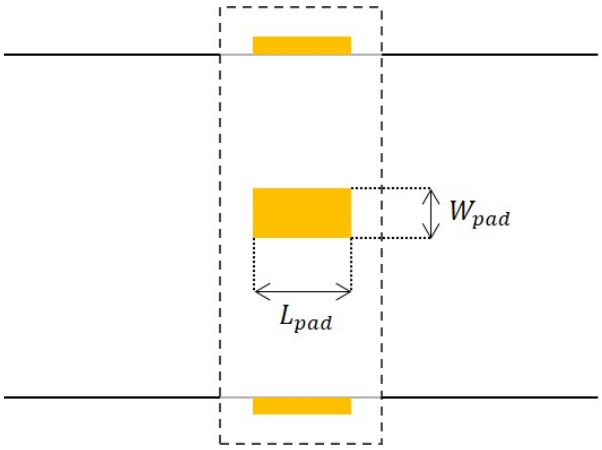

Figure 5.2: Schematic defining the gripper pad dimensions, including the pad length (L_p) and pad width (W_p).

5.2.1. Defining the Equilibrium Clamping Demand

Before evaluating the structural response of the steel, the exact radial force exerted by each individual pad (F_{pad}) must be established. As detailed in Equation 5.3, the empirical friction coefficient $\mu(\sigma)$ degrades with increasing contact pressure (σ). Therefore, the true clamping force cannot be determined algebraically; it must be found through a numerical equilibrium solver.

To achieve static equilibrium during upending, the frictional holding force generated by a single pad must exactly equal its required share of the global 14,250 kN shear demand:

$$\sigma \cdot A_{pad} \cdot \mu(\sigma) - F_{req\_per\_pad} = 0 \tag{5.4}$$

Where A_{pad} is the physical contact area of a single pad ($W_{pad} \times L_{pad}$), $\mu(\sigma)$ is the pressure-dependent friction coefficient, and σ represents the applied normal pad pressure in MPa. $F_{req\_per\_pad}$ is the total global holding demand divided by the total number of pads in the system.

Because the unknown pressure variable (σ) exists both as a variable multiplier and within the exponential decay function of $\mu(\sigma)$, an iterative root-finding algorithm (MATLAB's `fzero` function) was employed. This solver iteratively searches for the exact equilibrium pressure that satisfies the equation above. Once the equilibrium pressure (σ) is found, it is compared against the maximum allowable polymer bearing limit (10 MPa) to ensure material survival. If the polymer constraint is satisfied, the true normal force per pad ($F_{pad} = \sigma \cdot A_{pad}$) is exported to the structural bending model.

5.2.2. Local Steel Yielding (Roark's 2D Ring Bending)

With the discrete radial force (F_{pad}) defined, the structural response of the monopile wall is evaluated. Because the clamping force is applied at discrete intervals around the circumference, the shell is forced to bend sharply inward at the pad locations and outward in the unconstrained gaps between them.

7. Ring under any number of equal radial forces equally spaced

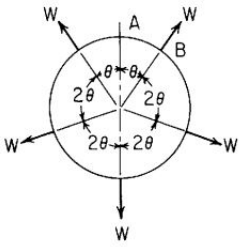

For $0 < x < \theta$ $\quad M = \frac{WR(u/s - k_2/\theta)}{2}$ $\quad N = \frac{Wu}{2s}$ $\quad V = \frac{-Wz}{2s}$

$\text{Max} + M = M_A = \frac{WR(1/s - k_2/\theta)}{2}$ $\quad \text{Max} - M = \frac{-WR}{2}\left(\frac{k_2}{\theta} - \frac{c}{s}\right)$ at each load position

Radial displacement at each load point $= \Delta R_B = \frac{WR^3}{EI}\left[\frac{k_1(\theta - sc)}{4s^2} + \frac{k_2 c}{2s} - \frac{k_2^2}{2\theta}\right]$

Radial displacement at $x = 0, 2\theta, \ldots = \Delta R_A = \frac{-WR^3}{EI}\left[\frac{k_1(s - \theta c)}{4s^2} - \frac{k_2}{2s} + \frac{k_2^2}{2\theta}\right]$

If $\alpha = \beta = 0$, $M = K_M WR$, $\Delta R = K_{\Delta R} WR^3/EI$

θ	15°	30°	45°	60°	90°
K_{M_A}	0.02199	0.04507	0.07049	0.09989	0.18169
K_{M_B}	−0.04383	−0.08890	−0.13662	−0.18879	−0.31831
$K_{\Delta R_B}$	0.00020	0.00168	0.00608	0.01594	0.07439
$K_{\Delta R_A}$	−0.00018	−0.00148	−0.00539	−0.01426	−0.06831

Figure 5.3: Roark's formula for a circular ring under any number of equal radial forces equally spaced [80].

The monopile is analyzed using Roark's formulas for circular rings (Figure 5.3) to assess the localized bending stresses. A 1-meter longitudinal slice of the monopile is isolated and treated as a 2D closed ring. To map the 3D pad force to the 2D Roark formula, the discrete pad force is first converted into a longitudinal line load, which acts as the radial point load (W) on the 1-meter ring slice:

$$W = \frac{F_{pad}}{L_{pad}} \tag{5.5}$$

According to Roark's formulas for a ring under any number of equal radial forces equally spaced, the maximum bending moment occurs directly at each load position. The magnitude of this peak bending moment (M_{max}) is defined as [80]:

$$M_{max} = \frac{W \cdot R}{2}\left(\frac{k_2}{\theta} - \frac{c}{s}\right) \tag{5.6}$$

where:

- R is the radius to the centroid of the cross-section.
- θ is half the angular spacing between adjacent loads, defined as $\theta = \pi/n$.
- $s = \sin\theta$ and $c = \cos\theta$.

- k_2 is a constant defined in Roark's Table 9.2 as $1 - \alpha_h$ [80], where α_h is the hoop-stress deformation factor ($\alpha_h = I/(A \cdot r^2)$). For a thin-walled cylinder with an extremely small thickness-to-radius ratio ($t/r \approx 0.024$), α_h is mathematically negligible ($\alpha_h \approx 5 \times 10^{-5}$), justifying the simplification of k_2 to unity (1.0).

To convert this bending moment into a localized bending stress (σ_b), the model relies on classical thin shell theory. According to the Kirchhoff-Love assumptions [81], a straight line normal to the shell's mid-surface remains straight and normal even after bending. Because the wall thickness ($t = 0.110$ m) is very small relative to the overall radius ($r = 4.5$ m), the stress distribution through the thickness is assumed to be linear. Consequently, the local cross-section of the curved steel can be treated identically to a flat rectangular plate. This theoretical foundation justifies calculating the peak localized bending stress (σ_b) using the elastic section modulus of a flat, solid rectangle (W_{slice}):

$$W_{slice} = \frac{1}{6} \cdot b \cdot t^2 \tag{5.7}$$

where b is the 1-meter unit height of the ring slice ($b = 1.0$ m), and t is the wall thickness. The resulting peak bending stress is thus defined as:

$$\sigma_b = \frac{M_{max}}{W_{slice}} \tag{5.8}$$

If σ_b exceeds the 355 MPa yield strength of the steel, the configuration fails the micro filter, indicating that the chosen geometry is insufficient to prevent localized plastic dimpling.

5.2.3. Parametric Design Space Exploration

To systematically determine the final interface dimensions, a deterministic parametric study was conducted rather than arbitrarily selecting a single geometry. A bounded design space was established for the primary configuration variables: pad count ($n \in [4, 6, 8, 10, 12]$) and ring count ($N_{rings} \in [1, 2]$). How the pad count is defined can be seen in Figure 5.4

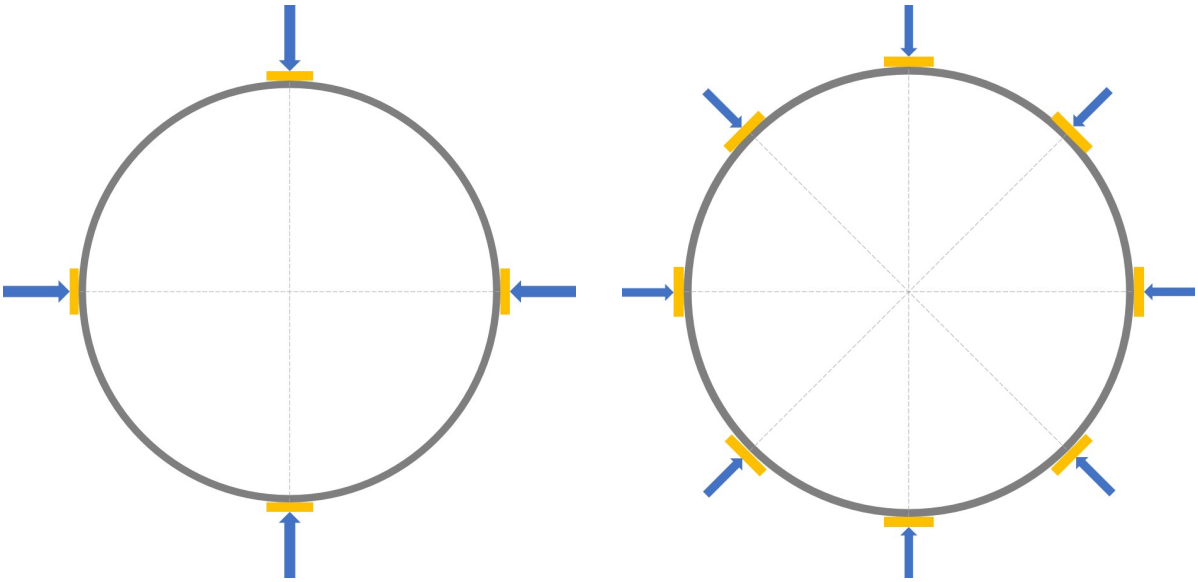

(a) 4-pad configuration **(b)** 8-pad configuration

Figure 5.4: Cross-sectional layout comparison showing 2 possible pad configurations: The 4-pad configuration (left) requires higher individual clamping forces (indicated by larger arrows). The optimized 8-pad configuration (right) needs lower individual forces (smaller arrows).

For the physical pad geometry the dimensions of 2.0 m x 1.0 m (L_{pad} x W_{pad}). Where the length (L_{pad}) of the pad was deliberately chosen to be longer than the width (W_{pad}) as the Equation 5.5 shows that increasing the length lowers the stress on the system.

5.2.4. Yield Results

As illustrated in Figure 5.5, configurations utilizing only 4 pads per ring significantly exceed the steel yield limit, even when distributed across two rings. While a 6-pad, 2-ring configuration technically satisfies the yield criterion, it operates dangerously close to the 355 MPa threshold.

Consequently, the analytical filter highlights the structural viability of an 8-pad configuration. By employing an $n = 8$ layout across two vertical rings ($N_{rings} = 2$) combined with pad dimensions of 2.0 m x 1.0 m, the peak local bending stress is reduced to a safe and acceptable level of approximately 180 MPa. Furthermore, this expanded contact area limits the required equilibrium pad pressure to approximately 1.5 MPa (Figure 5.6). This keeps the polymer pad completely safe and ensures the empirical friction coefficient remains highly efficient (Figure 5.1). The total applied clamping force to achieve the required friction force is 40,000 kN.

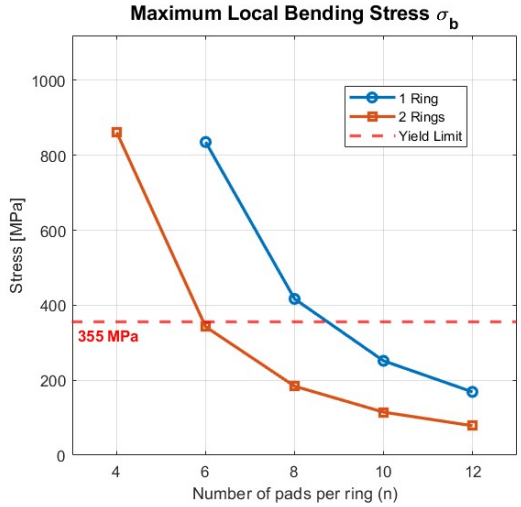

Figure 5.5: Maximum local bending stress (σ_b) evaluated against the number of pads per ring (n) for 1-ring and 2-ring configurations. The red dashed line indicates the steel yield limit (355 MPa).

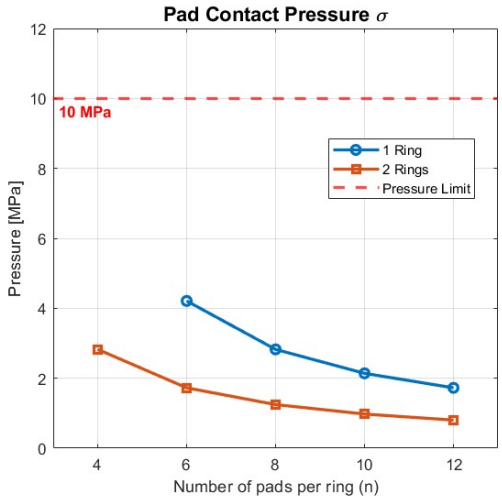

Figure 5.6: Pad contact pressure (σ) evaluated against the number of pads per ring (n) for 1-ring and 2-ring configurations. The red dashed line indicates the polymer pressure limit (10 MPa).

Having successfully satisfied the local yield limits, this 8×2 baseline geometry must now be subjected to the Macro filter to ensure that the resulting total clamping force does not threaten the global stability of the monopile cross-section.

5.2.5. Critical Evaluation of Analytical Assumptions

To ensure the Sizing Tool produces a robust Concept Design, the micro filter methodology intentionally utilizes two highly conservative structural assumptions:

- **The disc assumption (2D vs. 3D Shell Mechanics):** By isolating a 1-meter horizontal slice of the monopile, the Roark model assumes this specific 2D ring must independently resist 100% of the localized bending moment. In reality, the 90-meter monopile is a continuous 3D shell. According to the principles of classical shell theory and St. Venant's principle [82], the undisturbed steel extending longitudinally above and below the gripper provides substantial rotational and radial stiffness to the loaded cross-section. This 3D structural engagement, quantified in industry standards like DNV-RP-C202 through the concept of equivalent length [83], is entirely ignored in the 2D Roark model. Consequently, this isolation increases the calculated stress (σ_b), guaranteeing a substantial safety margin.
- **The Line Load Simplification:** While the physical gripper pad features a substantial circumferential width (W_{pad}), the Roark calculation compresses the applied force into an infinitely narrow line load (W). The line load assumption basically concentrates the force on a smaller area, overestimating the force and resulting in a conservative design.

5.3. Global Buckling Capacity (Macro Filter)

While the yield checks of the micro filter succesfully sized the pad geometry (2.0 m x 1.0 m) and layout (8×2 configuration) to prevent local yielding, it does not account for the geometric stability of the monopile cross-section. The objective of the second analytical phase is to serve as a final verification check, ensuring that the total clamping force required by the selected geometry does not induce global elastic shell buckling.

5.3.1. Elastic Buckling Capacity (f_{Eh})

For thin-walled cylinders subjected to external radial pressure, failure typically occurs through geometric instability (buckling) at stress levels lower than the material's yield strength. While classical shell theory defines this critical buckling pressure as a function of the material's elastic modulus and the shell's radius-to-thickness ratio [81], this Sizing Tool directly adopts the conservative industry standard defined in DNV-RP-C202 [83].

For unstiffened circular cylinders satisfying the "long cylinder" condition ($l/R > 2.25\sqrt{R/t}$), the characteristic elastic buckling strength (f_{Eh}) for lateral pressure, as defined in section '3.4.2 Shell Buckling', in DNV-RP-C202 [83], is defined as:

$$f_{Eh} = 0.25E\left(\frac{t}{R}\right)^2 \tag{5.9}$$

Given the 90 m length (l) and 4.5 m radius (R) of the monopile, the long cylinder condition is easily satisfied (l/R = 20 > 14.39). Based on the wall thickness (t) of 0.110 m and Equation 5.9, the theoretical buckling ceiling for the monopile is established at approximately 31.4 MPa.

5.3.2. The Smearing Strategy and Equivalent Length (l_{eo})

To evaluate the applied clamping demand against the 31.4 MPa hoop stress capacity, the discrete forces from the hydraulic pads must be translated into a global hoop stress. However, calculating stress based solely on the physical height of the pads (L_{pad}) results in an overly conservative model that ignores the structural continuity of the shell.

A localized radial load distributes longitudinally into the adjacent shell material. Because the gripper pads act simultaneously around the circumference, the system is modeled structurally as a temporary, external ring frame. To quantify the zone of structural engagement, the Sizing Tool adopts the DNV-RP-C202 definition from section '2.2.4 Circumferential membrane stress' for the "equivalent length" (l_{eo}) of shell plating that acts together with a ring frame [83]:

$$l_{eo} = 1.56\sqrt{R \cdot t} \tag{5.10}$$

Assuming sufficient longitudinal spacing between the rings to prevent overlapping decay zones, the total effective length (L_{eff_total}) of the monopile wall actively resisting the radial crush for a multi-ring configuration (N_{rings}) is the combined sum of the physical pad footprints and their associated DNV-defined equivalent lengths:

$$L_{eff\_total} = N_{rings} \cdot (L_{pad} + l_{eo}) \tag{5.11}$$

5.3.3. Applied Stress vs. Buckling Capacity

With the effective length established (equation 5.11), the True Total Clamping Force (F_{total}) demanded by the friction equilibrium solver is mathematically "smeared" into an equivalent uniform external pressure (p_{eq}):

$$p_{eq} = \frac{F_{total}}{2\pi \cdot R \cdot L_{eff\_total}} \tag{5.12}$$

Finally, the applied circumferential membrane (hoop) stress ($\sigma_{h,Sd}$) is calculated using the thin-walled pressure vessel relation [84]:

$$\sigma_{h,Sd} = \frac{p_{eq} \cdot R}{t} \tag{5.13}$$

The baseline geometry is deemed globally stable only if $\sigma_{h,Sd} \leq f_{Eh}$.

5.3.4. Evaluation of Global Stability Results

For the final selected 8×2 geometry, the total effective resisting length (L_{eff_total}) expands to 6.20 m. When the true equilibrium clamping demand ($\approx 40,000$ kN) is distributed over this area, the smeared equivalent pressure (p_{eq}) is a mere 0.16 MPa. This results in an applied hoop stress of only 9.32 MPa, which sits well below the 31.37 MPa elastic buckling limit, providing a safety factor of approximately 3.4 against global cross-sectional collapse.

This verification also highlights the structural benefit of the chosen pad aspect ratio. In the micro filter, prioritizing longitudinal pad length (L_{pad} = 2.0 m) over circumferential width (W_{pad} = 1.0 m) was mathematically favorable for lowering the local Roark line load. The same applies for the global buckling check. Because the equivalent length (l_{eo}) acts as an additive decay zone, utilizing a longer pad substantially expands the total structural resistance zone.

5.3.5. Assumptions and Limitations of the Global Buckling Check

While the DNV-based macro filter provides a verification of global stability, it relies on two critical analytical simplifications:

- **The Smearing Limitation:** The global buckling model assumes a perfectly uniform 360-degree distribution of force. It is blind to the fact that the actual load is applied via discrete patches. This structural blind spot reinforces why the discrete yield check was a mandatory check: the macro model ensures the gross cross-section remains geometrically stable, while the micro model ensures the shell does not fail locally beneath the discrete load patches.
- **Geometric Imperfections:** The theoretical f_{Eh} limit assumes a mathematically perfect cylinder. In physical reality, monopiles contain weld seams and out-of-roundness tolerances that structurally reduce the actual buckling capacity. The buckling check keeps a massive safety margin, where applied hoop stress is roughly a third of the theoretical capacity, ensuring the concept design is sufficiently robust to cope with real-world geometric imperfections.

5.4. Synthesis and Conclusion: Defining the Concept Baseline

The objective of this chapter was to translate the 9,500 kN required shear force into a structurally sound, viable geometry. The yield test demonstrated that trying to satisfy the friction demand with fewer pads resulted in localized yielding, due to more concentrated line loads. The Global Buckling Capacity check showed that the gripper interface needs to distribute the clamping force along sufficient longitudinal length to prevent buckling.

The analytical synthesis established the local parameters to be an 8 $\times$ 2 pad configuration (8 pads per ring across 2 vertical rings) and utilizing discrete pad dimensions of 2.0 $\times$ 1.0 m, represents an optimal baseline geometry. This specific architecture succesfully passes the investigated structural threats:

- **Polymer and Friction Stability:** The total contact area keeps the equilibrium pad pressure low (1.5 MPa), protecting the polymer from crushing and ensuring the empirical friction coefficient remains highly efficient.
- **Local Yield Prevention:** By utilizing 8 discrete loading lines and prioritizing an elongated pad length (L_{pad} = 2.0 m) to lengthen the radial line load, the peak local bending stress is restricted to approximately 180 MPa, well below the 355 MPa steel yield limit.
- **Global Buckling Prevention:** The total equivalent length of 6.20 m, combined with the total clamping demand of 40,000 kN generates an applied hoop stress of only 9.32 MPa against a theoretical buckling capacity of 31.37 MPa.
- **System redundancy:** The chosen configuration passes both checks. a 6-pad configuration would just survive the yield check. Thus the system has built in redundancy: for each ring, 2 cylinders could fail and the system would still generate enough friction force without yielding or buckling the system.

5.4.1. Scope of Applicability and Future Numerical Verification

While the analytical sizing tool relies on conservative assumptions to guarantee a structural safety margin, these calculations serve strictly to establish a mathematically defensible baseline concept.

In physical offshore operations, the monopile is subjected to highly complex, multi-axial stress states, most notably, the interaction between the massive global bending moment generated by the overhanging pile and the local radial compression from the gripper. As stated in Section 1.3 of DNV-RP-C202 [83], when buckling recommendations are not provided for such complex interactions, the final design must be verified through advanced numerical analysis (Finite Element Method, FEM)

To realize this design for actual fabrication, a comprehensive non-linear FEM study would be required to account for geometric imperfections, material non-linearities, residual stresses, and the exact multi-axial stress concentrations at the pad edges. However, executing a non-linear FEM simulation falls outside the conceptual scope of this thesis.

Instead, the analytical boundary conditions established in this chapter have successfully supported the next phase of the development process. The resulting local variables are the optimized 8×2 interface geometry and serve as the physical gripper interface foundation for Chapter 6.

6

Functional Concept Design

The preceding chapters established the theoretical and analytical foundations for the proposed crane-less, buoyancy-assisted upending method. Chapter 4 defined the global dynamic behaviour of the system, yielding the global parameters such as the required vertical jacking distance, the pivot offset, the required ballast weight, and the need for rotational damping. Subsequently, Chapter 5 investigated the local friction interface resulting in the local variables, such as the required pad configuration and dimensions necessary to safely transfer the 9,500 kN maximum clamping force to the monopile without inducing structural failure.

The objective of this chapter is to translate these global and local variables into a physically realizable, functional mechanical concept by applying a systematic design method.

6.1. Design Scope

To define the boundaries, it is necessary to establish the scope of the design presented in this chapter. The proposed design is a functional concept aimed at demonstrating the kinematic feasibility of the upending method.

Therefore, the scope of this chapter includes:

1. **System kinematics:** The mechanisms required to accommodate the simultaneous ballasting, pitching, and vertical translation of the monopile.
2. **Geometry and layout:** The arrangement of the gripper frame, the pitch hinge, and the vertical jacking system relative to a JUV.
3. **Interface dimensions:** The 8x2 friction pad configuration validated in Chapter 5.
4. **Conceptual actuation logic:** Descriptions of the hydraulic and damping strategies required to drive the kinematics and dampen the wave-induced motions.

Detailed mechanical engineering of the system as well as the integration of the design of a conventional gripper fall outside the scope of this conceptual phase. Therefore, the scope excludes:

1. **Detailed structural sizing:** The exact determination of steel plate thicknesses, bolted connections, and weld dimensions.
2. **Finite Element Method (FEM) verification:** Detailed stress and buckling checks of the gripper frame and the monopile.
3. **Component specification:** The exact sizing and commercial selection of individual hydraulic cylinders, pumps, and mechanical dampers.
4. **Post-upending handling and piling support system:** The integration of a conventional vertical gripper used for pile guiding, alignment, and support during final installation is excluded. This system is assumed to take over once the monopile reaches a stable vertical orientation.

6.2. Functional Breakdown and Concept Development

The operational goal: safely gripping, translating, and rotating a floating monopile into a vertical position, must be divided into manageable sub-functions. This functional breakdown guides organized concept development.

6.2.1. Functional Breakdown

The overarching problem was divided into the following sub-problems:

1. **Vertical motion of the gripper:** Translating the system along the JUV to acquire the required vertical height.
2. **Gripper kinematics (Open/Close):** The structural mechanism required to encompass the floating monopile.
3. **Gripper actuation:** The actuation types used to open/close the arms.
4. **Gripper locking:** The mechanical locks used to secure the gripper arms safely once closed.
5. **Structural ring and pad design:** The global shape of the gripper frame and the arrangement of the friction pads (incorporating the 8x2 layout).
6. **Pad pressure application:** The mechanism responsible for actively applying the required radial clamping force.
7. **Rotational joint:** The mechanical hinge allowing the transition from a horizontal to a vertical orientation.
8. **Pitch and yaw damping:** The systems required to mitigate wave-induced rotational resonance during the upending procedure.

6.2.2. The Morphological Chart

For each sub-problem, various working principles and partial solutions were brainstormed. These partial solutions range from standard offshore handling equipment (e.g., rack and pinion drives, slewing rings) to conceptual hydraulic and friction-based mechanisms.

The resulting solution space is mapped in a morphological chart, presented in Figure 6.1. This chart serves as the foundational matrix for the concept generation phase.

Three distinct conceptual paths were explored. For each path, a flow diagram was created onto the morphological chart, detailing the specific combination of sub-solutions chosen, alongside the pros and cons of those selections. They form the basis of the concept designs evaluated in the following section.

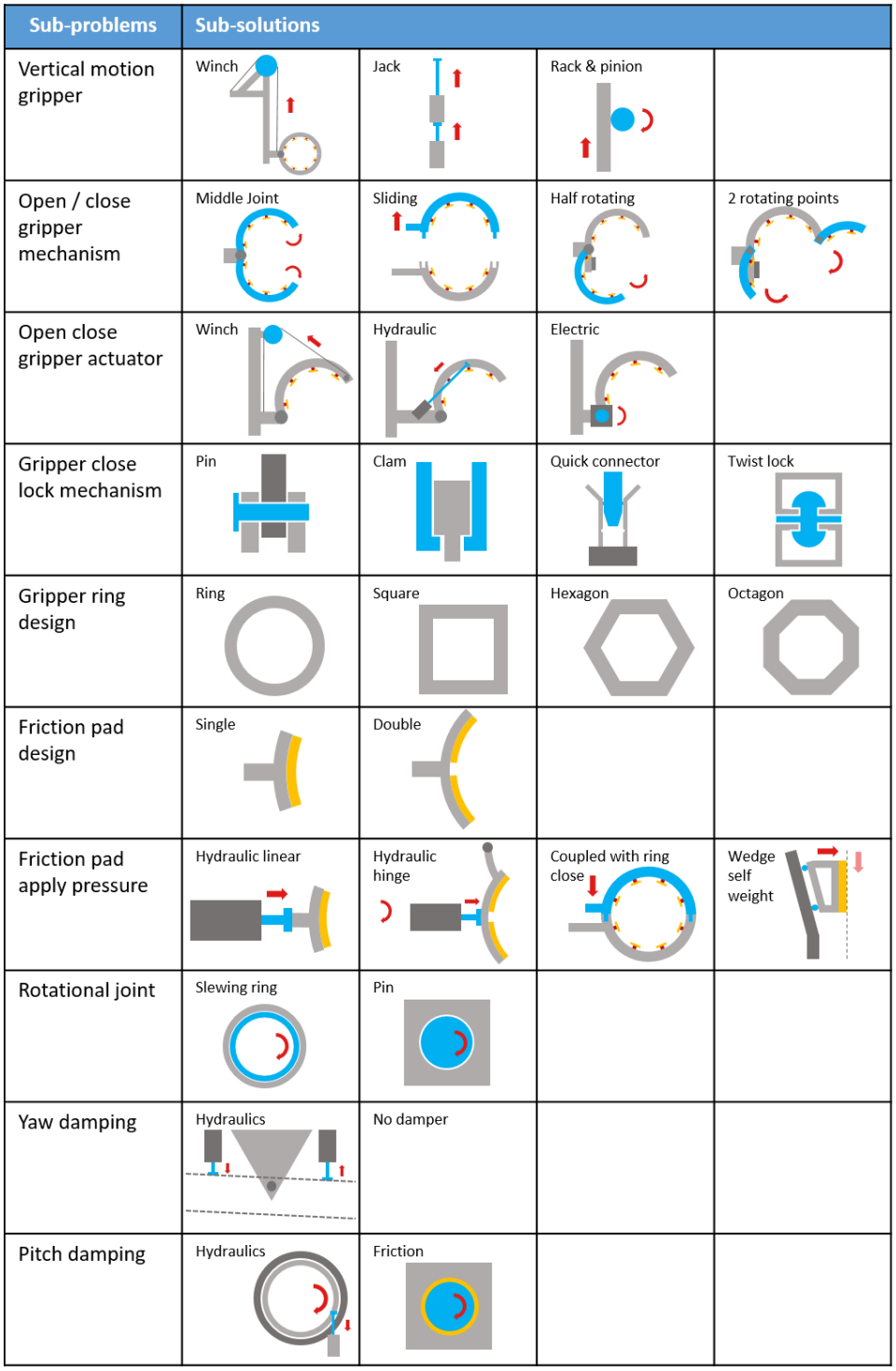

Figure 6.1: The morphological chart showing the sub-problems of the upending operation with various partial mechanical solutions.

6.2.3. Concept 1: Sliding Gripper

The first concept is created by following a flow chart laid over the morphological chart as indicated with Figure 6.2.

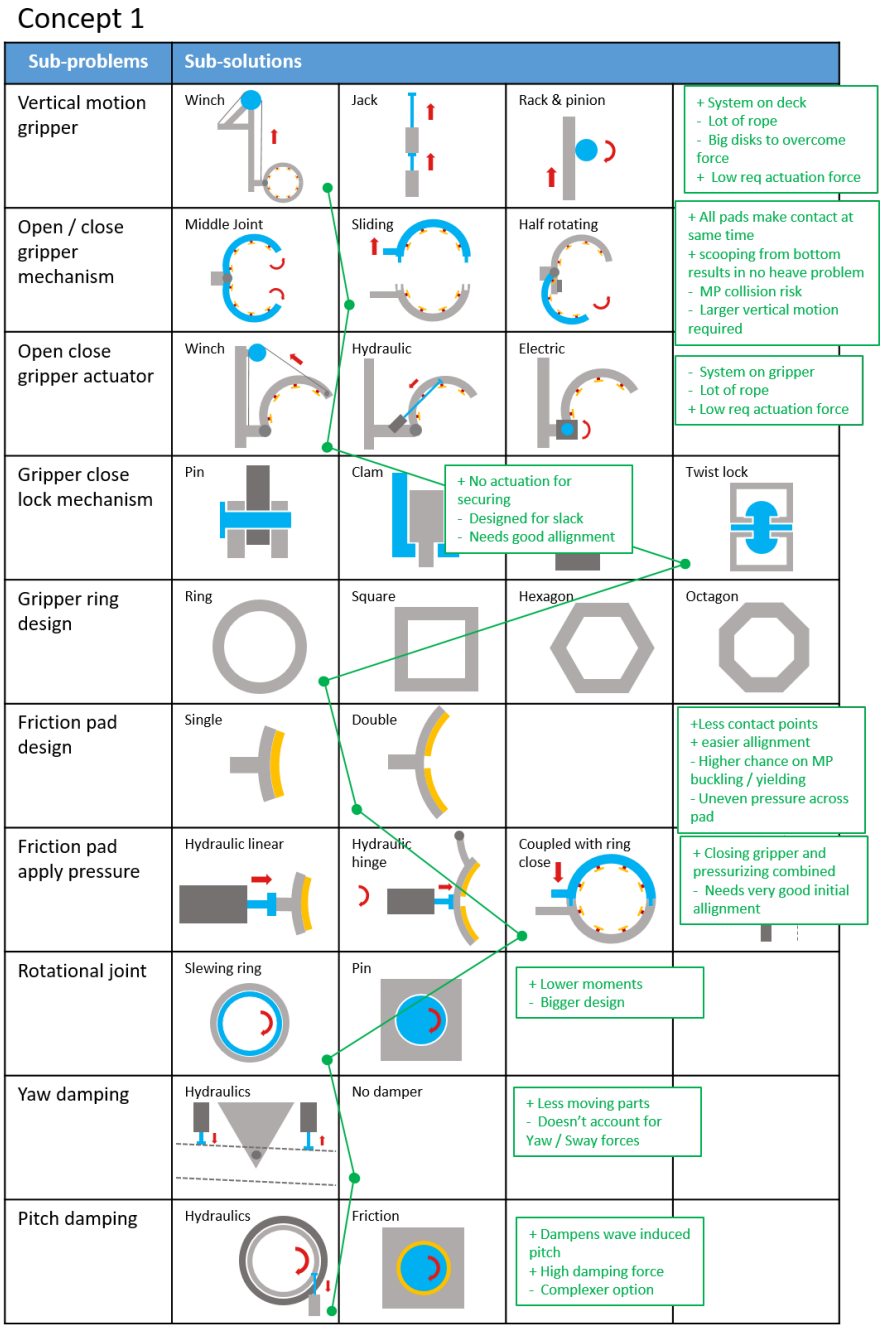

Figure 6.2: The flowchart of the first concept.

The first concept, illustrated in Figure 6.3, utilizes a deck-mounted hoisting approach combined with a vertically sliding clamping mechanism.

Vertical Translation: The vertical motion required to accommodate the vertical distance is actuated by a heavy-duty winch system situated on the deck of the JUV. This winch mechanically hoists the entire gripper assembly along vertical guide rails attached to the vessel.

Gripper Kinematics: The mechanism designed to encompass the floating monopile operates via a vertical sliding action. The lower half of the friction harness acts as a structural cradle and is rigidly fixed to the main translating frame. To capture the pile, only the upper arm of the assembly is actuated, sliding vertically downwards to enclose the cylindrical cross-section.

Pad Pressure Application and Locking: The design is such that the required normal force is applied to the friction pads simultaneously with the final closing stroke of the upper arm. This eliminates the need for an independent, secondary clamping actuation system. Once fully engaged, the structural harness is secured using a mechanical twist-lock system, providing a robust mechanical fail-safe against unintentional opening during the dynamic upending phases.

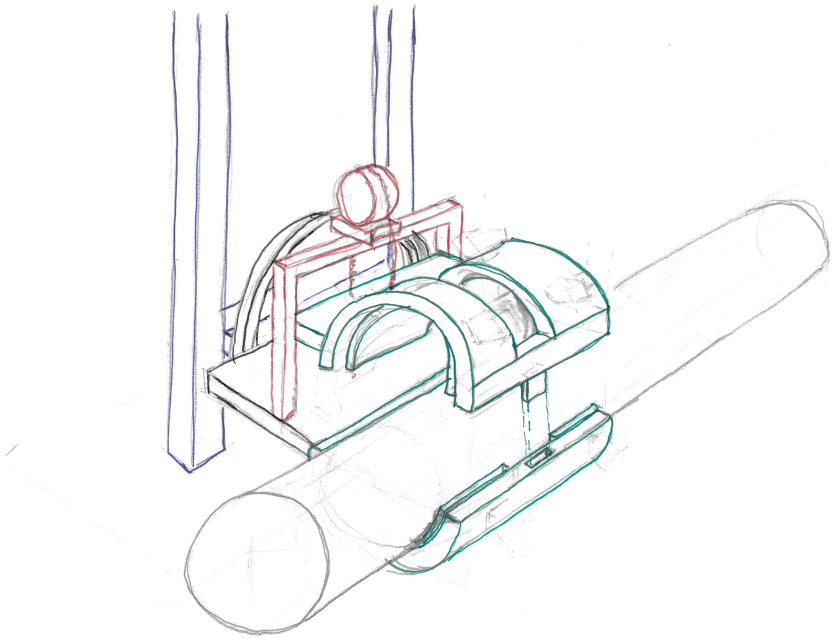

Figure 6.3: 3D sketch of Concept 1, featuring a deck-mounted winch for vertical translation and a vertically sliding upper gripper arm with coupled force application.

6.2.4. Concept 2: Radial Hydraulic Gripper

The second concept is created by following a different flow chart laidd over the morphological chart as indicated with Figure 6.4.

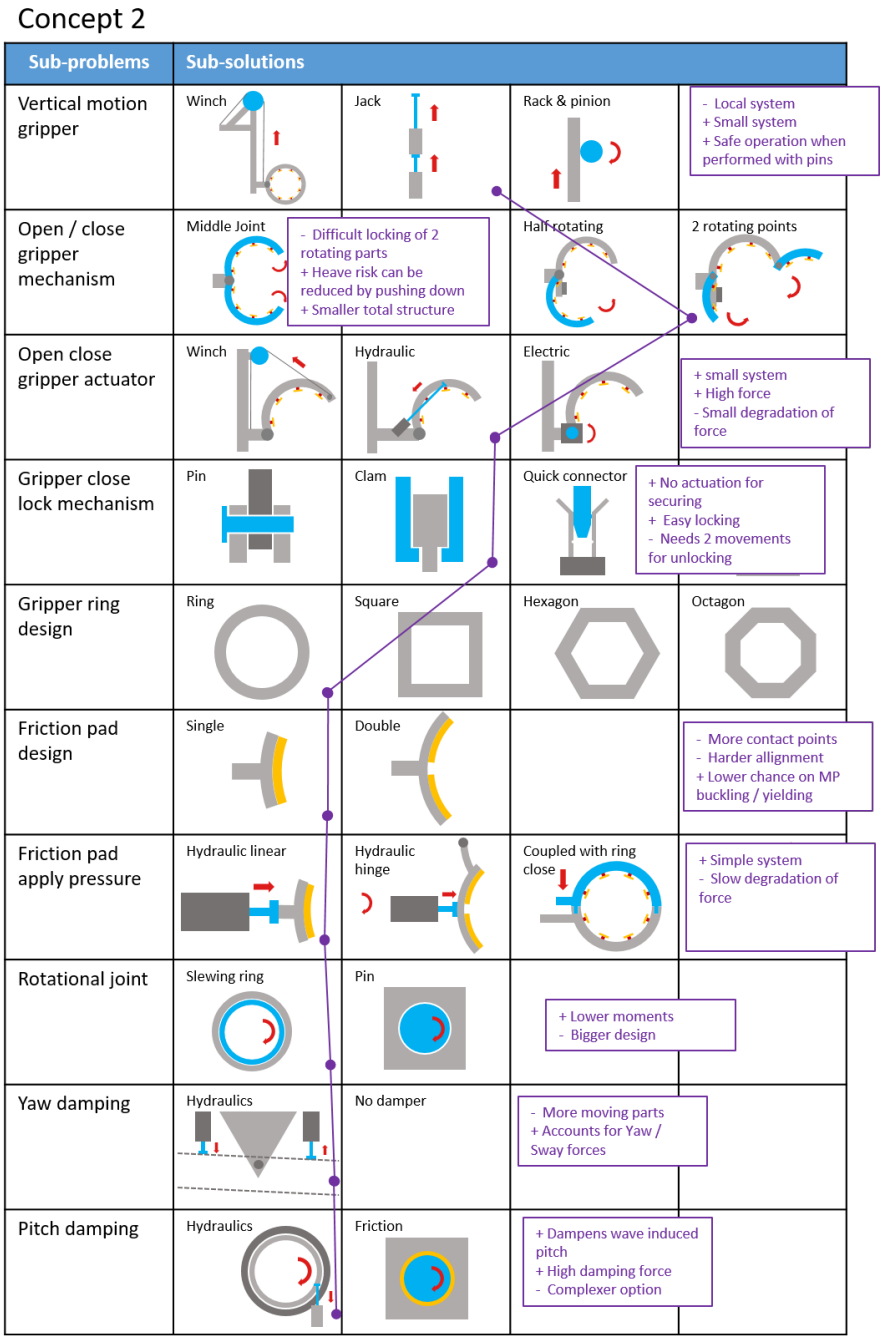

Figure 6.4: The flowchart of the second concept.

The second concept, shown in Figure 6.5, utilizes a hydraulic caterpillar jacking system for vertical translation and an active, multi-cylinder approach for radial clamping.

Vertical Translation: The vertical motion is achieved via a hydraulic caterpillar skidding mechanism, operating on a push-pull (or pin-hole) principle along the vessel's guide rails. Hydraulic cylinders stroke upwards to lift the entire gripper assembly. Once the stroke length is reached, mechanical locking pins engage with the rail to secure the load. The hydraulic cylinders then retract to reset their position, repeating the cycle to gradually jack the system to the required vertical height.

Gripper Kinematics: In contrast to the scooping motion of Concept 1, this concept captures the monopile from above. The upper half of the friction harness is rigidly fixed to the main translating frame. The lower half consists of two hinged, quarter-circle swing arms. During engagement, these arms open outward, allowing the rigid top structure to be lowered directly onto the floating monopile. The arms are then hydraulically actuated to swing inward, encompassing the lower circumference of the pile.

Gripper Locking: Once the swing arms are fully closed, they are structurally secured to one another at the bottom centreline using a heavy-duty mechanical pin connection. This transforms the open jaws into a closed structural ring, essential for safely transferring the radial loads.

Pad Pressure Application: The application of the required normal force is entirely decoupled from the closing kinematics. Instead, the force is actively applied by an array of individual linear hydraulic cylinders mounted radially behind each of the friction pads within the 8x2 configuration. This direct-acting cylinder approach allows for highly precise, independent control of the friction force applied to the monopile.

Yaw rotation and Damping: To lower structural stresses induced by transverse wave loads (previously assumed to be absorbed by the structure), the system incorporates a rotational degree of freedom in the yaw direction. This allows the assembly to dampen out-of-plane sway forces, thereby reducing the forces and bending moments transferred into the JUV structure.

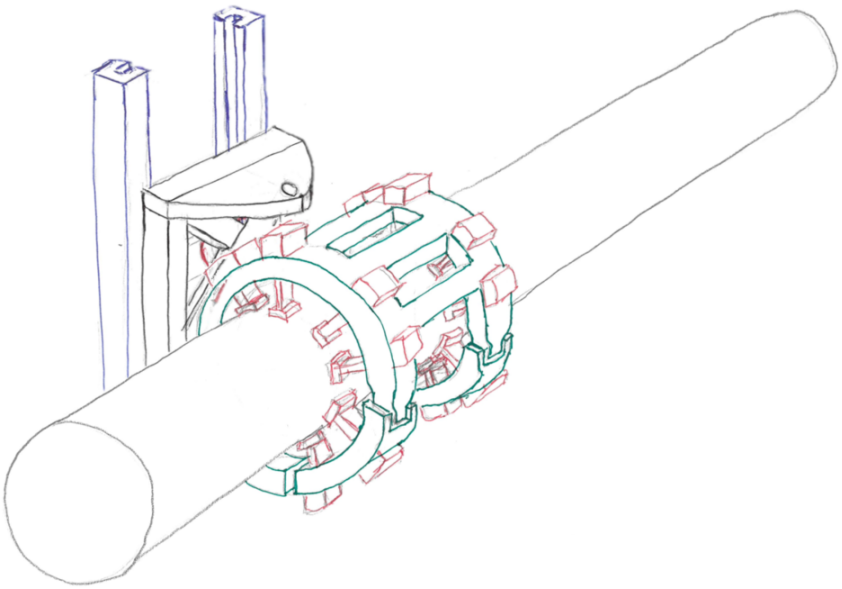

Figure 6.5: 3D sketch of Concept 2, featuring a hydraulic skidding mechanism for vertical translation, hinged swing-arms, and active radial hydraulic cylinders for pad pressure application.

6.2.5. Concept 3: Self-Locking Wedge Gripper

The third concept is created by following a different flow chart laid over the morphological chart as indicated with Figure 6.6.

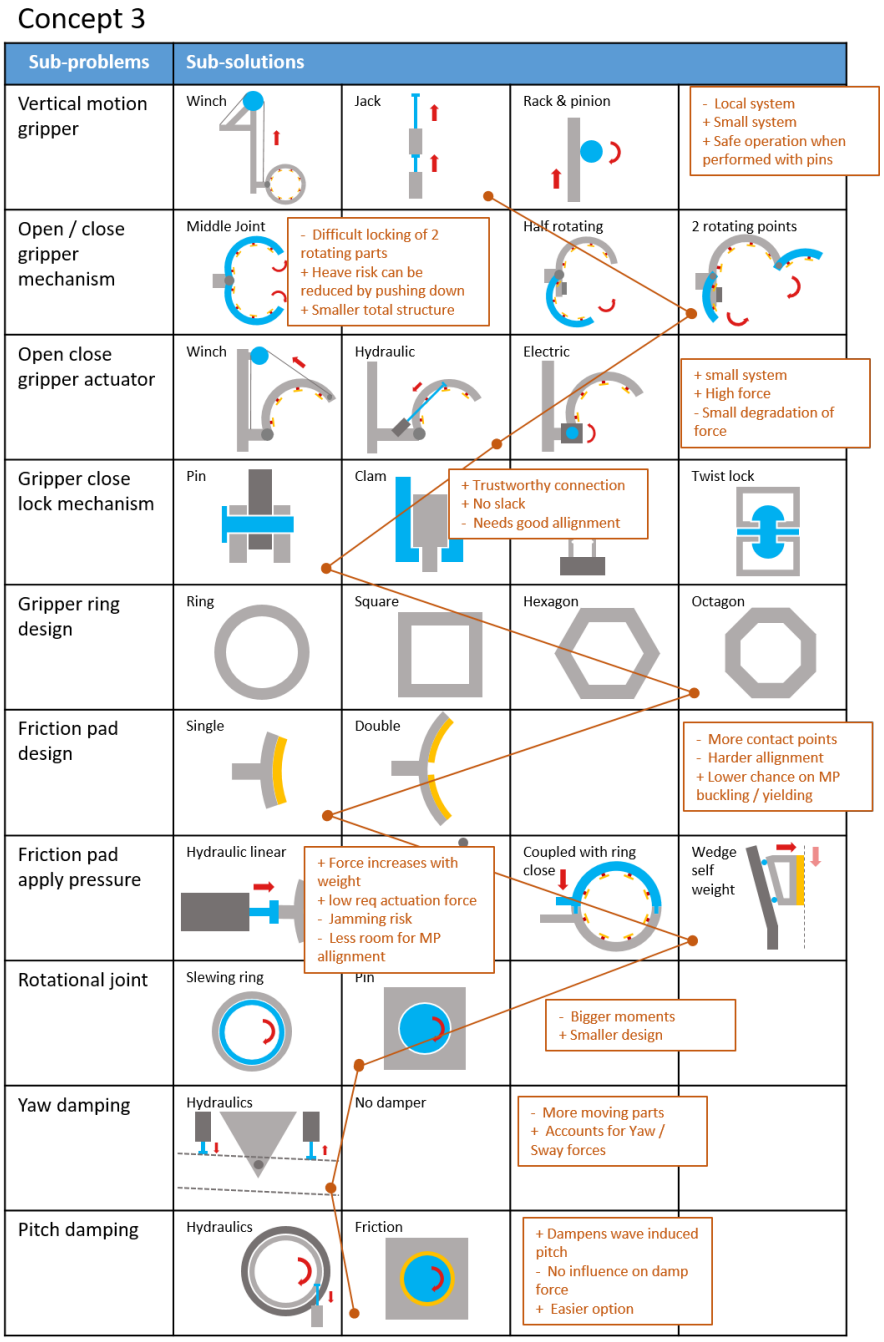

Figure 6.6: The flowchart of the third concept.

The third concept, illustrated in Figure 6.7, shares its global layout with Concept 2 but introduces a fundamentally different, semi-passive mechanism for applying the radial clamping force.

Vertical Translation and Kinematics: The macroscopic movements of the system are identical to Concept 2 (Section 6.2.4). Vertical translation is achieved via the same hydraulic skidding (push-pull) mechanism, and the pile is captured from above using hinged swing-arms that enclose the structural ring.

Pad Pressure Application: The defining trait of Concept 3 is the substitution of direct-acting radial hydraulic cylinders with a self-locking frictional wedge system. To initiate contact, hydraulic cylinders drive the wedge assemblies downwards along the longitudinal axis of the monopile. However, the clamping force is generated passively. As the upending rotation happens, the shifting mass of the monopile begins to pull downward on the friction pads. This downward movement drags the wedges deeper into their housings, proportionally converting the perceived weight of the monopile into an ever-increasing radial clamping force.

Operational Tolerances and Engagement: While the self-locking wedge provides a highly robust, fail-safe clamping force, it introduces kinematic limitations during the engagement phase. Because the initial actuation is longitudinal rather than radial, a large vertical stroke of the driving cylinder translates to only a minimum radial displacement of the friction pad, governed by the shallow angle of the wedge. Consequently, the radial clearance (open state) of the gripper is much smaller compared to Concept 2, demanding significantly higher precision and tighter alignment tolerances when positioning the floating monopile with regard to the friction harness.

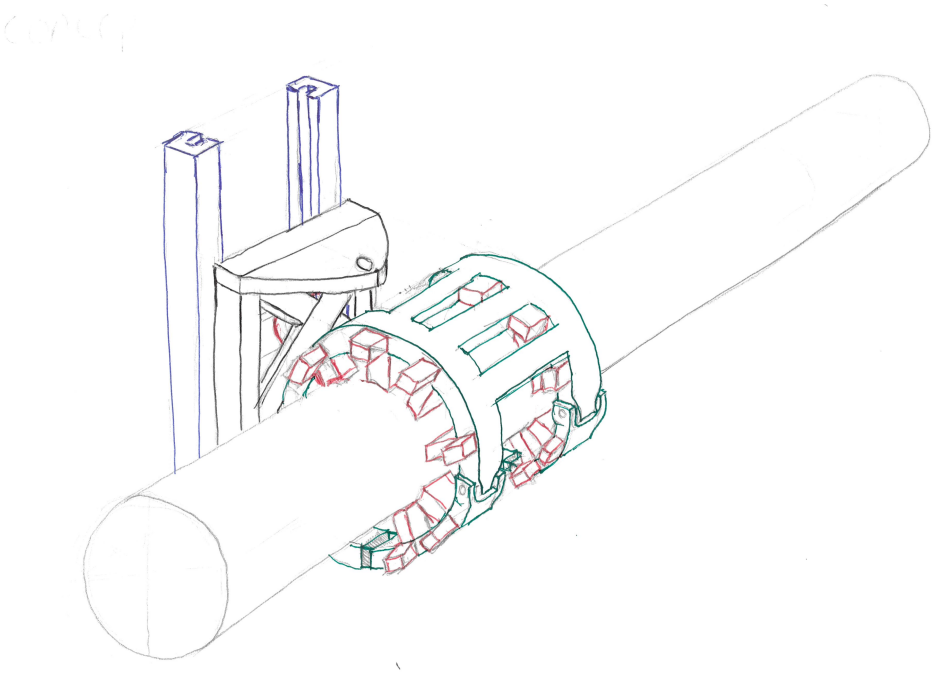

Figure 6.7: 3D sketch of Concept 3, featuring the same skidding and swing-arm design as Concept 2, but utilizing a longitudinally actuated, self-locking wedge mechanism for clamping.

6.3. Multi-Criteria Analysis and Concept Selection

To objectively select the most promising concept for further development, a Multi-Criteria Analysis (MCA) was conducted.

6.3.1. Evaluation Criteria

The MCA evaluates each concept against predefined criteria. Concepts were scored on a scale from 1 (poor performance) to 5 (excellent performance). These scores were multiplied by predefined weighting factors to yield a final weighted score.

The criteria are divided into four main categories, weighted according to their criticality. A comprehensive breakdown of the sub-criteria, individual weightings, and definitions is provided in Appendix E.

- **Operational Efficiency (30%):** Evaluates engagement tolerance, attachment simplicity, and retraction reliability, as the engagement of the floating monopile and the gripper is a crucial and difficult step in this process.
- **Safety & Integrity (30%):** Prioritizes mechanical fail-safes during power loss and symmetrical pressure control to prevent local monopile buckling.
- **System Integration (25%):** Assesses mass efficiency, spatial clearances, vertical stroke requirements, and the system's rotational inertia relative to the JUV.
- **Fabrication (15%):** Evaluates estimated capital costs and manufacturing complexity. This is weighted lowest, as the primary goal is proving kinematic feasibility rather than economic optimization.

6.3.2. Concept Evaluation and Discussion

Rather than detailing every individual score, the following discussion highlights the decisive engineering trade-offs that drove the final selection.

Operational Performance and Tolerances: Concept 2 (Radial Cylinders) significantly outperformed Concept 3 (Wedges) and concept 1 (Sliding) in operational efficiency. Because the wedge mechanism in Concept 3 requires a longitudinal stroke to generate radial clamping, and concept 1 has pressure appliance coupled with its gripper closing, their radial clearances in the 'open' state are significantly smaller. This results in a poor engagement tolerance, requiring highly precise monopile positioning. Furthermore, Concept 3 poses a high risk of jamming during the retraction phase due to the sliding component of the wedge design.

Safety and Load Distribution: The safety category presented the most critical trade-off. Concept 3 scored perfectly in fail-safe reliability, as the payload's own weight passively mechanically locks the system, making it trustworthy with power loss. However, it lacks the ability to actively control load distribution. The independent radial cylinders of Concept 2 allow for active, symmetrical load distribution, which is important to mitigate the risk of local buckling in the thin monopile walls. Concept 2 scores lower on fail-safe reliability as there could be a hydraulic loss of power.

System Integration and Feasibility: Concept 1 (Sliding) was heavily penalized in this category. The total structure has to be substantially bigger to scoop the monopile from underneath. This reduces mass efficiency. The required translational structure, to slide open the upper arm of the gripper negatively impacts the rotational inertia of the system. Concepts 2 and 3 are more compact as they use rotational opening mechanisms.

6.3.3. Results and Final Selection

The assessment was translated into numerical scores, yielding the final weighted results presented in Table 6.1.

Table 6.1: Multi-Criteria Analysis

Criteria	**Weight**	**Concept 1**		**Concept 2**		**Concept 3**	
		Score	Total	Score	Total	Score	Total
1 Operational Efficiency							
1.1 Engagement Tolerance	10%	3	6%	5	10%	2	4%
1.2 Attachment Strategy	10%	3	6%	4	8%	3	6%
1.3 Required energy	5%	3	3%	2	2%	4	4%
1.4 Retraction Ease	5%	4	4%	5	5%	2	2%
subtotal	**30%**		**19%**		**25%**		**16%**
2 Safety & Integrity							
2.1 Fail-safe Reliability	20%	4	16%	2	8%	5	20%
2.2 Pressure Control	10%	2	4%	5	10%	3	6%
subtotal	**30%**		**20%**		**18%**		**26%**
3 System Integration							
3.1 No-go Zone Buffer	5%	5	5%	5	5%	3	3%
3.2 Vertical Compactness	5%	2	2%	4	4%	4	4%
3.3 Mass Efficiency	10%	2	4%	4	8%	3	6%
3.4 Rotational Intertia	5%	2	2%	4	4%	4	4%
subtotal	**25%**		**13%**		**21%**		**17%**
4 Fabrication							
4.1 Manufacturing complexity	5%	4	4%	4	4%	2	2%
4.2 Total costs	10%	5	10%	3	6%	3	6%
subtotal	**15%**		**14%**		**10%**		**8%**
Total	**100%**		**66%**		**74%**		**67%**

As demonstrated in Table 6.1, **Concept 2 (Radial Hydraulics)** emerged as the clear winner with a total weighted score of 74%. Although it scored lower than Concept 3 in passive fail-safe reliability, its superior operational tolerances, retraction ease, and ability to actively control radial pressure distribution make it the safest and most viable solution.

6.4. Functional 3D Model

Following the results of the Multi-Criteria Analysis, Concept 2 was translated into a functional 3D CAD model using Autodesk Inventor, illustrated in Figure 6.8. The objective of this model is to verify its kinematic feasibility.

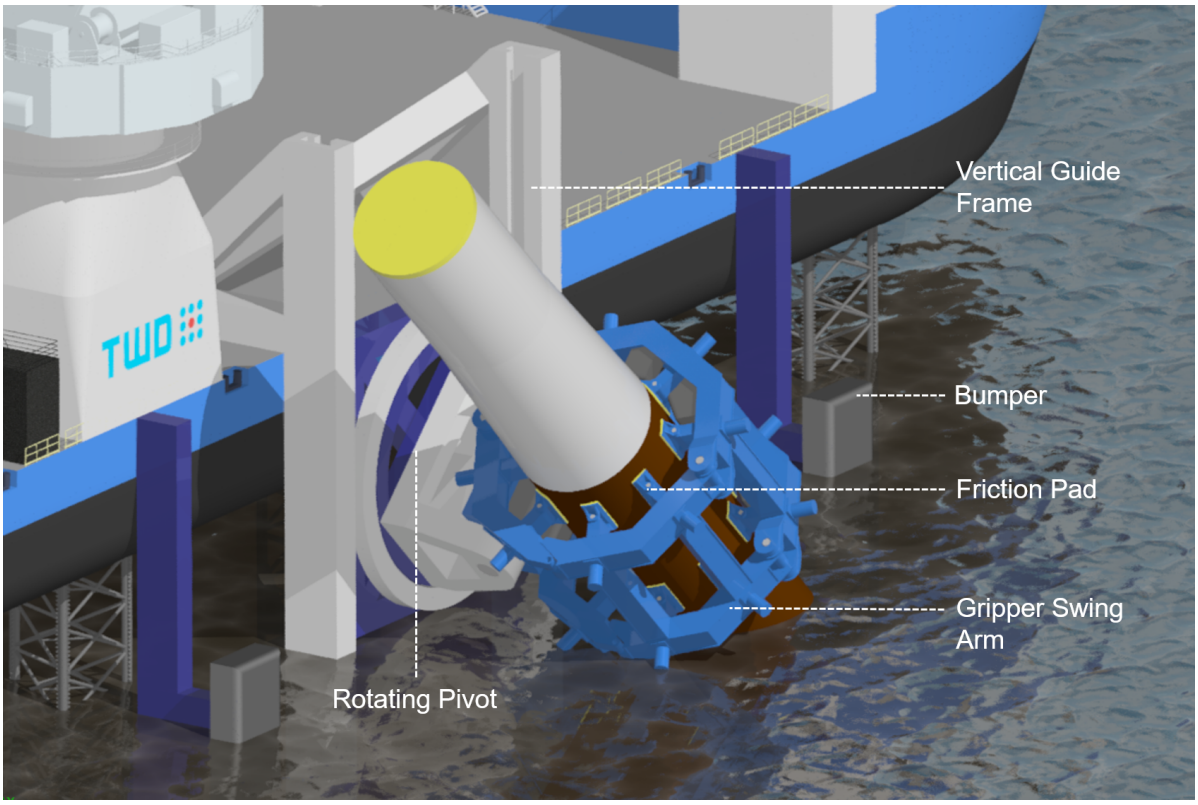

Figure 6.8: Isometric render of the final conceptual design (Concept 2).

The physical dimensions and layout of the model are governed by the local and global parameters determined via the analytical models in previous chapters. These governing variables are integrated into the 3D model as follows:

- **Global Parameters**
  - **Pivot Offset (z_{off}):** The engagement with the monopile is in such a way that the rotational hinge is situated 12 m from the monopile's centre of gravity. This exact placement provides a 1-meter spatial buffer between the gripper frame and the monopile's conical section.
  - **Final Global Pivot Height ($Z_{G,P}$):** The upending sequence concludes at a vertical pivot elevation of 10 m. Coupled with the pivot offset, this specific height minimizes the required frictional clamping force while ensuring sufficient clearance to prevent seabed collisions during rotation.

- **Local Variables**
  - **Pad Configuration:** The structural frame incorporates the analytically optimized 8 x 2 friction pad array (two vertical rings containing eight pads each). These 16 pads are actuated independently via radial hydraulics.
  - **Pad Dimensions ($W_{pad} \times L_{pad}$):** Each individual friction pad measures 1 x 2 m. This contact area, distributed across the 16 points, guarantees that the applied clamping force remains safely below the local buckling and yielding threshold of the thin-walled monopile.

6.5. Full Operational Sequence

The functional design will be explained by detailing the full operational sequence, which is divided into 4 distinct phases:

1. **I. Transport:** the monopile is moved from the storage quay to the installation site
2. **II. Engagement:** The monopile is maneuvered to the gripper and they are safely engaged.
3. **III: Upending:** The craneless ballast assisted upending of the monopile.
4. **IV. Handover:** The monopile is successfully upended and the hydrohammer finishes the installation.

6.5.1. Phase I: Monopile preparation and Transport

The installation starts at the quayside storage yard, where the standard open-ended monopile is prepared for wet transport. Mechanical internal plugs are temporarily installed and sealed at both the top and bottom rims of the structure, as illustrated in Figure 6.9.

Once the monopile is succesfully sealed, the buoyant monopile is launched into the water. two tugboats connect to the monopile, one to the bottom and one to the top. After which the monopile is towed horizontally to the offshore installation site (Figure 6.10).

Figure 6.9: A pile plug being installed to make a monopile buoyant [85].

Figure 6.10: Aerial view of a floating monopile being towed by a tugboat. [20].

6.5.2. Phase II: Gripper Engagement

Phase II transitions the monopile from a freely floating body to a rigidly constrained component. This phase is described across panels (a) through (f) of the phase II engagement storyboard (Figure 6.11).

1. **Vessel Approach and Alignment:** The dual-tug configuration helps to precisely maneuver the floating cylinder laterally against the extended rubber guide bumpers (Figure 6.11a and 6.11b). These bumpers align the pile centerline directly beneath the open gripper centerline.
2. **Heave-Compensated Land-down:** The open gripper assembly is jacked down vertically along the vessel guide rails until the rigid upper cradle of the structural ring makes physical contact with the top section of the monopile shell (Figure A.10b). During this landing step, an active hydraulic heave-compensation system within the jacking cylinders matches the sea-state-induced vertical wave motions of the monopile, preventing loss of contact between the monopile shell and the gripper frame.
3. **Swing-Arm Locking:** With the upper cradle in contact with the MP, the two hinged lower swing-arms are hydraulically actuated to swing inward beneath the lower circumference of the pile (Figure 6.11d). Once fully enclosed, a heavy-duty mechanical locking pin engages at the bottom centerline. This locks the jaws into a closed structural ring.
4. **Friction Pad Engagement:** While the structural ring is locked, the monopile still maintains a slight clearance within the internal circumference of the harness to allow for final alignment. To

overcome this clearance, the 8x2 radial hydraulic cylinders extend outward, driving the 16 independent friction pads into direct contact with the monopile outer layer (Figure 6.11e). The hydraulic pressure is increased until the required clamping force is established.

5. **Bumper retraction:** The bumpers are hydraulically retracted toward the JUV hull (Figure 6.11f). This ensures that the monopile does not clash with the vessel structures when upending.

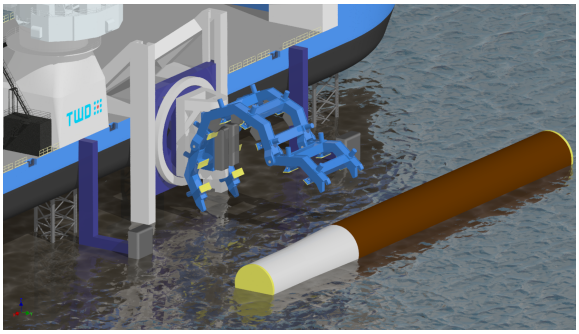

(a) Vessel approach and alignment.

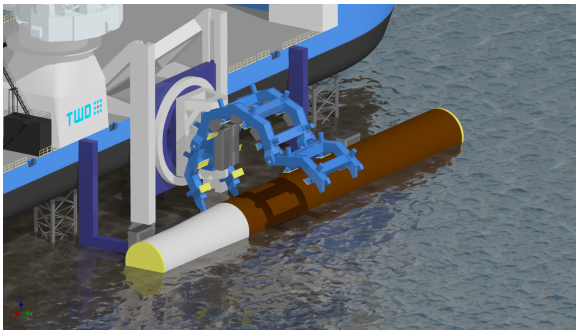

(b) Positioning under the gripper.

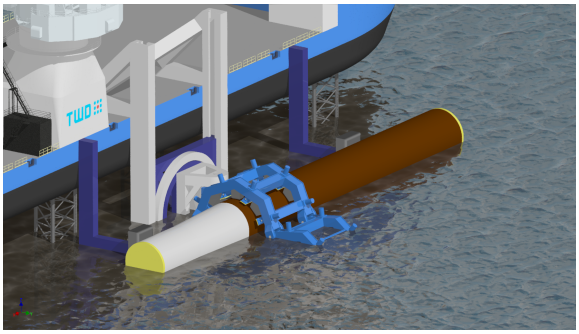

(c) Initial gripper frame contact.

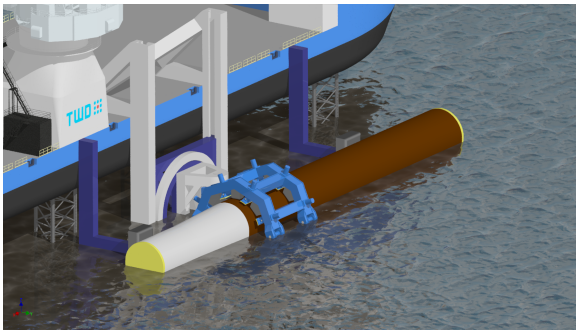

(d) Swing-arms close and lock.

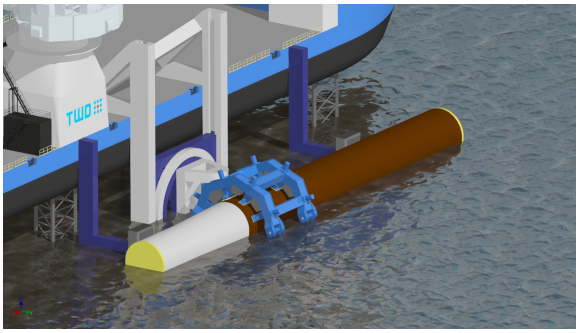

(e) Radial friction pads engage.

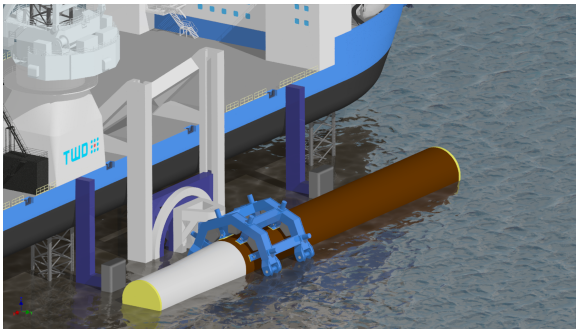

(f) Guide bumpers retract to clear.

Figure 6.11: Phase II (Engagement): The monopile is maneuvered to the gripper and safely engaged.

6.5.3. Phase III: Upending Sequence

The monopile is now rigidly connected to the gripper interface, restricting independent translation. Phase III concerns the physical rotation of the monopile from its horizontal floating state to its final vertical orientation. Steps of this phase are shown in Panels (a) through (c) of Figure 6.12.

The upending sequence begins by initiating the actuation sequence: controlled seawater ballast is pumped into the internal core via a ballast hose connected to the top plug, while the skidding mechanism simultaneously jacks the entire gripper frame vertically upward along the guide rails (Figure 6.12a and 6.12b). The combination of adding the ballast mass and the vertical upwards motion results in rotation of the monopile.

Dynamic out-of-plane motions caused by wave action during this phase are dissipated by the integrated pitch and yaw hydraulic damping systems, preventing it from transferring bending moments into the guide rails.

The monopile reaches an orientation of exactly 90 °, at which point the automated mechanical over-rotation latch drops into place, rigidly locking the pitch hinge and preventing the assembly from drifting toward its natural hydrostatic equilibrium past verticality (Figure 6.12c).

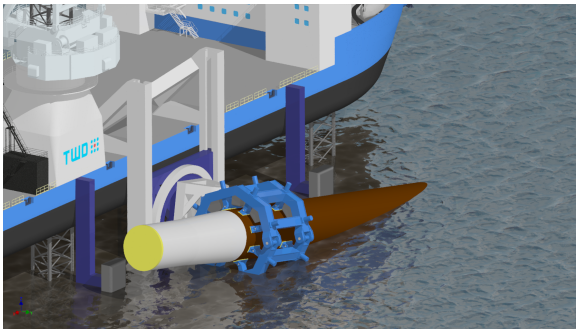

(a) Start ballasting and lift (10°).

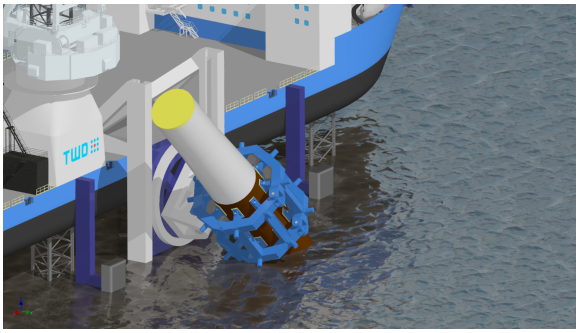

(b) Controlled rotation (45°).

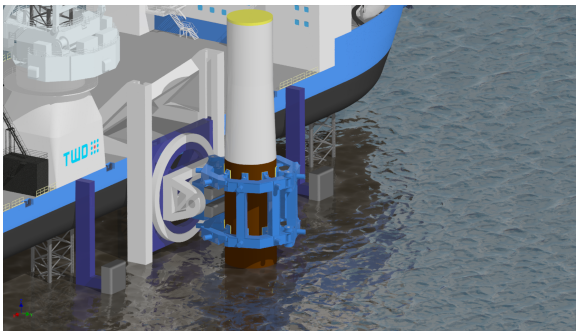

(c) Vertical equilibrium lock (90°).

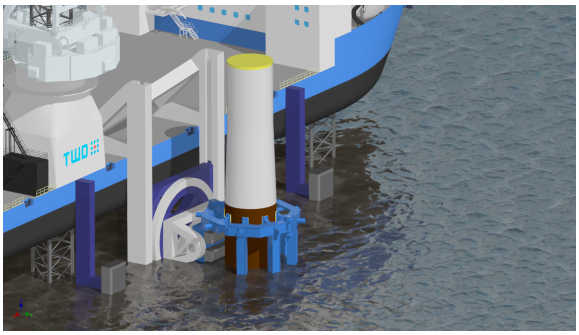

(d) Lowered to stable depth.

Figure 6.12: Phase III and IV: The controlled ballast-assisted upending sequence and lowering to a self-stable embedment depth.

6.5.4. Phase IV: Final Positioning and Piling Operations

The final phase stabilizes the vertical monopile within the seabed soil layer and hands over structural control to standard offshore driving equipment to complete the installation lifecycle.

With the vertical lock engaged, the bottom plug is remotely unlatched and removed. The top plug actively increases the pressure in the top compartment of the monopile to maintain the buoyancy force until later soil friction takes over. The jacking mechanism then reverses direction, jacking the entire vertical assembly downward toward the seabed. The downward motion continues until the monopile penetrates the upper soil and reaches a self-stable embedment depth (Figure 6.12d).

At this depth, the surrounding soil provides sufficient resistance to prevent overturning. This marks the transition from the upending phase to the final installation phase.

At this stage, there is no need for a physical handover to a separate gripping/guiding system. Instead, the functionality of the current gripper changes. The radial hydraulic cylinders are retracted, releasing the friction pads from the monopile surface and clearing the internal space of the gripper.

In the vertical configuration, the overall layout of the proposed gripper is already very similar to conventional monopile grippers used for pile guiding. Although guide rollers are not included in the current design, they can be integrated into the inner circumference of the frame. These rollers would then take over the role of guiding and stabilizing the monopile during the piling operation.

Finally, the JUV crane hoists a traditional offshore hydrohammer from the deck and positions it on top of the monopile (Figure 6.13). Impact driving starts to push the monopile to its final penetration depth, while the tugboats have already departed to retrieve the next monopile, preparing the next installation cycle.

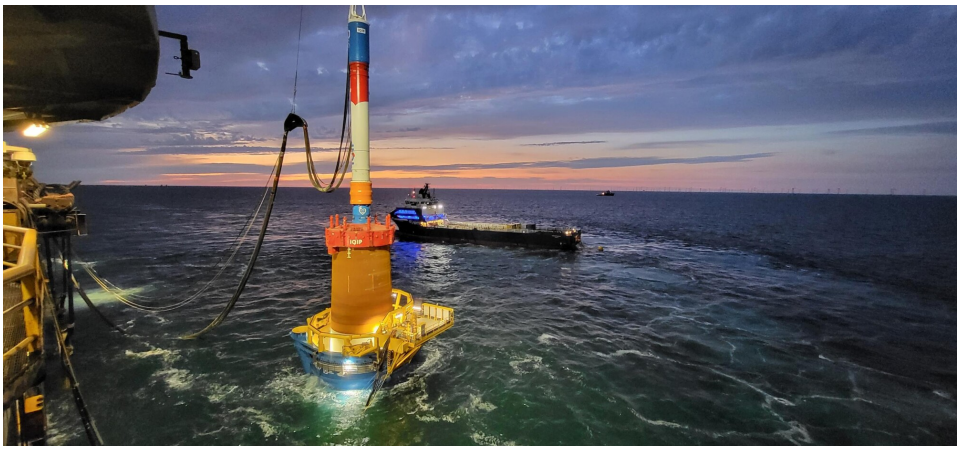

Figure 6.13: A hydrohammer being deployed for monopile driving at sea [86].

6.6. System Actuation and Damping Mechanisms

To provide a complete understanding of the system's mechanics, the functional logic of the actuation and damping systems is defined below. While the global structural frame and the radial cylinders are represented in the 3D model, the hydraulic and damping components are conceptually explained.

6.6.1. Swing-Arm Actuation

The kinematic opening and closing of the gripper frame are governed by hydraulic cylinders acting directly on the hinged swing-arms. This movement is visually detailed in Figure 6.14. The actuation cylinders are mounted on the rigid upper section of the structural ring, next to the hinge points. To create the necessary clearance for engagement, these cylinders retract, swinging the arms outward (Figure 6.14a). Once positioned around the monopile, the cylinders extend to fully enclose the structure (Figure 6.14b).

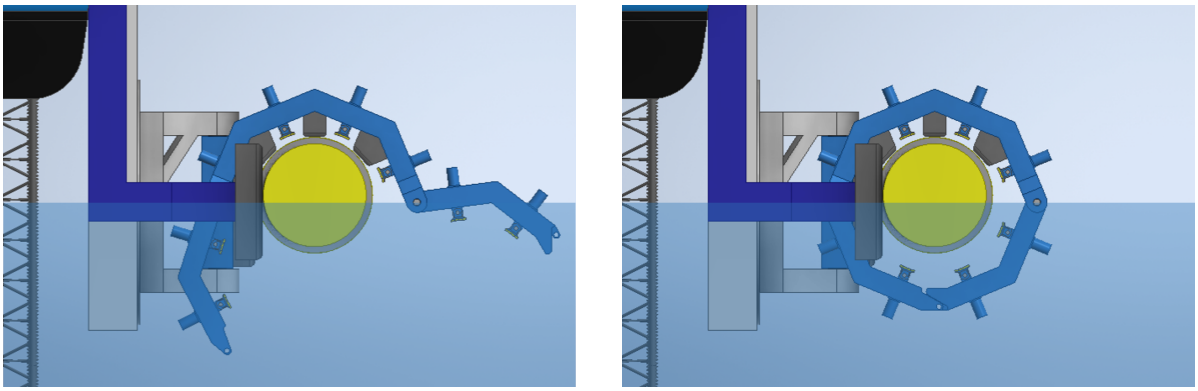

(a) Open/close cylinders retracted: Swing-arms open to provide engagement clearance.

(b) open/close cylinders extended: Swing-arms fully enclose the monopile prior to locking of both arms.

Figure 6.14: Front view visualization of the swing-arm actuation, demonstrating the transition from the open approach state to the enclosed state.

6.6.2. Swing-Arm Locking Mechanism

After the hydraulic positioning cylinders have fully enclosed the swing-arms around the monopile, the frame must be structurally secured before the high-pressure radial clamping force can be applied. This is achieved via a hydraulically actuated locking pin located at the connection of the two swing-arms. Once the arms connect, the pin extends, mechanically interlocking the two halves. This actuation transforms the open, hinged swing-arms into a continuous, rigid structural ring.

6.6.3. Radial Pad Actuation (The Hydraulic Press)

To safely apply the required friction force, sixteen cylinders (8×2), each coupled to a friction pad, independently apply pressure to the monopile surface. During the initial capture phase, the pads are fully retracted to provide the necessary clearance around the monopile, as shown in Figure 6.15a. Once the swing arms are structurally locked, the cylinders actuate radially inward, closing the gap and pressing the friction pads against the monopile wall (Figure 6.15b). This independent actuation stroke ensures a precise and symmetrical pressure distribution across the interface.

Based on the required friction capacity established in Chapter 4, the system must generate a total normal force (F_{total}) of 40,000 kN to safely grip the monopile. This force is distributed equally across the number of independent hydraulic actuators ($n_{cyl} = 16$). The required continuous radial push force per cylinder (F_{cyl}) is calculated as follows:

$$F_{cyl} = \frac{F_{total}}{n_{cyl}} = \frac{40,000 \text{ kN}}{16} = 2,500 \text{ kN} \tag{6.1}$$

While detailed hydraulic circuit design and cylinder sizing remain outside the scope of this conceptual phase, a 2,500 kN capacity (approximately 250 metric tons) is well within the standard operational limits

of commercially available heavy-duty offshore hydraulics. This confirms the mechanical feasibility of the proposed radial layout without requiring novel or experimental actuation technologies.

After the required normal force is reached, the hydraulic cylinders are mechanically locked, for example through a lock-nut or comparable locking mechanism. This ensures that, in the event of hydraulic pressure loss, contact between the friction pads and monopile is maintained, preventing loss of grip and satisfying fail-safe operational criteria.

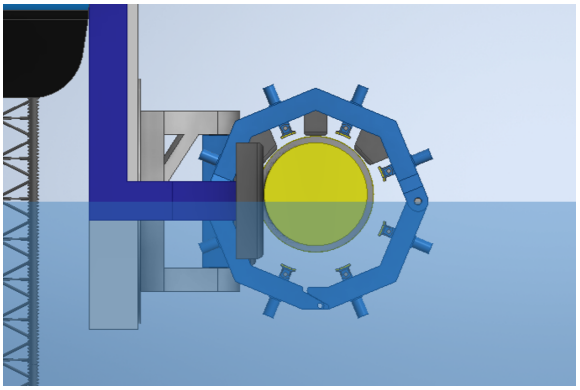

(a) Swing-arms structurally locked with friction pads in the retracted position (clearance state).

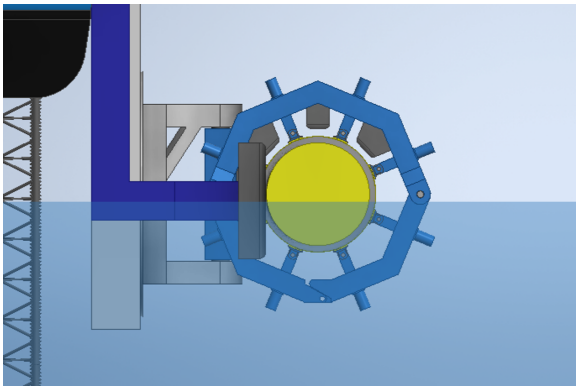

(b) Linear hydraulic cylinders fully extended, engaging the friction pads against the monopile.

Figure 6.15: Front view visualization of the radial pad actuation mechanism, demonstrating the transition from the enclosed state to full frictional clamping.

6.6.4. Guide Bumper Retraction

To help the initial alignment of the floating monopile, the gripper frame is equipped with two guide bumpers. During the approach phase, these bumpers are fully extended to catch the monopile safely into the engagement zone (Figure 6.16a). However, once the monopile is securely clamped and the upending rotation starts, these extended structures risk clashing with the monopile or the vessel structure during upending. To prevent this, the bumpers are hydraulically retracted inward. This transition from the extended to the retracted state is shown in Figure 6.16.

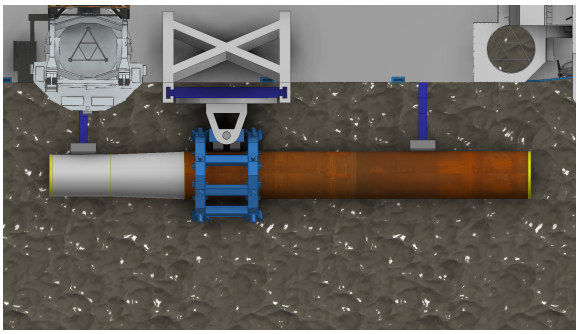

(a) Bumpers fully extended to guide and align the monopile during the initial gripper approach.

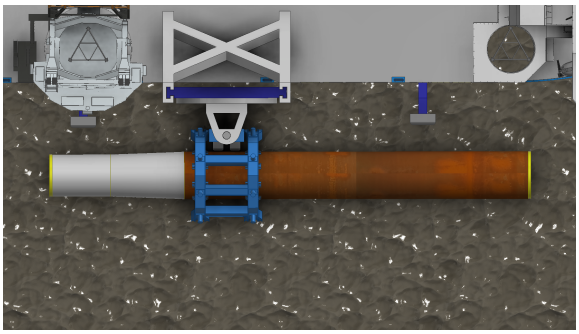

(b) Bumpers hydraulically retracted to provide clearance for the upending rotation.

Figure 6.16: Top view visualization of the bumpers

6.6.5. Vertical Jacking Mechanism

The required vertical translation along the guide rails attached to the vessel is achieved via a hydraulic push-pull skidding mechanism, commonly referred to in the offshore industry as a caterpillar jacking system. Rather than using single, massive cylinders capable of a continuous 10-meter stroke, this system breaks the lifting process into discrete, cyclic steps, as conceptually illustrated in Figure 6.17.

The upward translation follows the following kinematic sequence:

- **Step 1: Base Engagement (Figure 6.17a).** The lower base block of the hydraulic cylinders is mechanically pinned to the vessel's guide rails. The structural frame (blue) is unpinned, resting entirely on the retracted cylinders.
- **Step 2: Actuation Stroke (Figure 6.17b).** The hydraulic cylinders extend. Pushing against the locked base block, this extension physically hoists the entire gripper assembly upwards along the rails.
- **Step 3: Reset and Retraction (Figure 6.17c).** Once the maximum cylinder stroke is reached, secondary locking pins engage to secure the structural frame to the guide rails. The lower cylinder base is then unpinned, and the cylinders retract. This retraction pulls the base block upwards, resetting it into a higher pin-hole to begin the next lifting cycle.

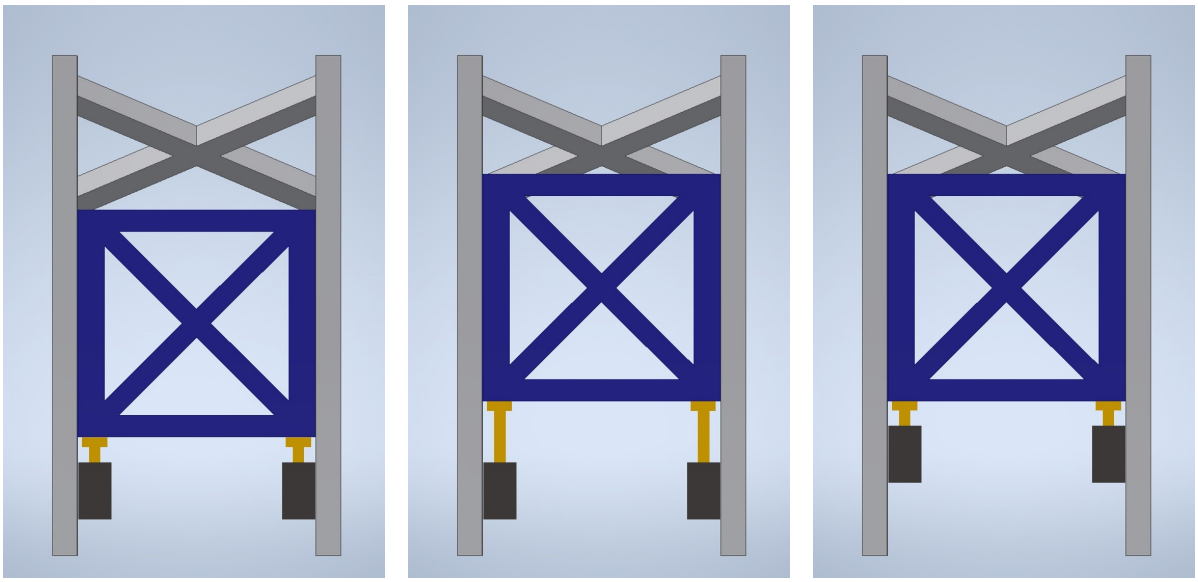

(a) Step 1: Cylinder base locked; cylinders fully retracted.

(b) Step 2: Cylinders extend, pushing the frame upwards.

(c) Step 3: Frame locks to rail; cylinder base unpins and retracts upwards.

Figure 6.17: Conceptual schematic of the step-by-step hydraulic caterpillar jacking sequence used for vertical translation of the gripper frame.

6.6.6. Heave Compensator

During the initial approach and engagement phases, the gripper, connected the to Jack-Up Vessel, remains rigidly elevated above the water level while the floating monopile moves dynamically with the sea state. Attempting to land a completely rigid gripper assembly onto this oscillating structure introduces a high risk of severe impact damage to both the gripper assembly and the thin-walled monopile shell. To eliminate unsafe peak loads, the vertical jacking mechanism is designed with a heave compensator.

Before structural engagement begins, the vertical jacking cylinders transition from a rigid positioning state into a heave state. When the gripper frame makes contact with the floating monopile, the system allows the frame to stroke vertically in tandem with the wave-induced motions rather than resisting them.

The mechanism dampens oscillations and suppresses peak impact forces. This provides a stable connection that allows the swing-arms to safely close and lock around the pile.

6.6.7. Pitch Damping

As established in Chapter 4, the upending system is susceptible to resonance with wave frequencies, resulting in spikes in structural loading. To mitigate this effect, a unidirectional damper is incorporated, as conceptually shown in figure 6.18. This damper resists the surfacing motion by incorporating a wedge-type mechanism, thereby preventing rotation back toward the 0-degree state. As a result, the monopile is constrained to rotate only in the desired direction, effectively damping out oscillations.

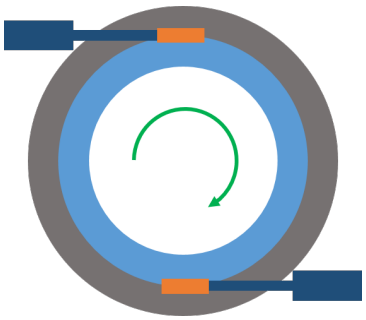

Figure 6.18: A conceptual unidirectional pitch damper placed on the pitch rotation ring, resisting rotation the opposite direction of the green arrow with a wedge.

6.6.8. Yaw Damping

To prevent sway waves from inducing extreme bending moments into the vertical guide rails, the gripper assembly features a dedicated yaw rotational mechanism. As illustrated in Figure 6.19, this joint allows the gripper frame to passively rotate slightly out-of-plane. To manage this motion, hydraulic dampers are placed between the stationary white yaw hinge and the pivoting gripper frame, safely dissipating the kinetic energy of the transverse (wave) loads. To prevent mechanical clashing with the vessel, this yaw articulation is physically constrained by hard stops to a maximum rotation of $\pm 5^{\circ}$ from the gripper centerline.

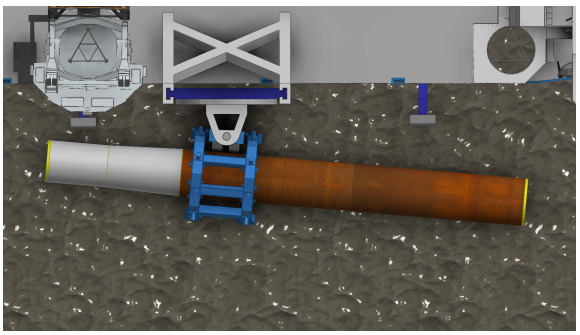

(a) Gripper assembly passively rotating to accommodate for sway (yawing left).

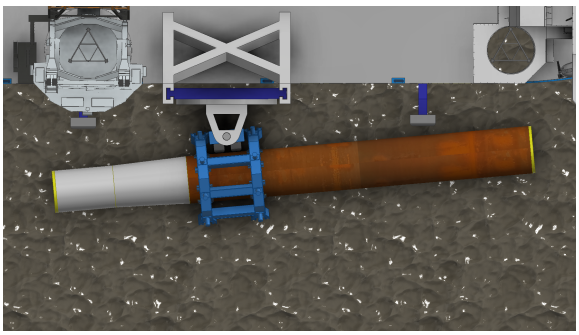

(b) Gripper assembly passively rotating to accommodate for sway (yawing right).

Figure 6.19: Top view visualization of the yaw damping mechanism, demonstrating the gripper frame's ability to rotate out-of-plane to prevent extreme bending moments transferring into the vessel guide rails.

6.6.9. 90-Degree Lock

As determined in the global upending simulations (Chapter 4), the final natural equilibrium position of the ballasted monopile is at approximately 95 degrees. However, the monopile needs to be installed with a near-perfect vertical (90-degree) orientation. To prevent over-rotation, a mechanical locking latch is integrated into the design. Once the monopile pitches to exactly 90 degrees, a lock comes into place, preventing the gripper assembly with the monopile from rotating further.

6.7. Cost Estimation and Commercial Viability

While the main objective of this thesis is to prove the kinematic and structural feasibility of the craneless upending system, its value is elevated by assessing the commercial viability. This section provides a comparative operational expenditure (OPEX) estimate to determine the break-even capital allowance for the proposed gripper assembly.

6.7.1. Base Case Definition

To establish a benchmark, the proposed method is evaluated against a cost-efficient traditional monopile installation strategy. Based on a comprehensive evaluation of nine transport and installation (T&I) methods by Tjaberings et al. [87], the most cost-effective standard method for a reference wind farm of 67 monopiles utilizes a single Heavy Lift Vessel (HLV). In this base case, the HLV acts as both the transport and installation vessel, shuttling back and forth between the storage quay and the offshore site. For a 67-monopile project, this traditional method requires an estimated 130 to 140 operational days; for this comparative analysis, an average of 135 days is assumed.

To quantify the costs, representative 2025 vessel day rates are sourced from a 2025 offshore cost study by TNO [9], summarized in Table 6.2.

Table 6.2: Vessel day rates assumed for OPEX calculations [9].

Vessel Type	Example / Class	Day Rate
Heavy Lift Vessel (HLV)	Bokalift 2	€400,000 / day
Jack-Up Vessel (JUV)	Aeolus	€250,000 / day
Tugboat	5000 bhp	€15,000 / day

In the base case, an HLV class similar to the *Bokalift 2* is used, as its 4,000-tonne crane capacity [88] comfortably accommodates the 2,170-tonne reference monopile. The total installation OPEX for the base case is calculated as:

$$\text{OPEX}_{\text{base}} = 135 \text{ days} \times €400,000/\text{day} = €54.0 \text{ million} \tag{6.2}$$

6.7.2. Proposed Concept Logistics and Cost

By utilizing buoyancy and the proposed gripper assembly instead of a heavy lift crane for upending, the vessel used for installation can be a standard Jack-Up Vessel (JUV). An example vessel such as the *Aeolus* possesses a crane capacity of only 1,600 tonnes [89], rendering it incapable of traditional lifting for this project. However, it is structurally sufficient to serve as the stationary jacking platform for the friction gripper.

Furthermore, the proposed method utilizes two tugboats for the wet-towing and presentation of the monopiles. Because the tugboats act as a continuous supply line, the JUV never has to shuttle back to the quay. By eliminating quay loading and transit times for the installation vessel, the total operation time is conservatively estimated to be reduced by 20 days, yielding a 115-day installation campaign.

Assuming the 115-day timeline, the daily operational use consists of one JUV and two tugboats. The OPEX for the proposed method is calculated as:

$$\text{OPEX}_{\text{proposed}} = 115 \text{ days} \times (€250,000 + 2 \times €15,000) = €32.2 \text{ million} \tag{6.3}$$

Note on Operational Limits: It must be acknowledged that wet-towing floating monopiles introduces a higher sensitivity to severe sea states compared to transporting them on the deck of an HLV. Therefore, while the logistical time is reduced to 115 days, realizing this timeline in practice will depend heavily on identifying adequate weather windows.

6.7.3. Break-Even Allowance and Strategic Value

Comparing the two strategies reveals a direct OPEX saving of **€21.8 million** in favor of the craneless upending using a JUV method.

This number establishes the break-even capital expenditure (CAPEX) allowance for the gripper design. Even in the highly conservative scenario where the custom gripper assembly is entirely written off after a single 67-monopile project, the system remains commercially viable as long as the engineering and fabrication costs of the gripper do not exceed €21.8 million. That number does not even consider that traditional installation equipment does not have to be fabricated.

Beyond direct cost savings, the proposed method holds significant strategic value. Recent market forecasts indicate that the availability of Heavy Lift Vessels will be severely constrained in the near future due to the escalating scale of offshore wind components [8]. By decoupling the installation of XXL monopiles from HLV availability, the proposed friction-gripper concept mitigates a critical supply chain bottleneck for future wind farm developers.

7

Concluding Remarks and Recommendations

7.1. Conclusion

This research investigated the theoretical and mechanical feasibility of a craneless, buoyancy-assisted upending method for XXL monopiles. Based on the kinematic, hydrodynamic, and structural analyses conducted in this study, it is concluded that a friction-based gripper system is a theoretically and mechanically feasible solution to safely upend heavy monopiles without the need for a Heavy Lift Vessel.

7.1.1. Global Upending Dynamics

The global dynamic analysis established that the monopile's rotation can be safely controlled through a coordinated sequence of vertical jacking ($Z_{G,P}$) and active seawater ballasting (z_{fill}). The parametric optimization concluded that a pivot offset (z_{off}) of 12 m, combined with a final pivot height of 10 m and a final ballast volume of 1,803 m^3, provides a stable rotational trajectory that successfully avoids collision with the -50 m seabed. This buoyancy-assisted approach effectively reduces the perceived weight of the monopile at the fully vertical 90-degree state from its dry mass of 2,170 tonnes down to an effective load of just 950 tonnes. Consequently, the gripper system is subjected to a peak longitudinal shear force of 9,500 kN, which dictates the required friction force.

7.1.2. Friction Interface and Structural Demand

To safely transfer this 9,500 kN shear load purely through wet friction, without causing local buckling or plastic yielding of the thin-walled monopile shell, a massive and uniformly distributed normal force is required. Supported by empirical data retrieved from physical friction testing of the polymer-steel interface at the TWD laboratory, it is concluded that the system must generate a total normal clamping force of 40,000 kN to prevent slip. To safely distribute this extreme pressure, the local gripper interface must consist of a 16-pad configuration (arranged in two rings of 8), with each polymer friction pad measuring 2.0 m by 1.0 m.

7.1.3. The Mechanical Concept

To translate these requirements into a physical machine, the Radial Hydraulic Gripper was selected as the optimal functional concept. This design utilizes 16 independent hydraulic cylinders, each delivering 2,500 kN of radial push force, which ensures a precise and symmetrical pressure distribution across the monopile shell. The system incorporates mechanical lock-nuts on the cylinders, providing fail-safe reliability that maintains the frictional grip even in the event of total hydraulic pressure loss.

7.1.4. Strategic and Commercial Viability

Beyond structural feasibility, the proposed concept demonstrates high commercial and strategic viability. By shifting the installation logistics from a scarce, high-cost Heavy Lift Vessel (HLV) to a Jack-Up Vessel (JUV) supported by a tugboat wet-towing continuous supply line, the installation timeline is shortened. For a reference 67-monopile wind farm, the proposed installation method yields an estimated operational expenditure (OPEX) saving of €21.8 million. This OPEX reduction establishes a highly favorable break-even capital allowance for the fabrication of the gripper assembly. More importantly, this method strategically decouples XXL monopile installation from the constrained HLV supply chain, mitigating a critical industry bottleneck.

7.2. Discussion

While the numerical and analytical models presented in this thesis demonstrate the feasibility of the craneless upending concept, the development of the functional concept relied on several foundational assumptions and simplifications. These assumptions are critically evaluated below.

7.2.1. Kinematic and Hydrodynamic Boundaries

The operation presented in the global upending dynamics (Chapter 4) was modeled as a two-dimensional planar motion, assuming a perfectly rigid Jack-Up Vessel (JUV) and infinitely stiff gripper structure. In physical offshore operations, however, the peak 14,200 kN structural load demand (which was assumed to be fully absorbed by the gripper structure) will induce elastic deflection in the gripper structure. This could introduce out-of-plane motions (sway and yaw) that were mathematically restrained in the current model.

Furthermore, the evaluation of wave kinematics was truncated at the Still Water Level (SWL) using Linear Airy theory. By omitting the wave crest kinematics in the splash zone, the model neglects the wave slamming forces that occur as the large-diameter monopile breaches the water surface. Additionally, the environmental loads were modeled using a single sinusoidal wave, whereas physical sea states consist of an irregular wave spectrum. Consequently, while the 9,500 kN shear load and 14,200 kN structural load serve as a reliable baseline, the true peak operational loads may be higher than this.

7.2.2. Local Interface and Structural Simplifications

To establish the 8×2 friction pad configuration, the Sizing Tool in Chapter 5 intentionally used conservative analytical filters. The local buckling check (Roark's formulas) relied on a 2D disc assumption, isolating a 1-meter horizontal slice of the monopile. This entirely neglects the 3D structural and rotational stiffness provided by the undisturbed steel above and below the gripper. Conversely, the global buckling check (DNV guidelines) suffered from a "smearing" limitation, assuming a mathematically perfect cylinder and a perfectly uniform 360-degree load distribution, remaining analytically blind to the discrete patches of applied force.

While these simplifications, combined with the assumption of an infinitely narrow line load, ensured a conservative design margin, they leave a blind spot regarding multi-axial stress interactions. During the physical upending process, the monopile is subjected to a massive global bending moment from its own overhanging weight, coupled simultaneously with the local radial compression from the gripper. The analytical formulas used in this conceptual phase cannot accurately capture the complex stress concentrations where these global and local forces interact, particularly at the edges of the friction pads.

7.2.3. Tribological Limits and Actuation

The requirement for a 40,000 kN total clamping force is supported by empirical friction data retrieved from laboratory testing, which provides a high degree of confidence in the static holding capacity of the steel-elastomer interface. Because the scope of this functional concept assumes rigid hydraulic locking and a constant normal force, it does not fully account for the creep of the friction pads and the potential loss of clamping pressure over the hours-long upending sequence.

7.3. Recommendations for Future Work

This thesis successfully establishes a mathematically defensible and functional baseline for a crane-less, friction-based upending method. To progress this concept from the functional design phase into detailed engineering and fabrication, the following actions are recommended for future research and development:

7.3.1. Advanced Dynamic and Hydrodynamic Modeling

To accurately quantify the peak operational loads, it is recommended to upgrade the current 2D analytical model to a fully 3D multi-body dynamic simulation (using OrcaFlex or similar industry-standard software). This advanced simulation should consider the impact of out-of-plane motions on the gripper structure. Furthermore, the hydrodynamic environment should be modeled using an irregular wave spectrum, alongside wave slamming forces during the monopile's transition through the water surface.

7.3.2. Non-Linear Finite Element Analysis (FEM)

To resolve the analytical blind spots of the 2D structural simplifications, a comprehensive 3D non-linear Finite Element Method (FEM) analysis is required. This model must simulate the geometry of the proposed 8×2 friction pad interface. The main objective of this FEM study should be to investigate the multi-axial stress interactions, specifically, the structural response of the thin-walled monopile shell when subjected to the massive global bending moment simultaneously with the 40,000 kN local radial compression.

7.3.3. Steel-Polymer Interface Considerations

While the static friction coefficient has been empirically validated through laboratory testing, the long-term endurance of the steel-polymer interface under cyclic loading requires further physical investigation. Moreover, the hydraulic actuation system must be engineered to actively compensate for the anticipated creep.

7.3.4. Adaptable Design

The current design is made for a single monopile size, while in reality monopiles within one wind farm already vary in diameter and length due to site-specific conditions. This means the current concept is not directly applicable in practice. To make the system usable in real operations, the gripper design should be adaptable to a range of monopile diameters. This can be achieved by introducing adjustable or modular components that allow the system to maintain proper contact across different geometries. Implementing this adaptability is essential for moving the concept from a single design case to a practical installation solution.

7.3.5. Detailed Mechanical Design

As this thesis successfully established the functional concept and spatial layout of the Radial Hydraulic Gripper, the next phase of development is detailed engineering. It is recommended to perform a comprehensive structural sizing of the gripper assembly, determining the exact steel plate thicknesses, weld dimensions, and bolted connections required for the gripper ring structure and jacking frame to survive the loads acting on the system. Furthermore, a detailed commercial component specification must be executed. While the conceptual actuation logic has been defined, future work must properly size and select the off-the-shelf components required to drive the system.

7.3.6. Integration of a Piling Guide

In standard offshore installation sequences, once a monopile is upended, it is typically transferred from the upending hinge to a dedicated piling gripper attached to the vessel to ensure verticality during seabed driving. The current functional concept of the Radial Hydraulic Gripper is only designed for the upending maneuver and does not currently consider the piling afterwards. Future research should investigate the integration of a piling guide directly into the upending gripper assembly.

AI Statement

For this thesis, I have used Generative AI to:

- Obtain inspiration for the overall structure of the report
- Improve the grammar, style, layout, and/or spelling of the text
- Implement mathematical models into code and/or produce code to process results.

In all cases I have reviewed and corrected the work and remain fully responsible for the content of the report.

References

[1] Wind and water works, “Dutch Offshore Wind Innovation Guide 2025,” Tech. Rep., 2025.

[2] *Decode offshore wind engineering challenges at every stage | DHI Reservoir - Drops of knowledge*. [Online]. Available: https://blog.dhigroup.com/decode-offshore-wind-engineering-challenges-at-every-stage/.

[3] Empire Engineering, “The Empire Engineering Guide to Offshore Wind Foundations Challenges and opportunities in designing and developing offshore wind foundations both now and in the future,” Tech. Rep., 2023.

[4] R. Gupta, “Behaviour of monopile under combined cyclic load,” 2020.

[5] J. Emblemsvåg, “Rethinking the “Levelized Cost of Energy”: A critical review and evaluation of the concept,” *Energy Research & Social Science*, vol. 119, p. 103 897, Jan. 2025, ISSN: 2214-6296. DOI: 10.1016/J.ERSS.2024.103897. [Online]. Available: https://www-sciencedirect-com.tudelft.idm.oclc.org/science/article/pii/S2214629624004882.

[6] B. van Wuijckhuijse, Y. Volkerts, E. radcliff, and C. Lemmens, “Buoyancy-Assisted Monopile Installation,” Tech. Rep., 2024.

[7] Topsector Energie, *Silent Installation of MonoPiLEs IIB*, 2021. [Online]. Available: https://projecten.topsectorenergie.nl/projecten/silent-installation-of-monopiles-iib-37016.

[8] T. Sahin et al., “Global Supply Chain Study - Market sizing,” Tech. Rep., Apr. 2024.

[9] S. Mancini, “Offshore Wind Farm Decommissioning Cost Estimates Simulating removal and transport of the subsystems of a hypothetical offshore wind farm site representative for the Dutch Roadmap 21GW,” Tech. Rep., 2025. [Online]. Available: www.tno.nl.

[10] Boskalis, *Boskalis’ Heavy Transport Vessels Accept the Monopile Transport Challenge – Heavy Lift News*. [Online]. Available: https://www.heavyliftnews.com/boskalis-heavy-transport-vessels-accept-the-monopile-transport-challenge/.

[11] Barber. Samuel, *Wagenborg awarded monopile contract | News | Heavy Lift & Project Forwarding International*, Mar. 2023. [Online]. Available: https://www.heavyliftpfi.com/sectors/wagenborg-awarded-monopile-contract/22243.article.

[12] SWZ Maritime, *In pics: Boskalis installs largest US wind farm foundation*, 2024. [Online]. Available: https://swzmaritime.nl/news/2024/07/03/in-pics-boskalis-installs-largest-us-wind-farm-foundation/.

[13] Alewijnse, *Boskalis Bokalift 2 | Alewijnse*, 2024. [Online]. Available: https://www.alewijnse.nl/referenties/boskalis-bokalift-2.

[14] LEANWIND, “D3.2-Key design parameters and criteria related to installation and maintenance vessels design; their layouts, crane operations and access systems,” Tech. Rep., 2013.

[15] C. K. van Lynden, I. van Winsen, C. N. Westland, and A. A. Kana, “OFFSHORE WIND INSTALLATION VESSELS - GENERATING INSIGHT ABOUT THE DRIVING FACTORS BEHIND THE FUTURE DESIGN,” *Transactions of the Royal Institution of Naval Architects Part A: International Journal of Maritime Engineering*, vol. 164, no. 2 A, pp. 221–236, Apr. 2022, ISSN: 17400716. DOI: 10.5750/ijme.v164iA2.1175.

[16] N. Kajastie, *First monopile installed for Dogger Bank offshore wind farm | Ground Engineering*, Jul. 2022. [Online]. Available: https://www.geplus.co.uk/news/first-monopile-installed-for-dogger-bank-offshore-wind-farm-29-07-2022/.

[17] D. Foxwell, *New-generation grippers grapple with DP vessel requirements*, Feb. 2020. [Online]. Available: https://www.rivieramm.com/news-content-hub/news-content-hub/new-generation-grippers-grapple-with-dp-vessel-requirements-57862.

[18] *Foundation installation campaign begins on Dogger Bank B - Dogger Bank Wind Farm*, May 2024. [Online]. Available: https://doggerbank.com/construction/foundation-installation-campaign-begins-on-dogger-bank-b/.

[19] van Oord, *Major upgrade for Van Oord's heavy lift installation vessel Svanen | Van Oord*, Dec. 2023. [Online]. Available: https://www.vanoord.com/en/updates/major-upgrade-van-oords-heavy-lift-installation-vessel-svanen/.

[20] University of Srathclyde Glasgow, *The Practicality and Challenges of Using XL Monopiles for Offshore Wind Turbine Substructures: Technical Feasability*, 2015. [Online]. Available: https://www.esru.strath.ac.uk/EandE/Web_sites/14-15/XL_Monopiles/technical.html.

[21] van Oord, *Van Oord installs first monopile at Baltic Eagle offshore wind farm | Van Oord*, Apr. 2023. [Online]. Available: https://www.vanoord.com/en/updates/van-oord-installs-first-monopile-baltic-eagle-offshore-wind-farm/.

[22] van Oord, *Van Oord heavy lift installation vessel Svanen takes on another Baltic project | Van Oord*, Dec. 2018. [Online]. Available: https://www.vanoord.com/en/updates/van-oord-heavy-lift-installation-vessel-svanen-takes-another-baltic-project/.

[23] van Oord, *Van Oord's heavy lift installation vessel Svanen has arrived at Kriegers Flak wind farm | Van Oord*, May 2020. [Online]. Available: https://www.vanoord.com/en/updates/van-oords-heavy-lift-installation-vessel-svanen-has-arrived-kriegers-flak-wind-farm/.

[24] *World's Largest Offshore Wind Farm | Fugro*. [Online]. Available: https://www.fugro.com/expertise/case-studies/development-worlds-largest-offshore-wind-farm-fugro.

[25] D. Raaijman, "Buoyancy based upending of a monopile," Tech. Rep., 2024. [Online]. Available: http://repository.tudelft.nl/..

[26] M. van der Slot, "Classification and Evaluation of Gripping Mechanisms for Offshore Splash-Zone Handling," Tech. Rep., 2025.

[27] S. Raval and B. Patel, "A Review on Grasping Principle and Robotic Grippers," *International Journal of Engineering Development and Research*, vol. 4, p. 483, 2016, ISSN: 2321-9939. [Online]. Available: www.ijedr.org.

[28] L. Chen and L. Qian, *Role of interfacial water in adhesion, friction, and wear—A critical review*, Feb. 2020. DOI: 10.1007/s40544-020-0425-4.

[29] P. Dzitac and A. Md Mazid, "A method to control grip force and slippage for robotic object grasping and manipulation," in *2012 20th Mediterranean Conference on Control and Automation, MED 2012 - Conference Proceedings*, 2012, pp. 116–121, ISBN: 9781467325318. DOI: 10.1109/MED.2012.6265624.

[30] IQIP, *External Lifting Tool*. [Online]. Available: https://iqip.com/products/lifting-equipment/external-lifting-tool/.

[31] J. C. Trinkle, "A Quantitative test for form closure grasps," in *IEEE International Conference on Intelligent Robots and Systems*, vol. 3, Institute of Electrical and Electronics Engineers Inc., 1992, pp. 1670–1677, ISBN: 0780307372. DOI: 10.1109/IROS.1992.594246.

[32] M. Cabaleiro, B. Conde, C. González-Gaya, and B. Barros, *Removable, Reconfigurable, and Sustainable Steel Structures: A State-of-the-Art Review of Clamp-Based Steel Connections*, May 2023. DOI: 10.3390/su15107808.

[33] KENC, *Flange Monopile Upending Tool*. [Online]. Available: https://kenc.nl/equipment/monopile-upending-tool/.

[34] J. Shintake, V. Cacucciolo, D. Floreano, and H. Shea, *Soft Robotic Grippers*, Jul. 2018. DOI: 10.1002/adma.201707035.

[35] F. Dietrich and A. Müller, "Upscaling of soft material grippers to heavy duty applications in handling and assembly," *CIRP Annals*, vol. 71, no. 1, pp. 33–36, Jan. 2022, ISSN: 17260604. DOI: 10.1016/j.cirp.2022.04.042.

[36] C. Blanes, M. Mellado, C. Ortiz, and A. Valera, *Tecnologías en garras robotizadas para operaciones de coger y dejar productos hortofrutícolas frescos*, 2011. DOI: 10.5424/sjar/20110904-501-10.

[37] Z. Wang, Z. Li, T. Wang, and B. Zhang, “Study on clamping mechanism of internal and external variable diameter lifting tool for offshore foundation pile,” *Machines*, vol. 9, no. 1, pp. 1–19, Jan. 2021, ISSN: 20751702. DOI: 10.3390/machines9010019.

[38] B. Zhang, H. Chen, T. Wang, and Z. Wang, “Design and experiment of a lifting tool for hoisting offshore Single-Pile foundations,” *Machines*, vol. 9, no. 2, pp. 1–13, Feb. 2021, ISSN: 20751702. DOI: 10.3390/machines9020029.

[39] P. Ditsche and A. P. Summers, *Aquatic versus terrestrial attachment: Water makes a difference*, 2014. DOI: 10.3762/bjnano.5.252.

[40] Jizhong Xiao, Bing Li, Kenshin Ushiroda, and Qiang Song, *Rise rover: a wall climbing robot with high reliability and load carrying capacity*. IEEE, 2015, ISBN: 9781467396752.

[41] G. Mantriota, “Theoretical model of the grasp with vacuum gripper,” *Mechanism and Machine Theory*, vol. 42, no. 1, pp. 2–17, Jan. 2007, ISSN: 0094114X. DOI: 10.1016/j.mechmachtheory.2006.03.003.

[42] P. Ditsche and A. Summers, “Learning from Northern clingfish (Gobiesox maeandricus): Bioinspired suction cups attach to rough surfaces,” *Philosophical Transactions of the Royal Society B: Biological Sciences*, vol. 374, no. 1784, Oct. 2019, ISSN: 14712970. DOI: 10.1098/rstb.2019.0204.

[43] Direct Industry, *Standard vacuum tilter for precast concrete and tunneling*. [Online]. Available: https://pdf.directindustry.com/pdf/aerolift-industrials-bv/t-series-standard-vacuum-tilters-precast-concrete-tunnelling/115869-1112021.html?.

[44] G. Loianno et al., “Localization, Grasping, and Transportation of Magnetic Objects by a Team of MAVs in Challenging Desert-Like Environments,” *IEEE Robotics and Automation Letters*, vol. 3, no. 3, pp. 1576–1583, Jul. 2018, ISSN: 23773766. DOI: 10.1109/LRA.2018.2800121.

[45] J. Fan et al., “An underwater robot with self-adaption mechanism for cleaning steel pipes with variable diameters,” *Industrial Robot*, vol. 45, no. 2, pp. 193–205, Apr. 2018, ISSN: 0143991X. DOI: 10.1108/IR-09-2017-0168.

[46] HVR MAG, *lifting magnets*, 2025. [Online]. Available: https://www.hvrmagnet.com/lifting-magnets.html?utm_source=bing&utm_medium=cpc&utm_campaign=566553817&utm_term=electromagnetic%20lifting%20device&msclkid=a3c5e9b1174c1d97070a80bd6623f059.

[47] P. Glick, S. A. Suresh, D. Ruffatto, M. Cutkosky, M. T. Tolley, and A. Parness, “A Soft Robotic Gripper with Gecko-Inspired Adhesive,” *IEEE Robotics and Automation Letters*, vol. 3, no. 2, pp. 903–910, Apr. 2018, ISSN: 23773766. DOI: 10.1109/LRA.2018.2792688.

[48] A. Y. Stark, T. W. Sullivan, and P. H. Niewiarowski, “The effect of surface water and wetting on gecko adhesion,” *Journal of Experimental Biology*, vol. 215, no. 17, pp. 3080–3086, Sep. 2012, ISSN: 00220949. DOI: 10.1242/jeb.070912.

[49] X. Li et al., “Recent developments in gecko-inspired dry adhesive surfaces from fabrication to application,” *Surface Topography: Metrology and Properties*, vol. 7, no. 2, May 2019, ISSN: 2051672X. DOI: 10.1088/2051-672X/ab1447.

[50] DNV AS, “DNV-ST-N001 Marine operations and marine warranty,” Tech. Rep., 2023.

[51] R. S. Wadhwa, T. Lien, G. Monkman, and H. Regensburg, “Study on the Holding Characterestics of a Magnetic Gripper,” Tech. Rep.

[52] E. Popova and V. L. Popov, “The research works of Coulomb and Amontons and generalized laws of friction,” *Friction*, vol. 3, no. 2, pp. 183–190, Jun. 2015, ISSN: 22237704. DOI: 10.1007/s40544-015-0074-6.

[53] T. Yamamoto, “Mechanism of Friction and Real Contact Area 1. ”Friction” and its Position in ”Tribology”,” Tech. Rep., 2007.

[54] R. I. Taylor, *Rough Surface Contact Modelling—A Review*, May 2022. DOI: 10.3390/lubricants10050098.

[55] R. Sakaguchi, J. Ferracane, and J. Powers, “Fundamentals of Materials Science chapter 4,” *Craig’s Restorative Dental Materials (Fourteenth Edition)*, pp. 29–68, 2019.

[56] T. Nishi, “Friction of diene rubbers on rough floors considering viscoelastic properties in the high strain range,” *Tribology International*, vol. 180, Feb. 2023, ISSN: 0301679X. DOI: 10.1016/j.triboint.2023.108225.

[57] N. Myshkin and A. Kovalev, “Chapter 1 Adhesion and Friction of Polymers and Polymer Composites,” Tech. Rep., 2018. [Online]. Available: www.worldscientific.com.

[58] A. Arvanitakit, B. J. Briscoet, M. J. Adamstt, and S. A. Johnsontt, “THE FRICTION AND LUBRICATION OF ELASTOMERS,” *Tribology series*, vol. 30, pp. 503–511, 1995.

[59] B. J. Briscoe and D. Tabor, “FRICTION AND WEAR OF POLYMERS: THE ROLE OF MECHANICAL PROPERTIES.,” *Br Polym J*, vol. 10, no. 1, pp. 74–78, 1978, ISSN: 0007-1641. DOI: 10.1002/pi.4980100114.

[60] E. Rabinowicz, “The nature of the static and kinetic coefficients of friction,” *Journal of Applied Physics*, vol. 22, no. 11, pp. 1373–1379, 1951, ISSN: 00218979. DOI: 10.1063/1.1699869.

[61] D. H. Cho, B. Bhushan, and J. Dyess, “Mechanisms of static and kinetic friction of polypropylene, polyethylene terephthalate, and high-density polyethylene pairs during sliding,” *Tribology International*, vol. 94, pp. 165–175, Feb. 2016, ISSN: 0301-679X. DOI: 10.1016/J.TRIBOINT.2015.08.027. [Online]. Available: https://www-sciencedirect-com.tudelft.idm.oclc.org/science/article/pii/S0301679X15003692.

[62] B. N. Persson, O. Albohr, F. Mancosu, V. Peveri, V. N. Samoilov, and I. M. Sivebaek, “On the nature of the static friction, kinetic friction and creep,” *Wear*, vol. 254, no. 9, pp. 835–851, 2003, ISSN: 00431648. DOI: 10.1016/S0043-1648(03)00234-5.

[63] B. S. Kuwik, G. Kim, C. Zhai, M. Daud, and R. C. Hurley, “Roughness and humidity effects on contact, friction, and contact plasticity revealed by micromechanical testing and analysis,” *Tribology International*, vol. 178, Feb. 2023, ISSN: 0301679X. DOI: 10.1016/j.triboint.2022.108075.

[64] C. Yang, X. Liu, Z. Huang, T. Wang, and M. Chen, “Detailed Analysis of Friction in Water-Lubricated Bearings under Boundary Lubrication: Model Development and Experimental Validation,” *Journal of Tribology*, vol. 147, no. 10, Oct. 2025, ISSN: 15288897. DOI: 10.1115/1.4067538.

[65] F. P. Bowden and D. Tabor, “Friction, lubrication and wear: a survey of work during the last decade,” Tech. Rep., 1966.

[66] D. CAPANIDIS and J. SOKOLSKA, “The effect of pressure and time of stationary contact under load on the static friction coefficient of polyurethane elastomers (EPUR) during friction on steel in various lubricating conditions,” *Tribologia*, vol. 289, no. 1, pp. 21–29, Mar. 2020, ISSN: 0208-7774. DOI: 10.5604/01.3001.0014.0835.

[67] R. C. Bowers, “Coefficient of friction of high polymers as a function of pressure,” *Journal of Applied Physics*, vol. 42, no. 12, pp. 4961–4970, 1971, ISSN: 00218979. DOI: 10.1063/1.1659881.

[68] F. G. Aquino, T. Sheldrake, J. Clevelario, F. S. Pires, and M. L. Souza, “CREEP BEHAVIOUR OF POLYURETHANES APPLIED IN THE OFFSHORE INDUSTRY UNDER DYNAMIC SERVICE CONDITIONS,” Tech. Rep., Oct. 2011.

[69] T. He, W. Chen, Z. Liu, Z. Gong, S. Du, and Y. Zhang, “The Impact of Surface Roughness on the Friction and Wear Performance of GCr15 Bearing Steel,” *Lubricants*, vol. 13, no. 4, Apr. 2025, ISSN: 20754442. DOI: 10.3390/lubricants13040187.

[70] E. Jansons and K. A. Gross, “The impact of ice texture on coefficient of friction for stainless steel with different surface roughness,” in *Key Engineering Materials*, vol. 800 KEM, Trans Tech Publications Ltd, 2019, pp. 308–312, ISBN: 9783035714074. DOI: 10.4028/www.scientific.net/KEM.800.308.

[71] TWD, “Basis of Design JdN MP follower and SF Inch Cape,” Tech. Rep., 2025.

[72] T. Sarpkaya and M. Storm, “In-line force on a cylinder translating in oscillatory flow,” *Applied Ocean Research*, vol. 7, no. 4, pp. 188–196, Aug. 1985.

[73] DNV, “DNV-RP-C205,” Tech. Rep., 2025.

[74] R. Dean and R. Dalrymple, “WATER WAVE MECHANICS FOR ENGINEERS AND SCIENTISTS,” Tech. Rep., 1991.

[75] DNV, “DNV-RP-N103 Modelling and analysis of marine operations,” Tech. Rep., 2017.

[76] J. R. Morison, M. P. O’brien, J. W. Johnson, and S. A. Schaaf, “The force exerted by surface waves on piles,” *Journal of Petroleum Technology*, pp. 149–154, 1950. [Online]. Available: http://onepetro.org/JPT/article-pdf/2/05/149/2238818/spe-950149-g.pdf/1.

[77] J. D. Wheeler, “Method for Calculating Forces Produced by Irregular Waves,” Tech. Rep., 1970. [Online]. Available: http://onepetro.org/JPT/article-pdf/22/03/359/2228185/spe-2712-pa.pdf/1.

[78] Frank M. White, “Fluid mechanics,” Tech. Rep., 2011.

[79] H. Y. Cho, H. M. Kweon, W. M. Jeong, and S. I. Kim, “A study on the optimal equation of the continuous wave spectrum,” *International Journal of Naval Architecture and Ocean Engineering*, vol. 7, no. 6, pp. 1056–1063, Nov. 2015, ISSN: 2092-6782. DOI: 10.1515/IJNAOE-2015-0074. [Online]. Available: https://www-sciencedirect-com.tudelft.idm.oclc.org/science/article/pii/S2092678216300164.

[80] R. J. Roark, W. C. Young, and R. G. Budynas, *Roark’s formulas for stress and strain*. McGraw-Hill, 2002, p. 852, ISBN: 007072542X.

[81] C. Mittelstedt, “Theory of Plates and Shells,” Tech. Rep., 2023.

[82] S. Timoshenko and S. Woinowsky-Krieger, “Theory_of_plates_and_shells,” Jul. 1989.

[83] DNV AS, “DNV-RP-C202 Buckling Strength of Shells,” Tech. Rep., 2019.

[84] A. Ibrahim, Y. Ryu, and M. Saidpour, “Stress Analysis of Thin-Walled Pressure Vessels,” *Modern Mechanical Engineering*, vol. 05, no. 01, pp. 1–9, 2015, ISSN: 2164-0165. DOI: 10.4236/mme.2015.51001.

[85] *Pile Plugs Monopiles – TMS*. [Online]. Available: https://tms.nl/offshore-equipment-tms/pile-plugs-monopiles/.

[86] *HYDROHAMMER® - IQIP’s Hydraulic Impact Hammer*. [Online]. Available: https://iqip.com/products/pile-driving-equipment/hydrohammer/.

[87] J. Tjaberings, S. Fazi, and E. Ursavas, “Evaluating operational strategies for the installation of offshore wind turbine substructures,” *Renewable and Sustainable Energy Reviews*, vol. 170, p. 112 951, Dec. 2022, ISSN: 1364-0321. DOI: 10.1016/J.RSER.2022.112951. [Online]. Available: https://www-sciencedirect-com.tudelft.idm.oclc.org/science/article/pii/S1364032122008322.

[88] *Bokalift 2 - Heavy Lift Vessel | TGS 4C | 4C Offshore*. [Online]. Available: https://www.tgs4c.com/vessels/vessel-bokalift-2-vid3672.html.

[89] *Investing in the future: Major crane upgrade for offshore installation vessel Aeolus | Van Oord*. [Online]. Available: https://www.vanoord.com/en/updates/investing-future-major-crane-upgrade-offshore-installation-vessel-aeolus/.

A. Craneless Buoyancy-Assisted Monopile Upending

M.T. van der Slot; J. Jovanova; J. Termorshuizen, TU Delft, the Netherlands

Abstract The increasing size of offshore wind monopiles presents significant challenges for conventional crane-based installation methods, which rely on scarce and costly Heavy Lift Vessels (HLVs). This study proposes a craneless installation method based on buoyancy-assisted upending using a friction-based gripper system.

The monopile is transported in a buoyant horizontal configuration and engaged by a gripper mounted on a Jack-Up Vessel. Controlled internal ballasting of the monopile and vertical actuation induce rotation about a passive pivot, while a distributed friction interface transfers the required loads. A combination of global dynamic analysis and local interface design is used to quantify the governing loads and define the system requirements.

The results show that buoyancy assistance significantly reduces the effective load on the gripper, enabling load transfer through a distributed clamping system. A functional mechanical concept, the Radial Hydraulic Gripper, is developed to demonstrate how the required forces and motions can be realized, including dynamic dampers and fail-safe mechanisms.

The study demonstrates that a physically feasible alternative to conventional crane-based installation can be achieved. By eliminating the need for HLVs, the proposed concept enables the use of Jack-Up Vessels and offers strong potential for improving operational flexibility and reducing installation costs in offshore wind projects.

A.1. INTRODUCTION

The rapid scaling of offshore wind turbines has led to a continuous increase in the size and mass of monopile foundations, creating significant logistical challenges for the industry. Today, next-generation XXL monopiles regularly exceed 2,000 tonnes, with dimensions projected to grow even further [6]. This scale has pushed Jack-Up Vessels (JUVs), originally designed for 1,000-tonne monopiles, to their operational limits [3]. Consequently, developers are increasingly forced to rely on floating Heavy Lift Vessels (HLVs) equipped with large crane capacities. While technically effective, this shift introduces high operational costs and creates a dependence on a scarce fleet of highly specialized vessels. As global installation demands increase, the limited availability of high-capacity HLVs is projected to become a critical supply chain bottleneck for future offshore wind development [8].

To mitigate these constraints, this paper proposes a craneless, buoyancy-assisted upending method utilizing a custom friction-based gripper system mounted on a highly available JUV. As illustrated in Figure A.1, the monopile is delivered in a buoyant, horizontal configuration and directly engaged by the side-mounted gripper. Instead of lifting the foundation with a crane, the system relies on controlled internal seawater ballasting to shift the centre of gravity. Coupled with vertical jacking actuation, this induces a controlled rotation about a passive pivot point, while the distributed friction interface safely transfers the massive structural loads.

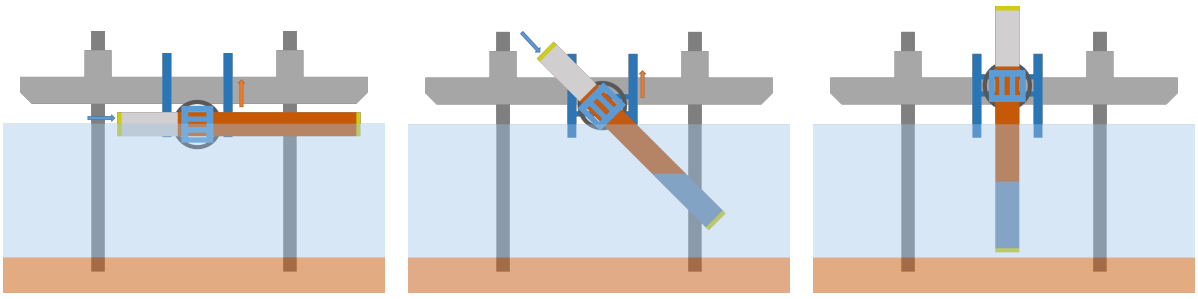

(a) Gripper engagement and initiation of internal ballasting.

(b) Rotation induced by internal ballasting and vertical actuation.

(c) Final vertical configuration followed by controlled lowering to the seabed.

Figure A.1: Schematic representation of the buoyancy-assisted upending principle. Internal ballasting and vertical actuation induce rotation of the monopile about a passive pivot.

The main objective of this study is to evaluate the kinematic, structural, and mechanical feasibility of this concept. The paper sequentially defines the global dynamic boundary conditions, evaluates the local friction-based load transfer interface, and presents a fully functional mechanical concept design. Ultimately, this study aims to

demonstrate that craneless upending provides a highly viable, cost-effective alternative that safely decouples XXL monopile installation from the constrained HLV supply chain.

A.2. DESIGN FRAMEWORK

The design of the proposed system follows a coupled global–local framework, as illustrated in Figure A.2. The upending process is divided into a global kinematic upending problem and a local structural design problem, which are linked through the resulting load envelope.

The global upending behaviour is governed by three key parameters: the pivot offset (z_{off}), defining the longitudinal engagement location along the monopile; the pivot height ($Z_{G,P}$); and the ballast fill level (z_{fill}). These global parameters determine the upending kinematics and the gripper load envelope.

The load envelope specifies the forces that must be transferred at the gripper–monopile interface. This load transfer is achieved through friction, requiring a distributed normal force applied via polymer contact pads. The local design is therefore defined by the local gripper interface parameters, namely the pad dimensions (L_{pad} and W_{pad}) and the number of pads per ring (n). A two-ring configuration is adopted to ensure stability and adequate load distribution

These global and local parameters define the constraints within which the functional concept design is developed.

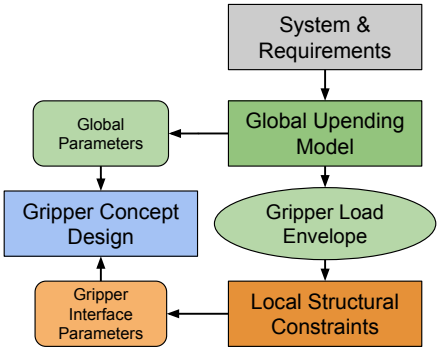

Figure A.2: Design framework linking global upending behaviour to local gripper design.

A.3. GLOBAL UPENDING MECHANICS

A representative XXL monopile is considered to evaluate the proposed concept. The monopile has a mass of 2,170 tonnes, a length of 90 m, an assumed uniform thickness of 0.11 m, a bottom diameter of 9 m, and a top diameter of 8 m, reflecting a tapered geometry. The analysis is performed in a water depth of 50 m under regular wave conditions.

The upending mechanism is governed by the balance of gravitational, buoyancy, and ballast-induced forces, as illustrated in Figure A.3. The combined weight of the monopile (W_{mp}) and ballast (W_{bal}) drives the rotation, while the buoyancy force (F_B) provides an opposing moment. The passive pivot (P) transmits reaction forces to the gripper, consisting of a normal force (R_x) and a shear force (R_z), with the latter directly governing the frictional load requirement. No resisting moment is generated at the pivot, as it is modeled as a free rotation point.

The global upending behaviour is controlled by three key parameters, shown in Figure A.4: the pivot offset (z_{off}), the pivot height ($Z_{G,P}$), and the ballast fill level (z_{fill}). These parameters determine the rotational kinematics and resulting force distribution. The vertical jacking motion increases the pivot height during the operation, assisting rotation and ensuring seabed clearance, while the ballast fill shifts the centre of gravity and drives the system through the rotation.

A parametric quasi-static upending study identifies an optimal configuration that minimizes the peak shear force at the gripper interface while maintaining sufficient seabed clearance. The selected configuration consists of a pivot offset located around 1 m from the conical section of the monopile, a final pivot height of 10 m, and a final ballast volume of 1,803 m^3, resulting in a minimum seabed clearance of 3 m.

To evaluate the behaviour of the system under realistic operating conditions, environmental loading and dynamic effects are incorporated into the analysis. It should be noted that the hydrodynamic model is simplified, and the observed response represents a first-order approximation of the system behaviour. The resulting time-domain response is shown in Figure A.5. The monopile rotates from 0° to approximately 90°. Due to environmental forces,

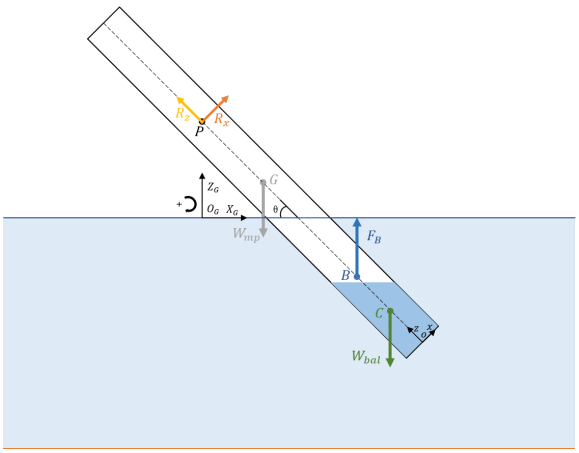

Figure A.3: Free body diagram illustrating the forces governing the passive rotation.

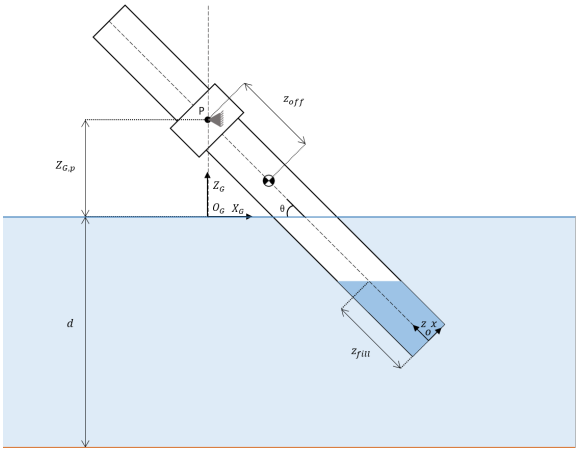

Figure A.4: Representation of the system variables: z_{off}, z_{fill}, and $Z_{G,P}$, defining the upending configuration.

a slight overshoot to approximately 95° is observed, indicating the need for a mechanical locking mechanism in the final design.

The presence of a passive rotational pivot causes the system to oscillate during the upending process. A temporary amplification of the oscillations occurs when the natural period of the system aligns with the wave period. As the mass distribution and submersion of the monopile evolve during the upending process, the natural period of the system changes continuously, causing it to pass through resonance with a range of wave conditions. This indicates that oscillatory behaviour is expected under realistic sea states. To mitigate this behaviour, the final design incorporates a rotational damping mechanism at the passive pivot, dissipating energy and reducing motion amplification during operation.

This leads to undesired local peaks in the normal reaction force, as shown in Figure A.6. However, the shear force governing the frictional load transfer is mainly determined near the vertical configuration and is therefore only marginally influenced by these oscillations.

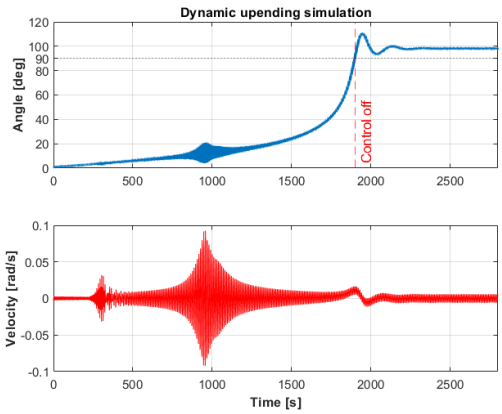

Figure A.5: Time-domain kinematic response of the fully loaded simulation (Waves and Current). Note the dynamic amplification near $t \approx 1000$ s and the final current-induced equilibrium at $95°$.

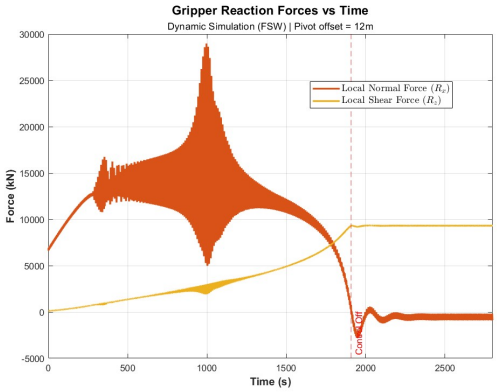

Figure A.6: Gripper reaction forces over time for the full simulation (Waves and Current). A load peak occurs during the resonance crossing at $t \approx 1000$ s.

The resulting peak shear force is approximately 9,500 kN. This corresponds to an effective reduction of the monopile load from its dry weight of 2,170 tonnes to approximately 950 tonnes due to buoyancy assistance. This load defines the primary design requirement for the gripper interface and forms the basis for the friction pad configuration presented in the following section.

A.4. LOAD TRANSFER AND LOCAL DESIGN

The global analysis results in a peak shear force of 9,500 kN at the gripper interface. This load is transferred through friction between the gripper and the monopile. To achieve this, a normal clamping force is applied using discrete friction pads.

Based on experimentally obtained friction coefficients for the steel–polymer interface, and applying a safety factor of 1.5, a total clamping force of approximately 40,000 kN is required to safely resist the imposed shear load.

To apply this clamping force without damaging the monopile shell, the load must be distributed over a sufficiently large contact area. This is achieved using a pad-based interface, where the pad dimensions and distribution govern the local contact pressures. The pad geometry is defined by the pad length L_{pad} and width W_{pad}, as shown in Figure A.7, while the circumferential load distribution is determined by the number of pads per ring, illustrated in Figure A.8.

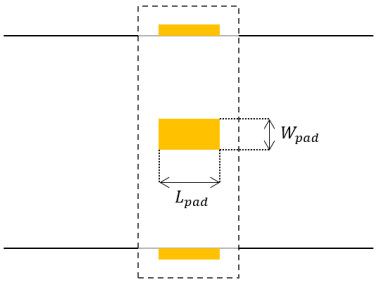

Figure A.7: Schematic defining the gripper pad dimensions, including the pad length (L_p) and pad width (W_p).

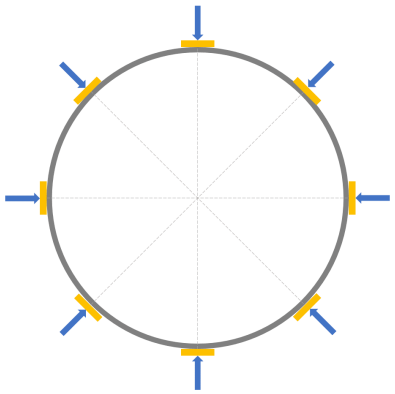

Figure A.8: Eight-pad configuration.

Increasing the total contact area reduces the local pressures, thereby lowering the risk of yielding and local shell buckling. A configuration consisting of pads dimensions of 2.0 m x 1.0 m (L_{pad} by W_{pad}), arranged in an 8-pad configuration per ring, is found to provide sufficient load distribution. A two-ring arrangement is adopted to ensure a stable design and both circumferential and axial load spreading.

Analytical checks confirm that the resulting contact pressures remain within allowable yield limits for both the monopile steel and the polymer interface material, and that local shell instability is avoided. This defines a structurally feasible interface capable of transferring the required load.

The resulting gripper interface parameters form the basis for the mechanical gripper concept design presented in the following section.

A.5. MECHANICAL CONCEPT DESIGN

The global and local analyses define the key requirements for the gripper system. The monopile must be engaged near the conical section, elevated to approximately 10 m, and rotated through controlled internal ballasting. The resulting load envelope includes a peak shear force of 9,500 kN, which must be transferred through friction, requiring a total clamping force of approximately 40,000 kN. The mechanical concept is developed within these constraints.

An overview of the proposed Radial Hydraulic Gripper system is shown in Figure A.9. The system is mounted on a Jack-Up Vessel and engages the monopile using a distributed pad-based interface. The system is connected to the vessel through a vertically guided caterpillar jacking system. A passive rotational pivot links the gripper to this structure, allowing the monopile to rotate under the combined effect of controlled internal ballasting and vertical actuation. The concept integrates radial clamping, vertical translation, and rotational freedom in a single system, enabling controlled and crane-independent upending.

The mechanical concept is illustrated in Figures A.10 and A.11. The process consists of two phases: monopile engagement and subsequent upending.

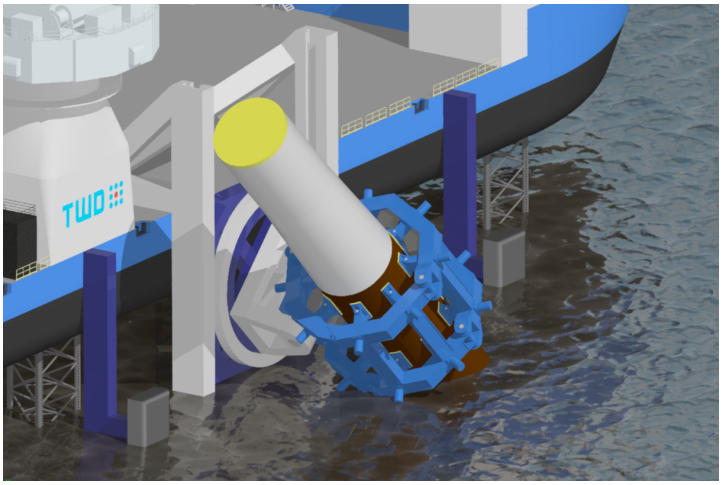

Figure A.9: Overview of the proposed Radial Hydraulic Gripper system mounted on a Jack-Up Vessel.

A.5.1. Engagement Phase

As shown in Figure A.10(a)–(c) the monopile is guided beneath the gripper with the help of two tugboats and brought into contact with the rigid upper gripper frame. The swing-arms are subsequently actuated to enclose the monopile and are mechanically locked, creating a closed structural ring capable of transferring radial loads.

The required clamping force is applied through a set of radially placed hydraulic cylinders, as shown in Figure A.10(d). These cylinders press the friction pads against the monopile surface, generating the normal force required to transfer the imposed shear load. The distributed configuration ensures uniform pressure application and preserves monopile integrity. To ensure fail-safe operation, the hydraulic cylinders are mechanically locked after pressurization, preventing loss of clamping force in the event of hydraulic pressure loss.

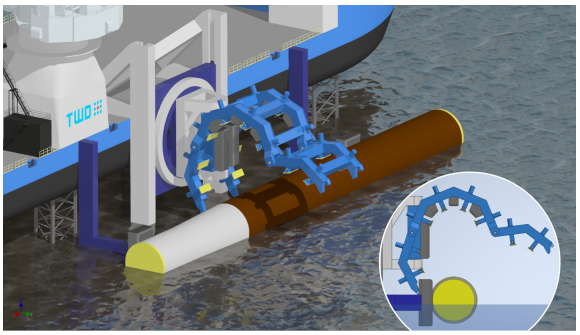

(a) Monopile positioned beneath the open gripper assembly.

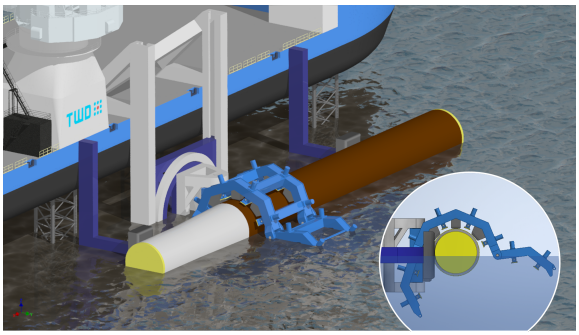

(b) Initial contact between gripper frame and monopile.

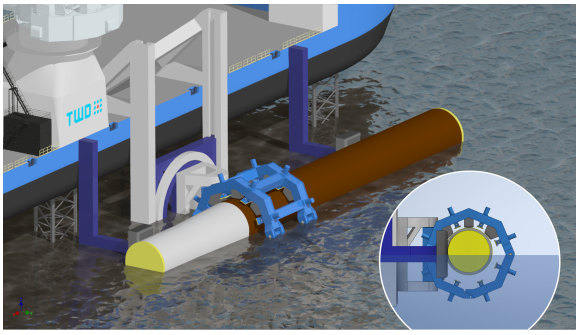

(c) Swing-arms close around monopile and are mechanically locked.

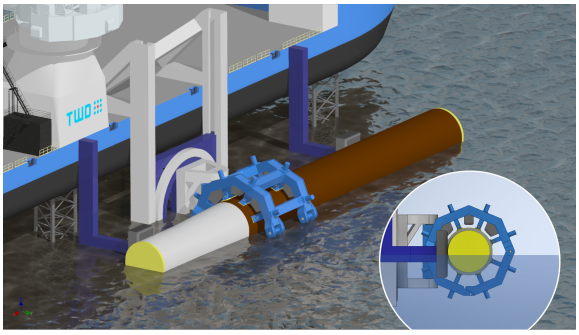

(d) Radial friction pads engage and apply the required clamping force.

Figure A.10: Gripper engagement phase.

A.5.2. Upending Phase

Once the monopile is securely clamped, the engagement phase is concluded and the upending sequence is initiated. The guide bumpers are retracted to provide space for upending. After which, controlled internal ballasting and vertical translation of the gripper frame start to induce rotation about the passive pivot, an intermediate stage of the upending is shown in Figure A.11(a). The vertical motion is achieved using a caterpillar-type hydraulic jacking system along the vessel guide rails. To control the oscillatory behaviour observed in the dynamic response, the passive pivot is equipped with a rotational damping mechanism. Upon reaching the vertical position, a mechanical locking system engages to prevent over-rotation and stabilize the system, as illustrated in Figure A.11(b).

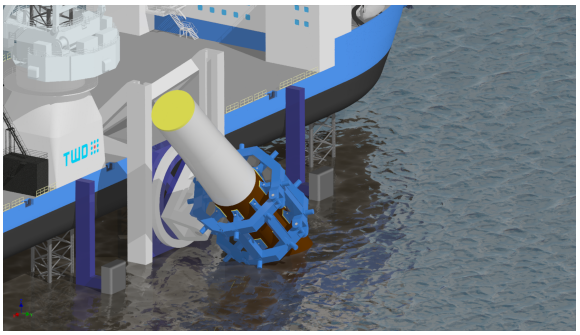

(a) Controlled rotation about the passive pivot during upending.

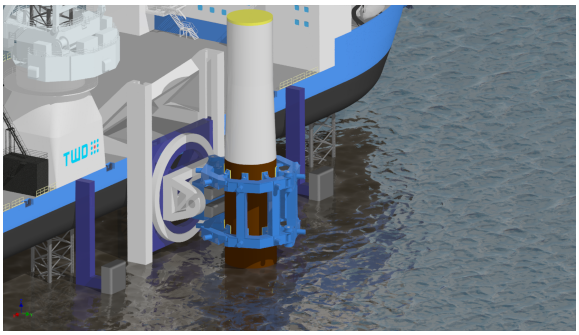

(b) Final vertical configuration with mechanical locking at $90°$.

Figure A.11: Monopile upending phase.

It should be noted that the global behaviour of the system is evaluated in a two-dimensional pitch plane. In practice, environmental loads can also act in the transverse (sway) direction, introducing out-of-plane forces. To accommodate out-of-plane environmental loading, the gripper assembly incorporates a controlled yaw degree of freedom, indicated in Figure A.12. This allows limited transverse rotational motion while integrated damping elements dissipate energy and reduce the transfer of bending moments to the vessel structure.

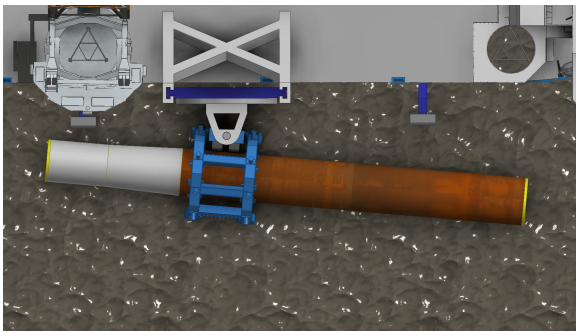

(a) Gripper assembly passively rotating to accommodate for sway (yawing left).

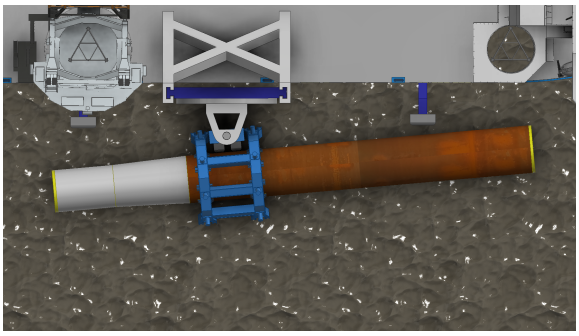

(b) Gripper assembly passively rotating to accommodate for sway (yawing right).

Figure A.12: Top view visualization of the yaw damping mechanism, demonstrating the gripper frame's ability to rotate out-of-plane to prevent extreme bending moments from transferring into the vessel guide rails.

Following the upending operation, the monopile is prepared for final installation. The bottom sealing cap is removed, while the internal pressure at the top of the monopile is controlled to temporarily maintain buoyancy. The vertical jacking system is operated in reverse, lowering the monopile into the seabed until a self-stable embedment depth is reached. At this stage, the gripper can release the monopile, after which conventional piling operations using a hydrohammer complete the installation.

The proposed system demonstrates that the required clamping forces, kinematic motion, and load transfer can be achieved within a single integrated design. Radial hydraulic clamping, vertical actuation, and rotation about a passive pivot enable a physically feasible installation system, while additional yaw and pitch damping allow for realistic offshore loading conditions.

The design therefore establishes a functional mechanical solution for the craneless upending method. Detailed structural sizing and component-level design are outside the scope of this work.

A.6. DISCUSSION

The presented results demonstrate that the proposed buoyancy-assisted upending method can reduce the effective load on the gripper system to manageable levels and enable controlled rotation of XXL monopiles. The integration of a friction-based gripper, combined with vertical actuation and a passive pivot, provides a physically feasible installation concept.

Several limitations should be considered when interpreting these results. The global dynamic behaviour is primarily evaluated in a two-dimensional pitch plane, assuming a rigid vessel and gripper structure. In reality, structural flexibility and out-of-plane motions may influence the load distribution.

In addition, the hydrodynamic environment is simplified by considering regular wave excitation and neglecting wave slamming effects during the transition through the water surface. As a result, peak loads under realistic offshore conditions may be higher, even though the determined load levels provide a representative baseline.

At the local level, the structural integrity of the monopile is assessed using simplified analytical models for yielding and buckling. While these approaches provide conservative design estimates, they do not capture the full three-dimensional stress interactions that arise from the combination of global bending and local radial compression. The effect of dynamic loading on the frictional behaviour, including potential pressure fluctuations and micro-slip, is also not captured in the current model. A key uncertainty therefore remains in the combined effect of these load components under extreme environmental conditions, which may govern the ultimate structural feasibility of the concept.

Further development of the concept requires more detailed numerical and experimental validation. This includes the extension of the dynamic model to fully coupled three-dimensional simulations, incorporating irregular wave spectra and vessel interaction. Detailed structural verification using finite element methods is required to assess local stress concentrations and validate the pad configuration.

Finally, the current design is tailored to a single monopile configuration. For practical offshore application, the concept should be extended to accommodate a range of monopile dimensions through adaptable or modular interface designs.

A.7. CONCLUSION

This study presents a craneless installation method for XXL monopiles based on buoyancy-assisted upending and a friction-based gripper system. The results show that buoyancy assistance effectively reduces the perceived weight of the monopile by more than a factor of two, enabling load transfer through a friction-based interface.

A Radial Hydraulic Gripper concept is developed to realize this principle. The required frictional force is safely applied to the monopile through a distributed pad-based interface, while vertical actuation combined with controlled internal ballasting induces rotation about a passive pivot, enabling upending. Dynamic effects observed in the upending process, including oscillatory behaviour and out-of-plane loading, are addressed through the inclusion of rotational damping and yaw compliance within the design.

The proposed concept demonstrates that a physically feasible alternative to conventional crane-based installation methods can be achieved. By eliminating the need for a scarce Heavy Lift Vessel, the system enables the use of Jack-Up Vessels, increasing operational flexibility and offering strong potential for reducing installation costs in future offshore wind installations.

B

Analytical Derivation of the Strip Theory Models

Because the monopile pitches continuously during the upending sequence, the boundaries of both the external ocean water and the internal liquid ballast form non-linear geometric intersections with the cylindrical shell. To accurately calculate the resulting forces, moments, and shifting inertia, this study employs a 1D numerical strip theory approach.

This appendix details the mathematical framework used to discretize the monopile, calculate the exact submerged geometries, and derive the governing parameters for both the external buoyancy and the internal Free Surface Effect (FSE).

B.1. Numerical Buoyancy via Strip Theory

To accurately capture the non-linear buoyancy moments during the upending sequence, the total length L of the monopile is discretized into N longitudinal elements (strips) of thickness dz, as illustrated in Figure B.1.

B.1.1. Geometric Discretization

For each individual strip i, the global vertical position of its center $Z_{G,i}$ is determined geometrically. This position depends on the global pivot height $Z_{G,P}$, the longitudinal distance from the gripper pivot ($z_p - z_i$), and the current pitch angle θ:

$$Z_{G,i} = Z_{G,P} - (z_p - z_i)\sin(\theta) \tag{B.1}$$

In this formulation, $Z_{G,i}$ represents the global vertical coordinate of the strip center relative to the still water level (SWL), where $Z_{G,i} = 0$ corresponds exactly to the waterline and a negative value indicates a submerged depth. Furthermore, $Z_{G,P}$ denotes the global vertical coordinate of the gripper pivot, z_p is the longitudinal coordinate of the pivot point measured from the pile base, and z_i defines the longitudinal coordinate of the local strip center, which serves as the origin o_i for the local 2D cross-sectional coordinate system. The pitch angle θ defines the rotation, with 0° representing a purely horizontal orientation.

B.1.2. Submerged Vertical Height

As observed in Figure B.1, during the upending process, a portion of the strips is fully submerged, a portion is partially submerged, and the remainder is completely dry. For fully submerged or completely dry strips, the displaced volume calculation is either the full cylindrical slice or zero, respectively. However, for the partially submerged transition zone, geometric evaluation is required. To determine the operational state of any given strip, the following boundary conditions are established:

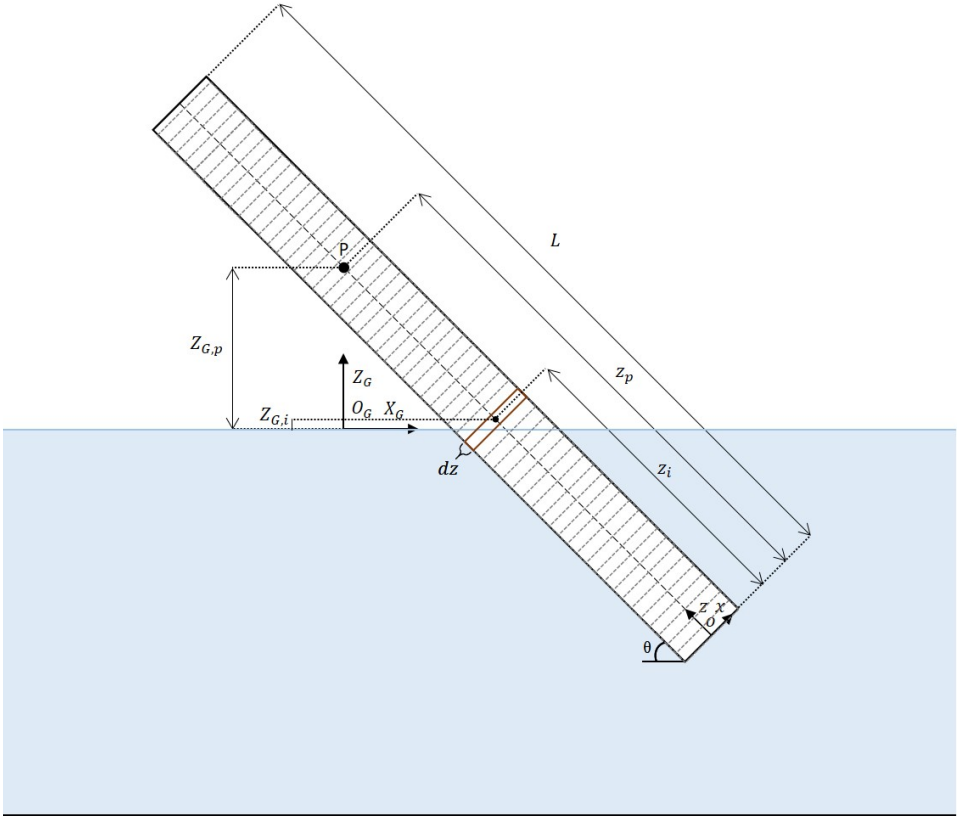

Figure B.1: Illustration of the global strip theory discretization for buoyancy calculation. A subset of strips is shown for clarity, though the entire length of the monopile is discretized in the numerical model.

$$h_i = \begin{cases} 0 & \text{if } Z_{G,i} \geq R|\cos(\theta)| \text{ (Dry)} \\ 2R & \text{if } Z_{G,i} \leq -R|\cos(\theta)| \text{ (Fully Submerged)} \\ R - \frac{Z_{G,i}}{|\cos(\theta)|} & \text{if } -R|\cos(\theta)| < Z_{G,i} < R|\cos(\theta)| \text{ (Partially Submerged)} \end{cases} \tag{B.2}$$

The variable h_i determines the local submerged depth of the circular cross-section at strip i. This depth is measured along the local x-axis and is defined as a function of the monopile radius R and the projected vertical position, as defined visually in Figure B.2(a).

B.1.3. Partially Submerged Cross-Sectional Area

For the strips located in the partially submerged transition zone, the wetted area $A_{sub,i}$ is calculated as the area of a circular segment, evaluated within the local x-y plane as illustrated in Figure B.2(b).

First, the central angle α_i corresponding to the submerged portion of the cross-section is derived using the local submerged height h_i and the monopile radius R:

$$\alpha_i = 2\cos^{-1}\left(\frac{R - h_i}{R}\right) \tag{B.3}$$

Using this central angle, the precise submerged cross-sectional area $A_{sub,i}$ is calculated by taking the area of the circular segment and subtracting the area of the triangular portion from above the waterline:

$$A_{sub,i} = \frac{1}{2}R^2(\alpha_i - \sin(\alpha_i)) \tag{B.4}$$

This formulation ensures the numerical model accurately captures the non-linear change in displaced volume as the circular cross-section cuts through the water surface.

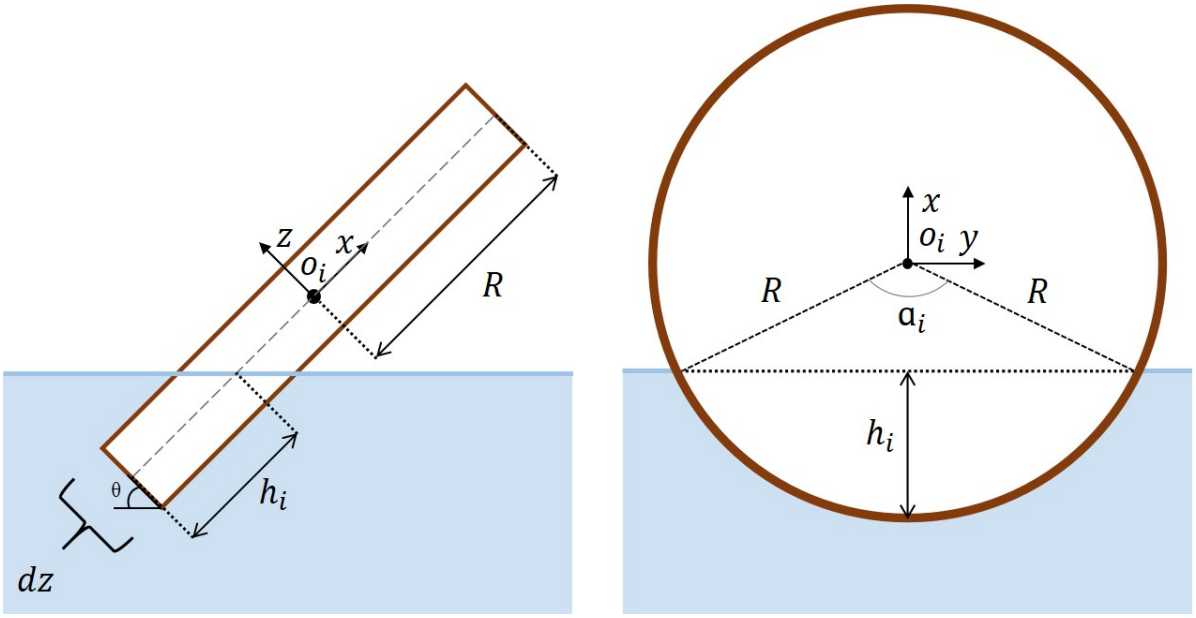

(a) An isolated strip detailing the local buoyancy geometry.

(b) Cross-sectional view (xyo_i) defining the submerged segment.

Figure B.2: Overview of the buoyancy strip geometry, contrasting (a) the longitudinal profile of an isolated strip with (b) the 2D cross-sectional view required for the area calculation.

B.1.4. Total Buoyant Force and Moment

With the submerged area defined, the elemental buoyant force $dF_{B,i}$ acting on a single strip is calculated as:

$$dF_{B,i} = \rho_w \cdot g \cdot A_{sub,i} \cdot dz \tag{B.5}$$

Where ρ_w is the density of seawater and g is the acceleration of gravity. Ultimately, the total buoyancy force F_B acting on the system, and the resulting restoring moment M_B about the gripper pivot, are determined through the discrete summation of all N strips:

$$F_B = \sum_{i=1}^{N} dF_{B,i} \tag{B.6}$$

$$M_B = \sum_{i=1}^{N} (dF_{B,i} \cdot (z_p - z_i) \cos(\theta)) \tag{B.7}$$

B.2. The Internal Free Surface Effect (FSE)

To capture the Free Surface Effect (FSE) of the ballast water, the water must be modeled as a quasi-static liquid where the free surface remains globally horizontal. Because the monopile is tilted at an angle θ, the internal fluid forms a complex wedge shape. This appendix explains how the FSE ballast water within the tilted cylindrical monopile can be modeled.

B.2.1. Strip Theory Discretization and Geometric Mapping

To model the water as a free surface, the monopile is discretized into N strips with thickness dz, as illustrated in Figure B.3

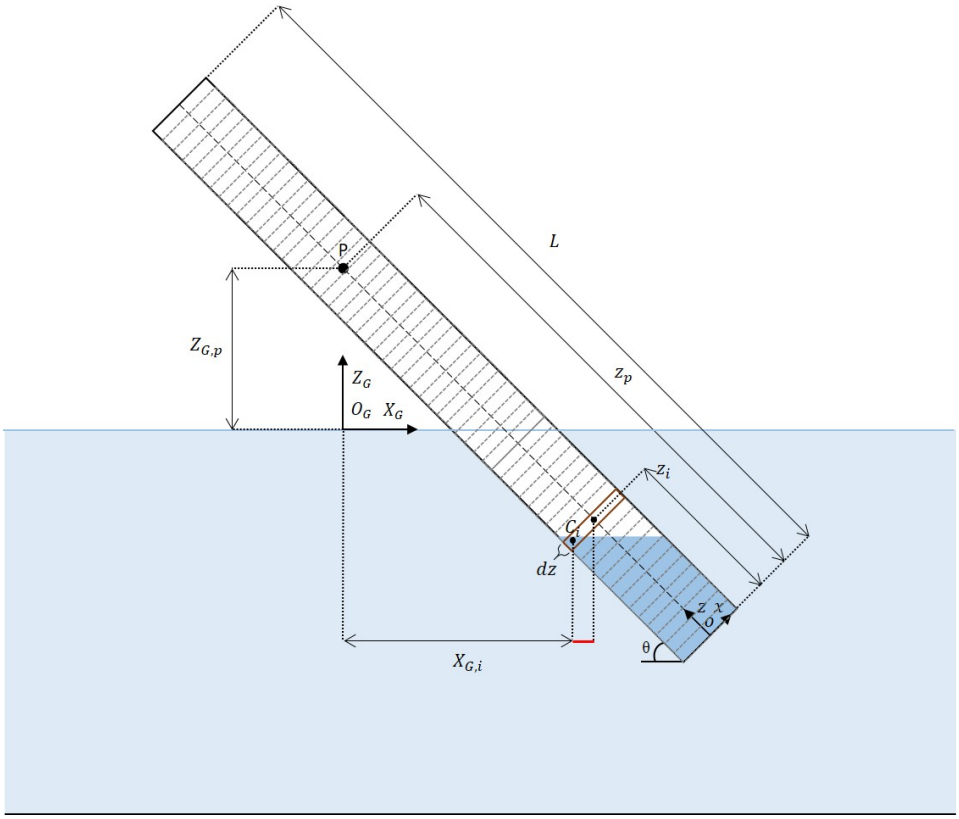

Figure B.3: Global 1D Strip Theory discretization of the internal fluid. The horizontal waterline is projected onto local cross-sectional slices along the monopile length.

For a monopile discretized into N strips of thickness dz, the global vertical coordinate of the center of any internal strip i is defined by the pivot height Z_p and the local longitudinal coordinate z_i:

$$Z_{G,i} = Z_{G,P} - (z_p - z_i)\sin(\theta)$$

To determine the fill level within a tilted strip, the vertical distance between the strip's center ($Z_{G,i}$) and the assumed internal free surface ($Z_{G,bal}$) must be projected onto the local x-axis of the cross-section.

This mapping creates the local water line coordinate, $x_{d,i}$, projected as follows:

$$x_{d,i} = \frac{Z_{G,i} - Z_{G,bal}}{\cos(\theta)}$$

This $x_{d,i}$ represents the distance from the center of the internal circle to the water surface along the local x-axis as defined in Figure B.4a. *(Note: A numerical limit of $|\cos(\theta)| \geq 10^{-6}$ is applied to prevent division by zero singularities as the monopile approaches the vertical orientation at $\theta = 90°$.)*

B.2.2. Local Submerged Height

The local submerged depth $h_{bal,i}$ of the internal cross-section (measured from the lowest point of the inner pipe wall upward) is a function of the internal radius $R_{in} = D/2 - t_{wall}$ and the projected distance $x_{d,i}$. The boundary conditions defining the dry, partially filled, and fully flooded states of the strip are:

$$h_{bal,i} = \begin{cases} 0 & \text{if } x_{d,i} \geq R_{in} \text{ (Dry)} \\ 2R_{in} & \text{if } x_{d,i} \leq -R_{in} \text{ (Fully Flooded)} \\ R_{in} - x_{d,i} & \text{if } -R_{in} < x_{d,i} < R_{in} \text{ (Partially Filled)} \end{cases}$$

Cross-Sectional Fluid Area

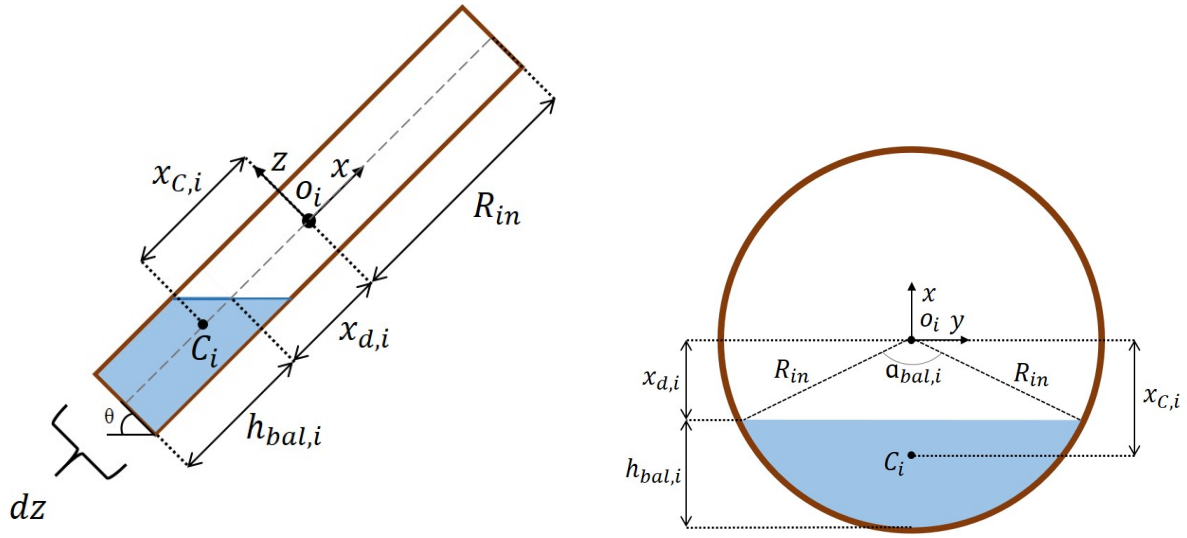

(a) An isolated strip detailing the local fluid geometry.

(b) Cross-sectional view of a partially filled strip.

Figure B.4: Overview of internal fluid geometry definitions, showing (a) the isolated strip perspective and (b) the cross-sectional view for area calculation.

For strips identified as partially filled, the cross-sectional area $A_{bal,i}$ is calculated using the geometry of a circular segment. First, the internal central angle $\alpha_{bal,i}$ is determined:

$$\alpha_{bal,i} = 2\cos^{-1}\left(\frac{R_{in} - h_{bal,i}}{R_{in}}\right)$$

The resulting area of the fluid in the cross-section is:

$$A_{bal,i} = \frac{1}{2}R_{in}^2(\alpha_{bal,i} - \sin(\alpha_{bal,i}))$$

B.2.3. Conservation of Mass and the Volume Solver

Now that the geometry of a single strip is defined, the global vertical elevation of the water surface ($Z_{G,bal}$) that accounts for the total volume currently in the pile must be resolved.

Defining the Target Volume

The physical volume of water injected into the system is dictated by the pump flow rate (Q_{pump}) over time:

$$V_{target} = Q_{pump} \cdot t$$

The Discretized Model Volume

According to the strip theory discretization, the total fluid volume for a guessed $Z_{G,bal}$ is the summation of all individual strip volumes:

$$V_{model}(Z_{G,bal}) = \sum_{i=1}^{N} A_{bal,i}(Z_{G,bal}) \cdot dz$$

The Root-Finding Objective

Because $A_{bal,i}$ is non-linear (due to the circular segment geometry), $Z_{G,bal}$ cannot be isolated algebraically. Instead, an iterative numerical solver (`fzero`) is employed to find the specific $Z_{G,bal}$ where:

$$f(Z_{G,bal}) = V_{model}(Z_{G,bal}) - V_{target} = 0$$

The above formula states that the volume of the pumped water (V_{target}) should be the same as the volume of the model (V_{model}).

B.2.4. Transverse Centroid Shift

In a ”frozen” mass model, the ballast is assumed to be a solid cylinder, meaning its center of mass always sits exactly at the origin o_i. When the mass is allowed to be a free surface, the water naturally pools on the ”downhill” side of the pipe. Consequently, the centroid of the partially filled cross-section shifts away from o_i.

The magnitude of this shift ($x_{C,i}$) is derived from the First Moment of Area for a circular segment as defined in Roark's Formulas for Stress and Strain [80]:

$$x_{C,i} = -S_\theta \frac{2R_{in}^3 \sin^3(\alpha_{bal,i}/2)}{3A_{bal,i}}$$

The value of $x_{C,i}$ dynamically switches sign using S_θ to ensure it always points toward the wall where the water is physically pooling. For $\theta < 90°$, it acts in the opposite direction of the positively defined local x-axis (as seen in Figure B.4a).

B.2.5. Global Gravity Moment Formulation

With the 2D local center of ballast mass position of every fluid slice defined by $(x_{C,i}, z_i)$, these coordinates must be projected into the global frame to determine the true actuating gravity moment (M_{bal}) acting about the gripper pivot P.

First, the physical mass of the water within each strip is calculated:

$$dm_i = \rho_w \cdot A_{bal,i} \cdot dz$$

To calculate the moment created by this mass element, the global horizontal distance between P and the local centroid C_i is required. This global horizontal coordinate (X_{G,C_i}) consists of two perpendicular projections:

- **The Axial Contribution:** The distance along the monopile centerline from the pivot to the strip is $(z_p - z_i)$. Its projection onto the global horizontal axis is $(z_p - z_i)\cos(\theta)$.
- **The Transverse Contribution (The Free Surface Effect):** The fluid centroid is shifted laterally off the centerline by $x_{C,i}$. Because the monopile is pitched at angle θ, this local transverse shift has a global horizontal projection equal to $x_{C,i}\sin(\theta)$.

Combining these yields the exact global horizontal coordinate for the fluid centroid of strip i:

$$X_{G,C_i} = (z_p - z_i)\cos(\theta) + x_{C,i}\sin(\theta)$$

(Note on the physics: Because $x_{C,i}$ is a negative value for $\theta < 90°$, adding the $x_{C,i}\sin(\theta)$ term mathematically decreases the total horizontal distance X_{G,C_i}. This models the physical reality that the fluid is "seeking plumb" and pooling closer to the vertical axis passing through P, thereby reducing the ballast's ability to act as an overturning counterweight).

The total gravity moment of the entire free surface ballast volume is the sum of the contributions from all N strips:

$$M_{bal} = \sum_{i=1}^{N} (dm_i \cdot g \cdot X_{G,C_i})$$

By implementing this summation, the dynamic solver continuously updates the exact 3D center of gravity of the liquid cargo at every timestep.

B.2.6. Mass Moment of Inertia

The rotational inertia of the fluid wedge simplifies to the elemental mass multiplied by the square of the longitudinal distance to the pivot:

$$I_{bal,P} = \sum_{i=1}^{N} \left(dm_i \cdot (z_p - z_i)^2 \right)$$

Because dm_i is calculated using the exact free surface area $A_{bal,i}$ (which naturally trails off to 0 as the strips become dry), this formulation cleanly and accurately captures the shifting mass distribution without unnecessary computational overhead.

B.2.7. Rate of Change of Inertia and Mass Injection

To accurately solve the equation of motion ($\sum M = I_P\ddot{\theta}$), the dynamic model must account for the fact that the monopile is a variable-mass system. As the pump injects water into the pitching pile, the system must exert a structural moment (torque) to accelerate this new, non-rotating water up to the angular velocity ($\dot{\theta}$) of the pile. This physical demand for torque is captured by applying the product rule to the system's angular momentum ($H = I_P \cdot \dot{\theta}$):

$$\frac{dH}{dt} = I_P \cdot \ddot{\theta} + \dot{I}_{bal,P} \cdot \dot{\theta}$$

To determine the rate of change of the ballast's mass moment of inertia ($\dot{I}_{bal,P}$), the Reynolds Transport Theorem (RTT) [78] is applied to the fluid control volume. RTT states that the total rate of change of an extensive property (like inertia) consists of two parts: internal geometric redistribution and the flux of that property across the boundary.

Geometric Redistribution (The Internal Volume)

As the monopile pitches, the water already inside the pile sloshes and changes its distributed shape. In the numerical time-domain solver, this time derivative is handled implicitly by recalculating the total $I_{bal,P}$ using the updated local strip areas at every timestep.

Mass Injection (The Boundary Flux)

The second part of the RTT accounts for the new mass crossing the boundary of the fluid volume—specifically, the free surface waterplane where the pump adds water. The rate at which inertia is injected into the system is the mass flow rate ($\dot{m} = \rho_w \cdot Q_{pump}$) multiplied by the square of the distance from the pivot to the geometric centroid of this waterplane surface (r^2_{surf}).

Because the mass is injected across an elliptical free surface rather than at a single mathematical point, this mass flux must be concentrated at the exact geometric centroid. For any partially filled strip, the horizontal water level cuts a chord across the circular cross-section. The local width of this free surface (w_i) is calculated using the Pythagorean theorem:

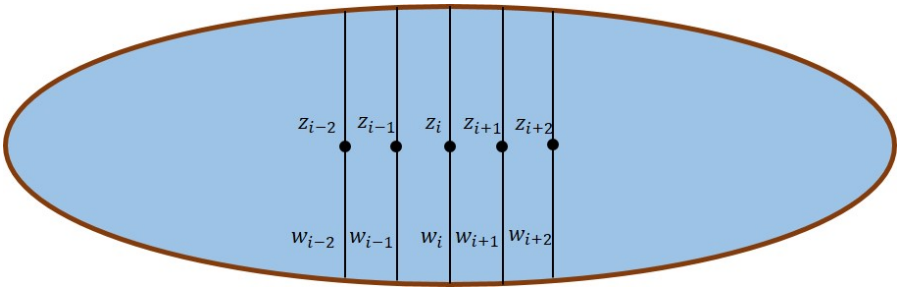

Figure B.5: Top-down projection of the internal fluid waterplane. The 1D strip theory reconstructs the elliptical boundary surface using discrete chord widths (w_i) at local longitudinal coordinates (z_i) to determine the exact geometric centroid for mass injection.

$$w_i = 2\sqrt{2R_{in}h_{bal,i} - h_{bal,i}^2}$$

As illustrated in Figure B.5, the longitudinal position of the boundary surface (z_{surf}) is found by taking the area-weighted average of these local chords along the active length of the fluid wedge:

$$z_{surf} = \frac{\sum_{i=1}^{N}(z_i \cdot w_i)}{\sum_{i=1}^{N} w_i}$$

With the longitudinal center of the mass flux defined, the squared distance from the global pivot (z_p) to this moving boundary is defined as $r_{surf}^2 = (z_p - z_{surf})^2$. Combining these elements yields the exact analytical boundary term for the rate of change of inertia due to mass injection:

$$\dot{I}_{bal,boundary} = (\rho_w \cdot Q_{pump}) \cdot (z_p - z_{surf})^2$$

This scalar value must be explicitly added to the total $\dot{I}_P$ in the equations of motion to ensure the momentum flux of the pumped water is dynamically conserved.

C

Dynamic Time-Domain model Verification

This appendix details the verification of the dynamic time-domain solver before the introduction of complex fluid dynamics (Free Surface Effect) and environmental wave loads. The dynamic outputs are compared directly against the verified quasi-static boundaries established in Section 4.2.

C.0.1. Mathematical Modifications for Baseline Verification

To establish a 1:1 comparison with the static equilibrium model, this verification run temporarily assumes a solid, ”frozen” ballast mass. This requires neglecting the FSE fluid wedge mechanics (Section 4.6).

1. Frozen Ballast Gravity Moment

The fluid center of gravity is assumed to remain perfectly on the longitudinal centerline, negating the transverse FSE shift. The driving moment simplifies to:

$$M_{bal}(t, \theta) = W_{bal}(t) \left(z_p - z_C(t)\right) \cos(\theta) \tag{C.1}$$

where the local centroid $z_C(t)$ remains fixed at the geometric center of the uniform ballast fill level ($z_{fill}/2$).

2. Simplified Rate of Change of Inertia

Because the internal mass is modeled as a flat, uniform cylinder rising at a constant rate, the Reynolds Transport Theorem used for the FSE is replaced by a 1D application of the Leibniz Integral Rule. The rate of change of the internal ballast inertia simplifies to:

$$\dot{I}_{bal,P}(t) = \rho_w A_i (z_{fill}(t) - z_p)^2 \cdot \dot{z}_{fill}(t) \tag{C.2}$$

Where the internal fluid rise velocity ($\dot{z}_{fill}$) is a constant derived directly from the pump rate (Q/A_i).

C.0.2. Baseline Time-Domain Response

To isolate the system’s underlying mass and hydrostatic physics from the environmental dynamics, a baseline dynamic simulation is conducted without external wave excitation ($H_s = 0$ m). However, the relative-velocity hydrodynamic drag term is kept to provide essential system damping.

To align with the static equilibrium model, this verification run temporarily assumes a solid, ”frozen” ballast mass. The dynamic evolution of the system’s geometry can be fully visualized at every integration step. One such state is shown in Figure C.1, illustrating the ”frozen” ballast assumption alongside the active geometric bounds.

The progression of this simulation is actively governed by two continuous control variables: the vertical translation of the gripper pivot and the internal injection of water ballast. As illustrated in Figure C.2,

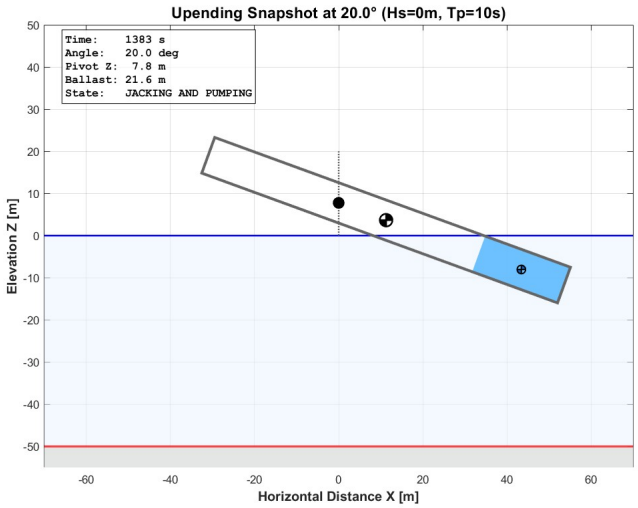

Figure C.1: Snapshot of the baseline dynamic time-domain simulation at $\theta = 20°$. At this stage, the ballast water is modeled as a solid, "frozen" mass.

to avoid artificial buoyancy spikes and numerical ringing, the system initiates from a carefully selected initial pivot height ($Z_{G,P,0} = 2$ m) with an empty internal ballast. Both the jacking mechanism and the ballast pumps operate continuously until the target vertical orientation is achieved just prior to $t = 2000$ s, after which the active controls are halted.

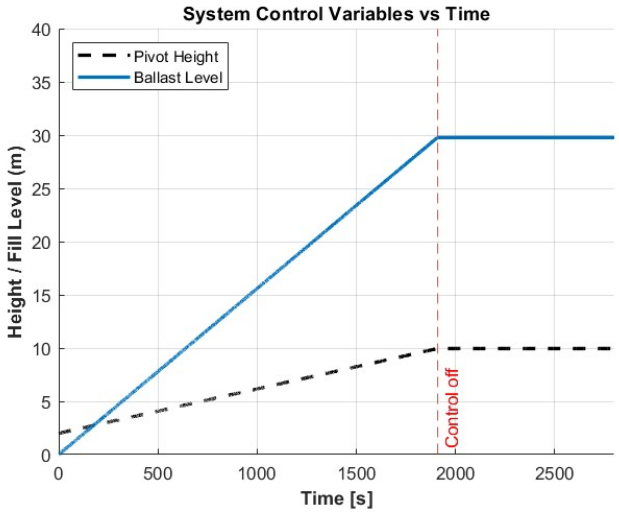

Figure C.2: Progression of the active control variables over time, showing the linear increase of the Global Pivot Height ($Z_{G,P}$) and Ballast Fill Level (z_{fill}) until the controls are deactivated.

The resulting kinematic response of the monopile to these control inputs is presented in Figure C.3. As the ballast water fills and the pivot jacks upwards, the angular velocity remains slow and highly controlled through the first $45°$ of rotation. However, during the final sequence, the monopile swings more rapidly toward the $90°$ target. After the controls are halted, the structure behaves as an underdamped pendulum, showing a decreasing oscillation around the vertical axis until the hydrodynamic drag fully dissipates the remaining kinetic energy.

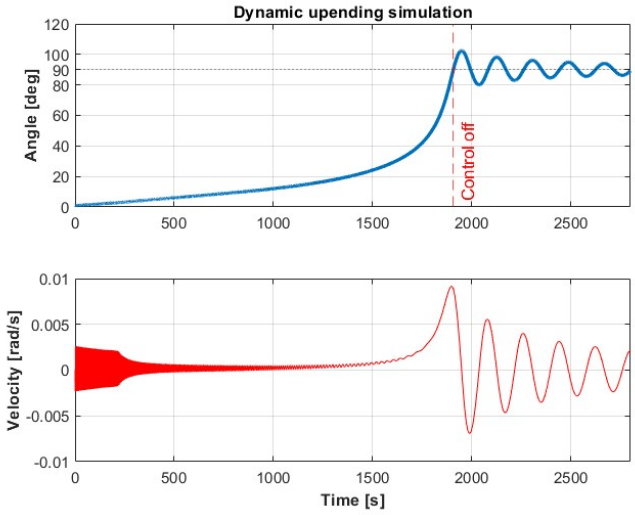

Figure C.3: Time-domain kinematic response of the baseline dynamic simulation, showing the pitch angle (θ) and angular velocity ($\dot{\theta}$) throughout the upending and settling phases.

Because the previously developed quasi-static model evaluates discrete equilibrium states independent of time, a direct time-domain comparison is impossible. Therefore, to correctly compare the two distinct mathematical models, the dynamic time-domain outputs are re-mapped and plotted against the angle (θ).

C.0.3. Moment Balance Verification

Figure C.4 compares the moments between the two models. In the static model, the net moment is exactly zero at all angles. In the dynamic model, thanks to the optimized starting conditions ($Z_{G,P,0} = 2$ m, $\theta_0 = 1°$), initial start-up oscillation is mitigated. After which the dynamic net moment mirrors the quasi-static equilibrium results.

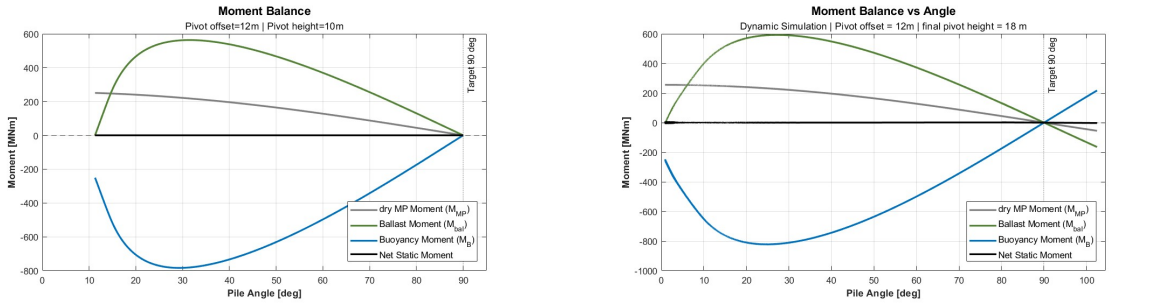

(a) Static evaluation with a constant pivot height of 10 m.

(b) Moments of the dynamic simulation to a final pivot height of 10 m.

Figure C.4: Comparison of the moment balance versus pile angle for a pivot offset of 12 m, showing (a) the static evaluation and (b) the dynamic simulation.

C.0.4. Reaction Force Verification

The validation of the structural load envelope is presented in Figure C.5, comparing the local shear (R_z) and normal (R_x) forces at the gripper.

An important physical distinction between the two models is observed during the early stages of the rotation ($\theta < 40°$). In the quasi-static model, the global pivot height is held constant at the final target elevation ($Z_{G,P} = 10$ m) across all angles. However, as established in the kinematic constraints, the dynamic sequence starts at a much lower pivot height ($Z_{G,P,0} = 2$ m) and gradually jacks upwards. Because the dynamic pivot is initially lower, the monopile is submerged deeper into the water at low angles. This deeper draft generates a larger initial buoyancy force, which counteracts gravity and

results in a noticeably lower peak structural force ($R_x \approx 14,000$ kN) compared to the static assumption ($16,000$ kN).

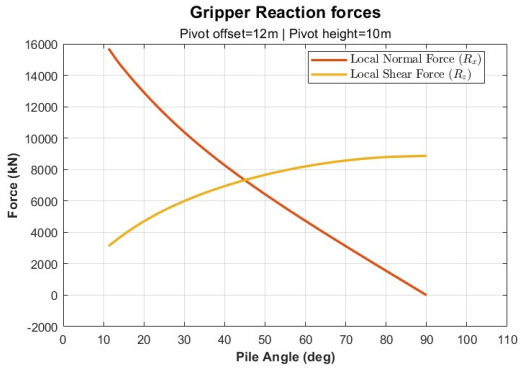

(a) Static evaluation with a constant pivot height of 10 m with the corresponding reaction forces.

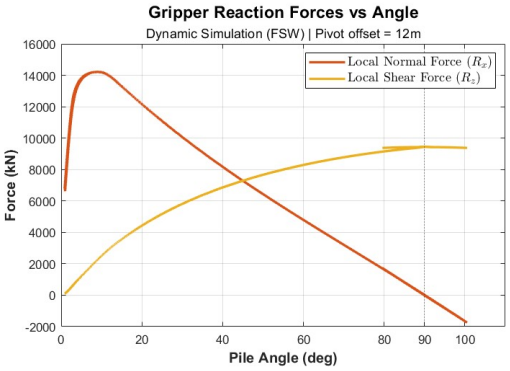

(b) Dynamic simulation reaching a pivot height of 10 m with the corresponding reaction forces.

Figure C.5: Comparison of the gripper reaction forces versus pile angle for a pivot offset of 12 m. While initial normal forces differ due to the transient jacking height, the dynamic shear force converges to the established 9,000 kN static envelope at verticality.

As the dynamic sequence progresses, the jacking height reaches its 10 m target, aligning the dynamic boundary conditions with the static assumptions. Consequently, as the pile approaches verticality, the dynamic force curves exhibit the same trajectory as the static forces.

The dynamic shear force (R_z) peaks at approximately $9,500$ kN as the pile reaches $90°$, which is 500 kN higher than the static simulation ($9,000$ kN). This is because the hydrodynamic resistance, which is added with the dynamic simulation, results in the monopile requiring more ballast to reach $90°$, increasing the total weight of the system. Furthermore, the normal force (R_x) smoothly decays to zero in both models.

This mathematical convergence confirms that the continuously changing inertia components, the shifting integration boundaries ($\dot{z}_{fill}$, $\dot{z}_{swl}$), and the local-to-global coordinate transformations in the time-domain ODE solver are structurally sound. With the baseline physics verified, the dynamic engine is validated for the introduction of external wave excitation and internal water free surface effects (as detailed in Chapter 4).

D

Friction Tests

This appendix is not included in the public version of the report due to confidentiality.

E

Multi-Criteria Analysis Definitions

This appendix provides a detailed breakdown of the sub-criteria and individual weighting factors used in the Multi-Criteria Analysis (MCA) for the concept selection presented in Section 6.3.

1. Operational Efficiency (Total Weight: 30%)

- *Engagement Tolerance (10%):* The maximum allowable spatial misalignment the concept can accommodate during the initial capture of the floating monopile.
- *Attachment Strategy (10%):* The simplicity of the pad configuration to transition from an 'open' state to a 'grip' state.
- *Required Energy (5%):* The relative amount of mechanical or hydraulic work that must be generated to apply the required friction force.
- *Retraction Ease (5%):* The risk of the mechanism jamming or failing to release once the upending is complete.

2. Safety & Integrity (Total Weight: 30%)

- *Fail-safe Reliability (20%):* The system's ability to maintain a secure grip on the monopile in the event of a total power or hydraulic pressure loss.
- *Pressure Control (10%):* The ability of the concept to ensure a symmetrical load distribution across the friction pads, mitigating the risk of local buckling in the thin monopile wall.

3. System Integration (Total Weight: 25%)

- *Mass Efficiency (10%):* The estimated self-weight of the gripper assembly.
- *No-go Zone Buffer (5%):* The spatial clearance margin the concept maintains relative to the conical transition sections of the monopile.
- *Vertical Compactness (5%):* The vertical spatial footprint required to perform the translation.
- *Rotational Inertia (5%):* The impact of the gripper's mass distribution relative to the pivot point, which influences the structural loading withing the gripper.

4. Fabrication (Total Weight: 15%)

- *Total Costs (10%):* A comparative estimation of the total capital expenditure required to build the design.
- *Manufacturing Complexity (5%):* The degree to which the concept relies on standard, commercially available offshore components versus complex, custom-machined components.

F

Global Upending Simulation Codebase

This appendix contains the core computational scripts used to execute the dynamic time-domain simulation of the crane-less upending procedure, as described in Chapter 4. The codebase utilizes MATLAB's `ode45` solver to evaluate the non-linear equation of motion, integrating real-time wave kinematics, fluid mass injections, and the Free Surface Effect (FSE).

F.1. Master Simulation Script

The master script determines the geometric properties, establishes the environmental wave boundaries, and executes the two-phase time-domain integration (active upending followed by turning of the control inputs when a vertical orientation is reached). Plotting and visualization have been left out for concisiveness.

Listing F.1: run_simulation_FSW.m: Main execution script.

```
% run_simulation_FSW.m
% Master script: Two-Phase Simulation (Upending -> Settling) WITH WAVES

%% 1. SYSTEM CONFIGURATION
sys.g = 9.81;               % m/s^2
sys.rho_s = 7850;           % kg/m^3
sys.rho_w = 1025;           % kg/m^3

% Monopile Geometry
sys.L = 90;                 % m
sys.D = 9.0;                % m
sys.t_wall = 0.110;         % m
sys.CoG_dry = sys.L / 2;    % m
sys.R_out = sys.D / 2;                  % m
sys.R_in  = sys.R_out - sys.t_wall;     % m

% Derived Areas
sys.A_outer = pi * (sys.D/2)^2;                 % m^2
sys.A_inner = pi * (sys.D/2 - sys.t_wall)^2;    % m^2
sys.A_steel = sys.A_outer - sys.A_inner;        % m^2
sys.M_mp    = sys.A_steel * sys.L * sys.rho_s;  % kg

% --- PIVOT & GRIPPER ---
sys.z_off = 12;                         % m
sys.z_p   = sys.CoG_dry + sys.z_off;    % m

% --- CONTROL LIMITS ---
sys.Z_p_start = 2;
sys.Z_p_max   = 20;      % Max Jacking Height [m]
sys.Q_pump    = 3400/3600; % [m^3/s]
sys.v_jack    = 0.25/60;    % [m/s]

% Strip Theory
```

```
sys.N_strips = 500;
sys.dz = sys.L / sys.N_strips;
sys.z_strips = linspace(sys.dz/2, sys.L-sys.dz/2, sys.N_strips)';

%% 2. WAVE ENVIRONMENT DEFINITION
sys.d  = 50;          % Water Depth [m]
sys.Hs = 2;           % Significant Wave Height [m]
sys.Tp = 10;          % Peak Period [s]
sys.vc = 0.5;         % Current Velocity [m/s]
sys.wave_dir = 1;     % 1 = Waves move Left to Right (+X)
sys.Cd = 0.68;        % Drag Coeff (DNV-RP-N103)
sys.Ca = 1.0;         % Added Mass Coeff (DNV-RP-N103)

% Wave Solver (Dispersion Relation)
sys.omega_wave = 2 * pi / sys.Tp;
k0 = sys.omega_wave^2 / sys.g; % Deep water guess
options = optimset('Display','off');
sys.k_wave = fsolve(@(k) sys.omega_wave^2 - sys.g * k * tanh(k * sys.d), k0, options);

%% 3. PHASE 1: THE UPENDING (Active Control)
theta_0 = deg2rad(1);
omega_0 = 0;
Y0 = [theta_0; omega_0];

% Stop Event: Tells ode45 to halt exactly at 90 degrees
options_phase1 = odeset('RelTol', 1e-5, 'AbsTol', 1e-6, ...
                        'Events', @(t,y) event_reach_vertical(t,y));

t_span1 = [0 3000];
[T1, Y1, te, ye, ie] = ode45(@(t, y) upending_dynamics_FSW(t, y, sys), ...
                             t_span1, Y0, options_phase1);

if isempty(te)
    warning('System never reached 90 degrees in Phase 1!');
    T = T1; Y = Y1;
    t_stop_sim = T1(end);
else
    %% 4. PHASE 2: THE SETTLING (Frozen Control)
    % Capture the "Frozen" inputs at the moment of stopping
    fixed_Z_pivot = min(sys.Z_p_start + sys.v_jack * te, sys.Z_p_max);
    fixed_Vol_bal = min(sys.Q_pump * te, sys.L * sys.A_inner);

    Y0_phase2 = ye.';
    t_span2 = [te, max(te + 100, 2800)];
    options_phase2 = odeset('RelTol', 1e-5, 'AbsTol', 1e-6);

    [T2, Y2] = ode45(@(t, y) settling_dynamics_w(t, y, sys, fixed_Z_pivot, fixed_Vol_bal),
        ...
                     t_span2, Y0_phase2, options_phase2);

    % Stitch Results
    T = [T1; T2(2:end)];
    Y = [Y1; Y2(2:end,:)];
end

% --- VISUALIZATION AND PLOTTING ROUTINES OMITTED FOR BREVITY ---

%% --- LOCAL FUNCTIONS ---
function [value, isterminal, direction] = event_reach_vertical(t, Y)
    value = deg2rad(90) - Y(1);
    isterminal = 1;
    direction = 0;
end

function dYdt = settling_dynamics_w(t, Y, sys, Z_fixed, Vol_fixed)
    theta = Y(1);
    omega = Y(2);

    sys_static = sys;
    sys_static.Z_p = Z_fixed;
    sys_static.Q_pump = 0;    % Turn off the pump
```

```
104
105     dist_pivot_to_dry_cog = sys_static.z_p - sys_static.CoG_dry;
106     M_g_dry = (sys_static.M_mp * sys_static.g) * (dist_pivot_to_dry_cog * cos(theta));
107
108     [M_g_ballast, I_bal, I_dot_bal_boundary] = get_free_surface_ballast_FSW(theta, Vol_fixed,
            sys_static);
109     [~, M_buoy] = get_buoyancy_forces_FSW(theta, Z_fixed, sys_static);
110     M_net_static = M_g_dry + M_g_ballast + M_buoy;
111
112     [M_drag, M_wave_inertia] = get_wave_loads(t, theta, omega, Z_fixed, sys_static);
113
114     z_swl = sys_static.z_p - (Z_fixed / sin(theta));
115     z_dot_swl = (Z_fixed * cos(theta)/sin(theta)^2) * omega; % Jacking velocity is zero
116
117     [I_steel_added, I_dot_steel_added] = get_inertia_properties_FSW(theta, z_swl, z_dot_swl,
            sys_static);
118
119     I_tot = I_steel_added + I_bal;
120     I_dot_tot = I_dot_steel_added + I_dot_bal_boundary;
121
122     alpha = (M_net_static + M_drag + M_wave_inertia - (I_dot_tot * omega)) / I_tot;
123     dYdt = [omega; alpha];
124 end
```

F.2. Dynamic Equation of Motion

This function constructs the non-linear Equation of Motion (Eq. 4.14) at each time step. It actively couples the moving boundary constraints (jacking and pumping) with the hydrodynamic loads.

Listing F.2: upending_dynamics_FSW.m: Main ODE state derivative solver.

```
1  function dYdt = upending_dynamics_FSW(t, Y, sys)
2      theta = Y(1);
3      omega = Y(2);
4
5      if theta < 1e-6; theta = 1e-6; end
6
7      % Kinematics (Control Inputs - Implements Table 3.2)
8      Z_pivot_current = min(sys.Z_p_start + sys.v_jack * t, sys.Z_p_max);
9      sys.Z_p = Z_pivot_current;
10     Vol_ballast = min(sys.Q_pump * t, sys.L * sys.A_inner);
11
12     % Static Moments
13     dist_pivot_to_dry_cog = sys.z_p - sys.CoG_dry;
14     M_g_dry = (sys.M_mp * sys.g) * (dist_pivot_to_dry_cog * cos(theta));
15
16     [M_g_ballast, I_bal, I_dot_bal_boundary] = get_free_surface_ballast_FSW(theta,
           Vol_ballast, sys);
17     [~, M_buoy] = get_buoyancy_forces_FSW(theta, Z_pivot_current, sys);
18     M_net_static = M_g_dry + M_g_ballast + M_buoy;
19
20     % Hydrodynamic Loads
21     [M_drag, M_wave_inertia] = get_wave_loads(t, theta, omega, Z_pivot_current, sys);
22
23     % System Inertia & Added Mass Boundaries
24     z_swl = sys.z_p - (Z_pivot_current / sin(theta));
25     z_dot_swl = -sys.v_jack/sin(theta) + (Z_pivot_current * cos(theta)/sin(theta)^2) * omega;
26
27     [I_steel_added, I_dot_steel_added] = get_inertia_properties_FSW(theta, z_swl, z_dot_swl,
           sys);
28
29     I_tot = I_steel_added + I_bal;
30     I_dot_tot = I_dot_steel_added + I_dot_bal_boundary;
31
32     % Implements Equation of Motion (Eq. 3.12)
33     alpha = (M_net_static + M_drag + M_wave_inertia - (I_dot_tot * omega)) / I_tot;
34     dYdt = [omega; alpha];
35 end
```

F.3. Free Surface Effect (FSE) Fluid Solver

The FSE solver models the internal ballast as a quasi-static liquid. It utilizes an iterative root-finding algorithm to establish the horizontal pooling plane and calculates the resulting shift in the center of gravity and the boundary mass flux.

Listing F.3: get_free_surface_ballast_FSW.m: Computes internal liquid dynamics.

```
function [M_g_ballast, I_bal, I_dot_bal_boundary] = get_free_surface_ballast_FSW(theta,
    V_target, sys)
    if V_target <= 0.001
        M_g_ballast = 0; I_bal = 0; I_dot_bal_boundary = 0;
        return;
    end

    R_in = sys.R_in;
    dz = sys.dz;
    z_i = sys.z_strips;
    z_p = sys.z_p;

    Z_G_i = sys.Z_p - (z_p - z_i) .* sin(theta);

    % Volume Solver (Root Finding for Z_bal)
    Z_min = min(Z_G_i) - R_in;
    Z_max = max(Z_G_i) + R_in;
    vol_error = @(Z_guess) calculate_volume(Z_guess, Z_G_i, theta, R_in, dz) - V_target;

    options = optimset('Display','off', 'TolX', 1e-4);
    Z_bal = fzero(vol_error, [Z_min, Z_max], options);

    % Internal Fluid Geometry
    x_d_i = (Z_G_i - Z_bal) ./ max(abs(cos(theta)), 1e-6);
    h_bal_i = max(0, min(2*R_in, R_in - x_d_i));

    alpha_bal_i = 2 .* acos(max(-1, min(1, (R_in - h_bal_i) ./ R_in)));
    A_bal_i = 0.5 .* R_in^2 .* (alpha_bal_i - sin(alpha_bal_i));
    w_i = 2 .* sqrt(max(0, 2.*R_in.*h_bal_i - h_bal_i.^2));
    dm_i = sys.rho_w .* A_bal_i .* dz;

    % The Centroid Shift (x_C,i)
    x_C_i = zeros(size(z_i));
    active_mask = (A_bal_i > 0) & (A_bal_i < pi*R_in^2);
    d_c_i = (w_i(active_mask).^3) ./ (12 .* A_bal_i(active_mask));
    x_C_i(active_mask) = -d_c_i;

    % Updated Gravity Moment (Implements Eq. 3.23 / 3.24)
    X_G_Ci = (z_p - z_i) .* cos(theta) + x_C_i .* sin(theta);
    M_g_ballast = sum(dm_i .* sys.g .* X_G_Ci);

    % Mass Moment of Inertia (I_bal)
    I_bal = sum(dm_i .* (z_p - z_i).^2);

    % Rate of Change of Inertia (Implements Eq. 3.17)
    if sys.Q_pump > 0 && sum(w_i) > 0
        z_surf = sum(z_i .* w_i) / sum(w_i);
        m_dot = sys.rho_w * sys.Q_pump;
        I_dot_bal_boundary = m_dot * (z_p - z_surf)^2;
    else
        I_dot_bal_boundary = 0;
    end
end

function V_total = calculate_volume(Z_guess, Z_G_i, theta, R_in, dz)
    x_d_i = (Z_G_i - Z_guess) ./ max(abs(cos(theta)), 1e-6);
    h_bal_i = max(0, min(2*R_in, R_in - x_d_i));
    alpha_bal_i = 2 .* acos(max(-1, min(1, (R_in - h_bal_i) ./ R_in)));
    A_bal_i = 0.5 .* R_in^2 .* (alpha_bal_i - sin(alpha_bal_i));
    V_total = sum(A_bal_i .* dz);
end
```

F.4. Hydrodynamic and Hydrostatic Physics

The following functions evaluate the interaction between the moving monopile and the offshore environment, calculating wave-induced Morison forces, numerical buoyancy limits, and shifting system inertia.

Listing F.4: get_wave_loads.m: Calculates Morison equation hydrodynamics.

```
function [M_drag, M_wave_inertia] = get_wave_loads(t, theta, omega_pile, Z_pivot, sys)
    dist_from_pivot = sys.z_p - sys.z_strips;
    z_global = Z_pivot - dist_from_pivot * sin(theta);
    mask_sub = (z_global <= 0) & (z_global >= -sys.d);

    if ~any(mask_sub)
        M_drag = 0; M_wave_inertia = 0; return;
    end

    z_eval = z_global(mask_sub);
    r_arm  = dist_from_pivot(mask_sub);
    dz     = sys.dz;

    % Wave Kinematics (kx - wt)
    k = sys.k_wave;
    w = sys.omega_wave;
    H = sys.Hs;
    d = sys.d;

    x_eval = r_arm * cos(theta);
    phase = (sys.wave_dir * k * x_eval) - (w * t);

    amp_fac = (pi * H / sys.Tp) / sinh(k*d);
    term_z = k * (z_eval + d);

    % Velocities and Accelerations
    u_oscillatory = sys.wave_dir * amp_fac * cosh(term_z) .* cos(phase);
    u_wave = u_oscillatory + sys.vc;
    w_wave = amp_fac * sinh(term_z) .* sin(phase);

    u_acc = sys.wave_dir * (amp_fac * w * cosh(term_z) .* sin(phase));
    w_acc = amp_fac * w * sinh(term_z) .* (-cos(phase));

    % Project to Normal Direction
    u_n = u_wave * sin(theta) + w_wave * cos(theta);
    udot_n = u_acc * sin(theta) + w_acc * cos(theta);

    % Relative Velocity (Implements Eq. 3.20)
    v_pile = r_arm * omega_pile;
    v_rel = u_n - v_pile;

    % Drag Moment (Implements Eq. 3.21)
    F_drag = 0.5 * sys.rho_w * sys.D * sys.Cd * abs(v_rel) .* v_rel * dz;
    M_drag = sum(F_drag .* r_arm);

    % Inertia Moment (Implements Eq. 3.22)
    Cm = 1 + sys.Ca;
    Area = pi * (sys.D/2)^2;
    F_inertia = sys.rho_w * Area * Cm * udot_n * dz;
    M_wave_inertia = sum(F_inertia .* r_arm);
end
```

Listing F.5: get_buoyancy_forces_FSW.m & get_inertia_properties_FSW.m

```
function [F_buoy, M_buoy] = get_buoyancy_forces_FSW(theta, Z_pivot, sys)
    dist_from_pivot = sys.z_p - sys.z_strips;
    Z_centers = Z_pivot - dist_from_pivot * sin(theta);
    R = sys.D / 2;

    abs_cos_theta = max(abs(cos(theta)), 1e-6);
    local_water_level = Z_centers ./ abs_cos_theta;

    h_vec = R - local_water_level;
```

```
    h_clamp = max(0, min(2*R, h_vec));

    term1 = R^2 * acos((R - h_clamp)/R);
    term2 = (R - h_clamp) .* sqrt(2*R*h_clamp - h_clamp.^2);
    A_sub = real(term1 - term2);

    dF = A_sub * sys.dz * sys.rho_w * sys.g;
    F_buoy = sum(dF);
    arms = dist_from_pivot * cos(theta);
    M_buoy = -sum(dF .* arms);
end

function [I_steel_added, I_dot_steel_added] = get_inertia_properties_FSW(theta, z_swl,
    z_dot_swl, sys)
    r_sq = (sys.z_strips - sys.z_p).^2;

    % 1. Steel Inertia (Implements Eq. 3.14)
    m_line_steel = sys.M_mp / sys.L;
    I_steel_p = sum(m_line_steel .* r_sq .* sys.dz);

    % 2. Added Mass Inertia (Implements Eq. 3.16)
    mask_swl = sys.z_strips <= z_swl;
    m_line_added = sys.Ca * sys.rho_w * sys.A_outer;
    I_added = sum(m_line_added .* r_sq(mask_swl) .* sys.dz);

    % Leibniz / Deforming Boundary Mass Flux
    if z_swl > 0 && z_swl < sys.L
        r_surf = abs(sys.z_p - z_swl);
        I_dot_added = m_line_added * r_surf^2 * z_dot_swl;
    else
        I_dot_added = 0;
    end

    I_steel_added = I_steel_p + I_added;
    I_dot_steel_added = I_dot_added;
end
```